

REPORT NO.
UCB/SEMM-2000/02

**STRUCTURAL ENGINEERING,
MECHANICS AND MATERIALS**

**ON THE FORMULATION OF CLOSEST-POINT
PROJECTION ALGORITHMS IN
ELASTOPLASTICITY.**

PART II: GLOBALLY CONVERGENT SCHEMES.

**With Applications to Deviatoric and Pressure-Dependent
Plastic Models.**

BY

A. PÉREZ-FOGUET

AND

F. ARMERO

JANUARY 2000

**DEPARTMENT OF CIVIL AND ENVIRONMENTAL ENGINEERING
UNIVERSITY OF CALIFORNIA
BERKELEY, CALIFORNIA**

On the Formulation of Closest-Point Projection Algorithms in Elastoplasticity.

Part II: Globally Convergent Schemes.*

With Applications to Deviatoric and Pressure-Dependent Plastic Models

by

A. PÉREZ-FOGUET[†] & F. ARMERO*

Structural Engineering, Mechanics and Materials
Department of Civil and Environmental Engineering
University of California, Berkeley CA 94720, USA

Abstract

This paper presents the formulation of numerical algorithms for the solution of the closest-point projection equations that appear in typical implementations of return mapping algorithms in elastoplasticity. The main motivation behind this work is to avoid the poor global convergence properties of a straight application of a Newton scheme in the solution of these equations, the so-called Newton–CPPM. The mathematical structure behind the closest-point projection equations identified in Part I of this work delineates clearly different strategies for the successful solution of these equations. In particular, primal and dual closest-point projection algorithms are proposed, in non-augmented and augmented Lagrangian versions for the imposition of the consistency condition. The primal algorithms involve a direct solution of the original closest-point projection equations, whereas the dual schemes involve a two level structure by which the original system of equations is staggered, with the imposition of the consistency condition driving alone the iterative process. Newton schemes in combination with appropriate line search strategies are considered, resulting in the desired asymptotically quadratic local rate of convergence and the sought global convergence character of the iterative schemes. These properties, together with the computational performance of the different schemes, are evaluated through representative numerical examples involving different models of finite strain plasticity. In particular, the avoidance of the large regions of no convergence in the trial state observed in the standard Newton–CPPM is clearly illustrated.

KEY WORDS: elastoplasticity; return mapping algorithms; closest-point projection; globally convergent schemes; augmented Lagrangian.

* Submitted to *International Journal for Numerical Methods in Engineering*.

[†] On leave from the Department of Matemàtica Aplicada III, ETSECCPB, UPC, Barcelona, Spain, during the Fall semester 1999.

* Corresponding author (armero@ce.berkeley.edu).

1. Introduction

The developments presented in ARMERO & PÉREZ–FOGUET [2000] (referred simply as Part I hereafter) have identified a rich mathematical structure behind the closest-point projection equations characteristic of the local integration of elastoplastic models, including their viscoplastic extensions, in both the infinitesimal and finite deformation ranges. Box 1.1 summarizes these equations following the same notation employed in this previous part of this work. More specifically, the updated values $(\cdot)_{n+1}$ of the stresses and internal variables at the end of a typical time increment $[t_n, t_{n+1}]$ in the solution of the global mechanical boundary-value problem are obtained from their known counterparts $(\cdot)_n$ for a given strain increment $\Delta\varepsilon = \varepsilon_{n+1} - \varepsilon_n$. Associated to this increment, we have the trial values $(\cdot)_{n+1}^{trial}$ of the different variables obtained under the assumption of incremental elastic response. The case of rate-independent elastoplasticity in a typical plastic corrector step, characterized by the enforcement of the consistency condition $f_{n+1} = 0$ from an initial trial solution with $f_{n+1}^{trial} > 0$, has been considered in Box 1.1. The discrete forms of the flow rule and hardening laws have been written without considering explicitly the usual assumptions of convexity and associativity required for a rigorous characterization of the aforementioned variational structure. It is in this general context where we present the numerical algorithms proposed in this work, even though the statements on the convergence properties of the different schemes apply rigorously to the associated convex case only.

Box 1.1 summarizes also the application of a Newton scheme in the solution of the resulting nonlinear algebraic equations. To this purpose, the equations have been written in residual form and the Jacobian matrix utilized in the iterative process identified. The final scheme, referred to as the Newton–CPPM herein, can be found in SIMO & HUGHES [1998] and has become a very popular strategy in the numerical solution of elastoplastic problems. As noted in Section 1 of Part I of this work, the asymptotic quadratic rate of convergence of this iterative scheme makes this approach very attractive. However, its limited global convergence properties leads often to a lack of convergence for large ranges of the initial trial state. This situation is related to the strong nonlinearity of the equations which may arise, for example, from the high curvature of the yield function, as it can be found in typical practical applications. The numerical results reported in DE SOUZA NETO et al. [1994], BIĆANIĆ & PEARCE [1996], PÉREZ–FOGUET ET AL. [2000a] and herein illustrate these difficulties. These observations identify clearly the goal of this work: the development of efficient globally convergent algorithms for the solution of the closest-point projection equations in elastoplasticity. We focus only on schemes that preserve the local asymptotic rate of convergence characteristic of the original Newton–CPPM. We note also that all the algorithms proposed in this work lead to the exact solution of the original closest-point projection equations. This implies, in particular, that the consistent algorithmic tangent employed in a typical Newton–Raphson solution of the global mechanical boundary-value problem coincides in all cases; see e.g. SIMO & HUGHES [1998].

BOX 1.1. The Newton closest-point projection algorithm for rate-independent elastoplasticity.

- For the plastic corrector step (i.e. $f_{n+1}^{trial} > 0$), define the residuals

$$\mathbf{r}_\varepsilon := \boldsymbol{\varepsilon}_{n+1}^e - \boldsymbol{\varepsilon}_{n+1}^{e,trial} + \Delta\gamma \mathbf{m}_\sigma(\boldsymbol{\sigma}_{n+1}, \mathbf{q}_{n+1}),$$

$$\mathbf{r}_\alpha := -\boldsymbol{\alpha}_{n+1} + \boldsymbol{\alpha}_{n+1}^{trial} + \Delta\gamma \mathbf{m}_q(\boldsymbol{\sigma}_{n+1}, \mathbf{q}_{n+1}),$$

$$r_f := f(\boldsymbol{\sigma}_{n+1}, \mathbf{q}_{n+1}),$$

for the elastic strain $\boldsymbol{\varepsilon}_{n+1}^e$ and strain-like hardening variables $\boldsymbol{\alpha}_{n+1}$, and where

$$\boldsymbol{\sigma}_{n+1} = \partial_{\boldsymbol{\varepsilon}^e} \psi(\boldsymbol{\varepsilon}_{n+1}^e, \boldsymbol{\alpha}_{n+1}) \quad \text{and} \quad \mathbf{q}_{n+1} = -\partial_{\boldsymbol{\alpha}} \psi(\boldsymbol{\varepsilon}_{n+1}^e, \boldsymbol{\alpha}_{n+1})$$

the stresses $\boldsymbol{\sigma}_{n+1}$ and stress-like hardening variables \mathbf{q}_{n+1} , for the stored energy function $\psi(\boldsymbol{\varepsilon}^e, \boldsymbol{\alpha})$ and yield function $f(\boldsymbol{\sigma}, \mathbf{q})$.

- Let

$$\mathbf{r}(\mathbf{x}) := \begin{Bmatrix} \mathbf{r}_\varepsilon \\ \mathbf{r}_\alpha \\ r_f \end{Bmatrix} \quad \text{for} \quad \mathbf{x} := \begin{Bmatrix} \boldsymbol{\varepsilon}_{n+1}^e \\ -\boldsymbol{\alpha}_{n+1} \\ \Delta\gamma \end{Bmatrix}.$$

Consider the Newton iterative scheme

$$\mathbf{x}^{(k+1)} = \mathbf{x}^{(k)} + \mathbf{d}^{(k)} \quad \text{for} \quad \mathbf{d}^{(k)} = -\mathbf{J}^{-1}(\mathbf{x}^{(k)}) \mathbf{r}(\mathbf{x}^{(k)}),$$

with $\mathbf{x}^{(0)} = \{\boldsymbol{\varepsilon}_{n+1}^{e,trial}, -\boldsymbol{\alpha}_{n+1}^{trial}, 0\}^T$ and the Jacobian

$$\mathbf{J} = \nabla \mathbf{r} = \begin{pmatrix} \mathbf{I} + \Delta\gamma \nabla \mathbf{m} \tilde{\mathbf{G}} & \mathbf{m} \\ \nabla f^T \tilde{\mathbf{G}} & 0 \end{pmatrix},$$

where

$$\nabla f = \begin{Bmatrix} \partial_\sigma f \\ \partial_q f \end{Bmatrix}, \quad \mathbf{m} = \begin{Bmatrix} \mathbf{m}_\sigma \\ \mathbf{m}_q \end{Bmatrix}, \quad \nabla \mathbf{m} = \begin{pmatrix} \partial_\sigma \mathbf{m}_\sigma & \partial_q \mathbf{m}_\sigma \\ \partial_\sigma \mathbf{m}_q & \partial_q \mathbf{m}_q \end{pmatrix},$$

and

$$\tilde{\mathbf{G}} = \begin{pmatrix} \partial_{\boldsymbol{\varepsilon}^e \boldsymbol{\varepsilon}^e}^2 \psi & -\partial_{\boldsymbol{\varepsilon}^e \boldsymbol{\alpha}}^2 \psi \\ -\partial_{\boldsymbol{\alpha} \boldsymbol{\varepsilon}^e}^2 \psi & \partial_{\boldsymbol{\alpha} \boldsymbol{\alpha}}^2 \psi \end{pmatrix}.$$

Remark: The condition $\nabla f \cdot \tilde{\mathbf{G}} \mathbf{m} > 0$ strictly is assumed for the underlying continuum model.

An algorithm is globally convergent if all the sequences that it generates converge to a solution of the problem. We refer to the classical global convergence theorem presented in LUENBERGER [1989] (page 187) for details. In the case of interest herein, this property corresponds to convergence for any initial trial state. As studied in detail in this last reference and other classical references on nonlinear optimization, this desired property can be obtained through the consideration of the appropriate line search scheme under certain technical conditions (usually involving the convexity of the variational problem in optimization and the smoothness of the functions involved). We explore this alternative first, by combining the original Newton scheme with a line search designed specifically for the equations of interest here. In particular, the constrained character of the original closest-point projection equations implied by the non-negative character of the plastic multiplier ($\Delta\gamma \geq 0$ in Box 1.1) is taken into account explicitly in the iterative process. Appendix I presents the details of the line search schemes developed in this work. We refer to the resulting algorithm as the primal closest-point projection method (the primal-CPPM in short), given its clear relation to the primal variational formulation of the closest-point projection equations under the usual assumption of convexity and associativity. This first proposed algorithm consists then simply of the Newton scheme with line search.

The special considerations required by the constrained character of the governing equations, with the consequent need of special variations in the computer code, motivate the development of alternative techniques. The consideration of the new augmented primal formulations identified in Part I appears then as a clear option, as it is developed next in this paper. We refer to the final scheme as the augmented-primal-CPPM. In addition of involving a regularized unconstrained problem, the augmentation adds also a simple mechanism for improving the computational efficiency of the original primal-CPPM. Numerical experiments identify in this way a range of the regularizing penalty parameter leading to this improvement.

It is interesting to observe that the original Newton-CPPM has been often interpreted in the literature as imposing the closest-point projection for each iterate, $(\cdot)^{(k)}$ in the notation of Box 1.1; see SIMO & HUGHES [1998], page 143 (Figure 3-10 in this reference, in particular). However, a look at the residual form of the equations clearly shows that this interpretation is not valid since, simply, the residuals $\mathbf{r}^{(k)}$ corresponding to the flow rule and hardening law do not vanish, in general, during the iteration process, except at the converged value. This observation identifies clearly the role played by the consistency condition and led to the dual variational formulations presented in Part I. In this context, the solution can be obtained simply as the roots of the yield function understood as a scalar function of the plastic multiplier. The evaluation of this “dual consistency function” requires the solution of the discrete forms of the flow rule and hardening law for a fixed plastic multiplier and, hence, unconstrained in nature. These considerations lead naturally to a two-level algorithm that we refer as the dual-CPPM. The consideration of a Newton scheme in combination with a line search in both levels assures the asymptotic quadratic

local rate of convergence of the algorithm and its globally convergent character, this latter property holding again under the usual technical conditions (i.e. the associated convex case with smooth material relations). The augmented extension of these ideas, referred to as the augmented–dual–CPPM herein, proves also to be a useful tool to add computational efficiency to the final numerical scheme.

An outline of the rest of the paper is as follows. Sections 2 and 3 describe the details behind the primal and dual algorithms, respectively, in their non-augmented and augmented forms. Appendix I includes again the details of the line search schemes developed in this work for constrained and unconstrained problems. We focus the developments on the rate-independent problem, with extensions to the simpler viscoplastic problem considered briefly in remarks in the end of each section. The properties and performance of the primal and dual classes of algorithms are evaluated numerically in Sections 4 and 5, respectively. Several representative examples are considered involving purely deviatoric and pressure dependent plastic models (both in an associated framework, with the second one involving non-smooth flow vectors), strain hardening and softening, as well as constant and non-constant elasticities. Finite deformation multiplicative plasticity models are considered in all cases. Appendix II includes a summary of the material models considered. The solution of a finite element problem using the primal–CPPM is shown in Section 6, as an example of practical application. Finally, Section 7 presents several concluding remarks, comparing in particular the different proposed algorithms.

2. Primal Algorithms

We develop in this section numerical algorithms based on the primal variational formulations developed in Sections 3 and 4 of Part I of this work for the rate-independent and viscoplastic problems, respectively. More precisely, we address the solution of the corresponding Euler-Lagrange equations or, more generally, their counterparts in the context of non-associated formulations without this variational structure. Extensions involving the corresponding augmented Lagrangian formulations, as developed in Section 5 of Part I, are presented in Section 2.2. We consider the rate-independent elastoplastic problem, with the viscoplastic problem discussed briefly in additional remarks in the end of each section.

2.1. The primal closest-point projection method

A simple and efficient choice when trying to improve the convergence properties of the original Newton closest-point projection method for the rate-independent problem summarized in Box 1.1 is the additional consideration of a line search technique, as described in Appendix I. We consider again the residual form of the equations presented in this box,

namely,

$$\mathbf{r}(\mathbf{x}) := \begin{Bmatrix} \boldsymbol{\varepsilon}_{n+1}^e - \boldsymbol{\varepsilon}_{n+1}^{e,trial} + \Delta\gamma \mathbf{m}_{\sigma_{n+1}} \\ -\boldsymbol{\alpha}_{n+1} + \boldsymbol{\alpha}_{n+1}^{trial} + \Delta\gamma \mathbf{m}_{q_{n+1}} \\ f_{n+1} \end{Bmatrix}, \quad \text{for } \mathbf{x} := \begin{Bmatrix} \boldsymbol{\varepsilon}_{n+1}^e \\ -\boldsymbol{\alpha}_{n+1} \\ \Delta\gamma \end{Bmatrix}, \quad (2.1)$$

the elastic strains, strain-like internal hardening variables, and the discrete plastic multiplier, respectively, all of them at the end t_{n+1} of a typical time step $[t_n, t_{n+1}]$. The flow vectors $\mathbf{m}_{\sigma_{n+1}}$ and $\mathbf{m}_{q_{n+1}}$, and yield function f_{n+1} in (2.1) are given functions of the conjugate stress variables $\boldsymbol{\sigma}_{n+1} = \partial_{\boldsymbol{\varepsilon}^e} \psi_{n+1}$ and $\mathbf{q}_{n+1} = -\partial_{\boldsymbol{\alpha}} \psi_{n+1}$ for the stored energy function $\psi_{n+1} = \psi(\boldsymbol{\varepsilon}_{n+1}^e, \boldsymbol{\alpha}_{n+1})$, as considered in Box 1.1. The interest herein is the consideration of a plastic corrector step, detected by the condition $f_{n+1}^{trial} := f(\boldsymbol{\sigma}_{n+1}^{trial}, \mathbf{q}_{n+1}^{trial}) > 0$ for the trial elastic values $\{\boldsymbol{\varepsilon}_{n+1}^{e,trial}, -\boldsymbol{\alpha}_{n+1}^{trial}, 0\}$, and the corresponding conjugate stress variables $\boldsymbol{\sigma}_{n+1}^{trial}$ and \mathbf{q}_{n+1}^{trial} . The constrained character of the problem arises from the restriction on the last component (say, component n_x) of \mathbf{x} , that is,

$$[\mathbf{x}]_{n_x} := \Delta\gamma \geq 0, \quad (2.2)$$

for the plastic multiplier $\Delta\gamma$. The presence of this constraint requires then the use of the line search scheme described in Section I.2 of Appendix I for unilaterally constrained problems. We denote the final algorithm by the primal closest-point projection method (or, in short, the primal-CPPM). Box 2.1 includes a summary of this scheme for a typical plastic corrector step.

The resulting algorithm is then very similar to the original Newton-CPPM, but with the added considerations associated to the line search and constraint detection. In particular, the condition (I.15) in Appendix I for the activation of the constraint (2.2) reads

$$\mathbf{m}_{\sigma_{n+1}}^{(k)} \cdot (\boldsymbol{\varepsilon}_{n+1}^{e,(k)} - \boldsymbol{\varepsilon}_{n+1}^{e,trial}) - \mathbf{m}_{q_{n+1}}^{(k)} \cdot (\boldsymbol{\alpha}_{n+1}^{(k)} - \boldsymbol{\alpha}_{n+1}^{trial}) > 0, \quad \text{with } \Delta\gamma^{(k)} = 0, \quad (2.3)$$

in a generic iteration (k) . If the condition (2.3) is satisfied, the modified Jacobian (I.17) presented in Box 2.1 is to be used. We observe that both the trial step and the final solution of the plastic corrector step of interest herein (that is, with $\Delta\gamma > 0$ strictly) do not satisfy this condition, and hence the activation of the constraint by the algorithm near then. To gain a better understanding of the relation (2.3), Figure 2.1 depicts a graphical interpretation of this condition for von Mises and Tresca yield conditions with associated perfect plastic flow and constant elasticities. We note, as an aside, that the constraint (2.2) has not become activated in any of the examples presented in Section 4, involving more complex yield conditions. We conclude that, even though the condition (2.3) needs to be considered from a theoretical point of view, it does not lead to added computational cost in practice. We refer to this section for further details and discussion.

As discussed in Appendix I, the global convergence of the algorithm requires the Jacobian to be non-singular and continuously differentiable, with the special considerations

BOX 2.1. Implementation of the primal closest-point projection method (primal-CPPM).

1. Input data: $\{\boldsymbol{\varepsilon}_{n+1}^{e,trial}, \boldsymbol{\alpha}_{n+1}^{trial}\}$, with the corresponding $\{\boldsymbol{\sigma}_{n+1}^{trial}, \mathbf{q}_{n+1}^{trial}\}$ and $f_{n+1}^{trial} > 0$.

2. Initialization: set $k = 0$,

$$\mathbf{x}^{(0)} := \begin{Bmatrix} \boldsymbol{\varepsilon}_{n+1}^{e,trial} \\ -\boldsymbol{\alpha}_{n+1}^{trial} \\ 0 \end{Bmatrix}, \quad \text{and} \quad \mathbf{r}^{(0)} := \begin{Bmatrix} 0 \\ 0 \\ f_{n+1}^{trial} \end{Bmatrix}.$$

3. Compute the Jacobian:

$$\mathbf{J}^{(k)} := \begin{pmatrix} \mathbf{I} + \Delta\gamma^{(k)} \nabla \mathbf{m}^{(k)} \tilde{\mathbf{G}}^{(k)} & \mathbf{m}^{(k)} \\ \nabla f^{(k)T} \tilde{\mathbf{G}}^{(k)} & 0 \end{pmatrix}$$

where all the quantities in this expression are evaluated at $\mathbf{x}^{(k)} = \{\boldsymbol{\varepsilon}_{n+1}^{e(k)}, -\boldsymbol{\alpha}_{n+1}^{(k)}, \Delta\gamma^{(k)}\}^T$ according to their definitions in Box 1.1.

4. Compute the direction of advance:

aux := 0

IF $\Delta\gamma^{(k)} = 0$ THEN aux := $\mathbf{m}_{\sigma_{n+1}}^{(k)} \cdot (\boldsymbol{\varepsilon}_{n+1}^{e(k)} - \boldsymbol{\varepsilon}_{n+1}^{e,trial}) -$
 $\mathbf{m}_{q_{n+1}}^{(k)} \cdot (\boldsymbol{\alpha}_{n+1}^{(k)} - \boldsymbol{\alpha}_{n+1}^{trial})$

IF aux ≤ 0 THEN

flag := .true.

$\mathbf{d}^{(k)} := -(\mathbf{J}^{(k)})^{-1} \mathbf{r}^{(k)}$

ELSE

flag := .false.

$$[\mathbf{D}^{(k)}]_{ij} := \begin{cases} [(\mathbf{J}^{(k)})^{-1}(\mathbf{J}^{(k)})^{-T}]_{ij} & i, j \neq n_x \text{ or } i = j = n_x \\ 0 & i, j = n_x \text{ and } i \neq j \end{cases}$$

$\mathbf{d}^{(k)} := -\mathbf{D}^{(k)}(\mathbf{J}^{(k)})^T \mathbf{r}^{(k)}$

ENDIF

5. Apply the line search scheme of Box 1.2 to the function $\mathbf{r}(\mathbf{x})$ by (2.1).

INPUT: $\mathbf{x}^{(k)}, \mathbf{r}^{(k)}, \mathbf{d}^{(k)}$ and flag.

OUTPUT: $\mathbf{x}^{(k+1)}$ and $\mathbf{r}^{(k+1)}$, as well as $(\boldsymbol{\sigma}, \mathbf{q})_{n+1}^{(k+1)}$ from the computation of $\mathbf{r}^{(k+1)}$, and other auxiliary quantities used in Item 3. for the Jacobian $\mathbf{J}^{(k+1)}$.

6. Check convergence \rightarrow set $(\boldsymbol{\varepsilon}^e, \boldsymbol{\alpha}, \boldsymbol{\sigma}, \mathbf{q})_{n+1} = (\boldsymbol{\varepsilon}^e, \boldsymbol{\alpha}, \boldsymbol{\sigma}, \mathbf{q})_{n+1}^{(k+1)}$ and EXIT.

7. Set $k \leftarrow k + 1$ and GO TO 3.

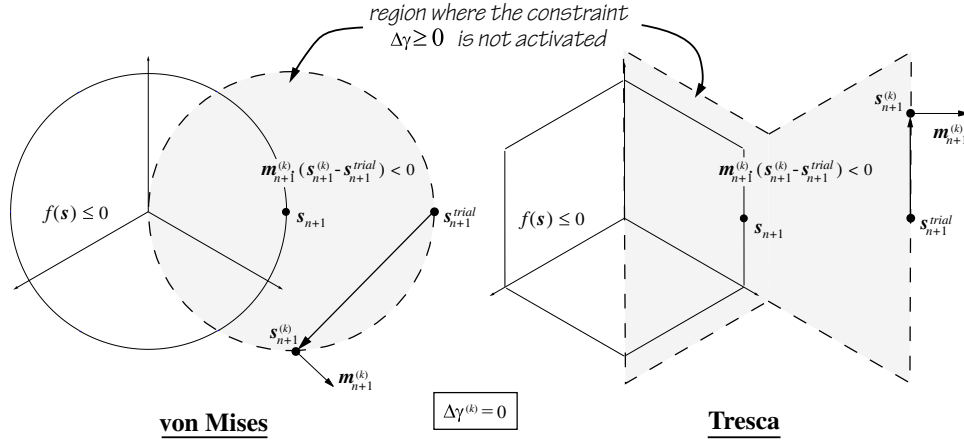


FIGURE 2.1. Graphical interpretation of the condition (2.3) for the **a)** von Mises and **b)** Tresca yield conditions, both with associated perfect plastic flow ($\mathbf{m} = \nabla f$) and constant elasticities. The region of the deviatoric stress plane ($\mathbf{s} := \boldsymbol{\sigma} - \sum_{i=1}^3 [\boldsymbol{\sigma}]_i$) where the constraint $\Delta\gamma \geq 0$ is not activated, leading to the modified Jacobian in the line search scheme, is shown in gray.

on the residually-based descent function presented in Remark I.1 due to the constrained character of the problem. A non-singular Jacobian is implied by the usual assumptions of an associative convex problem (i.e., $\mathbf{m} = \nabla f$ with $\nabla^2 f$ positive semi-definite) and strict convexity of the elastic relations (i.e. $\tilde{\mathbf{G}}$ positive definite), as considered in Part I of this work. Under these assumptions, the equations (2.1) correspond to the first order necessary and sufficient conditions of the convex primal variational problem considered therein (Proposition 3.1, to be specific). The required smoothness follows from the regularity of the material model, that is, the yield function, and elastic and hardening laws. However, the previous ultimate requirements on the Jacobian can be satisfied in more general situations. As a matter of fact, we consider in Section 4 an example involving strain softening. The performance of the algorithm is also assessed in that section for a case involving a non-differentiable residual due to the consideration of a yield function leading to a non-differentiable flow vector. In both cases, the primal-CPPM shows a dramatic improvement in its global convergence properties over the original Newton-CPPM, while exhibiting locally the desired asymptotic quadratic rate of convergence.

Remarks 2.1.

1. Globally convergent primal closest-point projection algorithms can be easily devised for the viscoplastic problem given its unconstrained character; see Section 4 of Part I.

In particular, the reduced residual reads in this case

$$\tilde{\mathbf{r}}_{\hat{\eta}}(\tilde{\mathbf{x}}) = \left\{ \begin{array}{l} \boldsymbol{\varepsilon}_{n+1}^e - \boldsymbol{\varepsilon}_{n+1}^{e,trial} + \frac{1}{\hat{\eta}} g(f_{n+1}) \mathbf{m}_{\sigma_{n+1}} \\ -\boldsymbol{\alpha}_{n+1} + \boldsymbol{\alpha}_{n+1}^{trial} + \frac{1}{\hat{\eta}} g(f_{n+1}) \mathbf{m}_{q_{n+1}} \end{array} \right\}, \quad \text{for } \tilde{\mathbf{x}} := \left\{ \begin{array}{l} \boldsymbol{\varepsilon}_{n+1}^e \\ -\boldsymbol{\alpha}_{n+1} \end{array} \right\}, \quad (2.4)$$

with a viscoplastic parameter $\hat{\eta} = \eta/\Delta t$ and a general viscoplastic function $g(\cdot)$. The plastic multiplier can be easily obtained as $\Delta\gamma = g(f_{n+1})/\hat{\eta}$. In this case, the associated Jacobian reads

$$\tilde{\mathbf{J}}_{\hat{\eta}}^{(k)} = \mathbf{I} + \frac{1}{\hat{\eta}} \left[g(f_{n+1}^{(k)}) \nabla \mathbf{m}_{n+1}^{(k)} + g'(f_{n+1}^{(k)}) \mathbf{m}_{n+1}^{(k)} \otimes \nabla f_{n+1}^{(k)} \right] \tilde{\mathbf{G}}_{n+1}^{(k)}, \quad (2.5)$$

where \otimes denotes the tensor product of two vectors. The regularity of the Jacobian (2.5) is assured, for example, by the usual convexity and associativity assumptions, and the monotonicity of the viscoplastic function $g(\cdot)$. The use of the line search scheme summarized in Section I.1 of Appendix I for unconstrained problems leads directly to a globally convergent scheme under these assumptions.

2. Alternatively, the algorithm presented in this section for the rate-independent problem, involving the plastic multiplier $\Delta\gamma$ as independent variable, can be easily extended to accommodate the viscoplastic problem by replacing the last component of the residual (2.1)₁ by

$$[\mathbf{r}(\mathbf{x})]_{n_x} = g(f_{n+1}) - \hat{\eta} \Delta\gamma. \quad (2.6)$$

The algorithm summarized in Box 2.1 applies then directly, with the Jacobian computed now as

$$\mathbf{J}_{\hat{\eta}}^{(k)} := \begin{pmatrix} \mathbf{I} + \Delta\gamma^{(k)} \nabla \mathbf{m}_{n+1}^{(k)} & \tilde{\mathbf{G}}_{n+1}^{(k)} & \mathbf{m}_{n+1}^{(k)} \\ g'(f_{n+1}^{(k)}) \nabla f_{n+1}^{(k)T} & \tilde{\mathbf{G}}_{n+1}^{(k)} & -\hat{\eta} \end{pmatrix}, \quad (2.7)$$

and the activation condition reading

$$\begin{aligned} \mathbf{m}_{\sigma_{n+1}}^{(k)} \cdot (\boldsymbol{\varepsilon}_{n+1}^{e,(k)} - \boldsymbol{\varepsilon}_{n+1}^{e,trial}) - \mathbf{m}_{q_{n+1}}^{(k)} \cdot (\boldsymbol{\alpha}_{n+1}^{(k)} - \boldsymbol{\alpha}_{n+1}^{trial}) \\ - \hat{\eta} g(f_{n+1}^{(k)}) > 0 \quad \text{with } \Delta\gamma^{(k)} = 0, \end{aligned} \quad (2.8)$$

We observe that the constrained character of the problem is maintained in this approach. \square

2.2. The augmented primal closest-point projection method

The extra considerations and difficulties encountered in the previous section due to the constrained character of the problem can be avoided entirely by considering the alternative

BOX 2.2. Implementation of the augmented form of the primal closest-point projection method (augmented-primal-CPPM).

1. Input data: $\{\boldsymbol{\varepsilon}_{n+1}^{e,trial}, \boldsymbol{\alpha}_{n+1}^{trial}\}$, with the corresponding $\{\boldsymbol{\sigma}_{n+1}^{trial}, \mathbf{q}_{n+1}^{trial}\}$ and $f_{n+1}^{trial} > 0$.

2. Initialization: set $k = 0$,

$$\mathbf{x}_c^{(0)} := \begin{Bmatrix} \boldsymbol{\varepsilon}_{n+1}^{e,trial} \\ -\boldsymbol{\alpha}_{n+1}^{trial} \\ 0 \end{Bmatrix}, \quad \text{and} \quad \mathbf{r}_c^{(0)} := \begin{Bmatrix} cf\mathbf{m}_\sigma \\ cf\mathbf{m}_q \\ f \end{Bmatrix}_{(\boldsymbol{\sigma}_{n+1}^{trial}, \mathbf{q}_{n+1}^{trial})}.$$

3. Compute the Jacobian:

$$\mathbf{J}_c^{(k)} := \begin{pmatrix} \mathbf{I} + \mathbf{H}^{(k)} \tilde{\mathbf{G}}^{(k)} & s^{(k)} \mathbf{m}^{(k)} \\ s^{(k)} \nabla f^{(k)T} \tilde{\mathbf{G}}^{(k)} & \frac{1}{c}(s^{(k)} - 1) \end{pmatrix},$$

where

$$s^{(k)} := \begin{cases} 0, & \Delta\lambda^{(k)} + cf^{(k)} < 0, \\ 1, & \Delta\lambda^{(k)} + cf^{(k)} > 0, \end{cases}$$

$$\mathbf{H}^{(k)} := \langle \Delta\lambda^{(k)} + cf^{(k)} \rangle \nabla \mathbf{m}^{(k)} + c s^{(k)} \mathbf{m}^{(k)} \otimes \nabla f^{(k)},$$

with all the quantities $(\cdot)^{(k)}$ in these expressions evaluated at the current iterate $\mathbf{x}^{(k)} = \{\boldsymbol{\varepsilon}_{n+1}^{e(k)}, -\boldsymbol{\alpha}_{n+1}^{(k)}, \Delta\lambda^{(k)}\}^T$ according to their definitions in Box 1.1.

4. Compute the direction of advance:

$$\mathbf{d}_c^{(k)} := -(\mathbf{J}_c^{(k)})^{-1} \mathbf{r}_c^{(k)}.$$

5. Apply the line search scheme of Box I.1 to the function $\mathbf{r}_c(\mathbf{x})$ by (2.9).

INPUT: $\mathbf{x}_c^{(k)}, \mathbf{r}_c^{(k)}$ and $\mathbf{d}_c^{(k)}$.

OUTPUT: $\mathbf{x}_c^{(k+1)}$ and $\mathbf{r}_c^{(k+1)}$, as well as $(\boldsymbol{\sigma}, \mathbf{q})_{n+1}^{(k+1)}$ from the computation of $\mathbf{r}_c^{(k+1)}$, and other auxiliary quantities used in Item 3. for the Jacobian $\mathbf{J}_c^{(k+1)}$.

6. Check convergence \rightarrow set $(\boldsymbol{\varepsilon}^e, \boldsymbol{\alpha}, \boldsymbol{\sigma}, \mathbf{q})_{n+1} = (\boldsymbol{\varepsilon}^e, \boldsymbol{\alpha}, \boldsymbol{\sigma}, \mathbf{q})_{n+1}^{(k+1)}$ and EXIT.

7. Set $k \leftarrow k + 1$ and GO TO 3.

augmented Lagrangian formulation of the primal problem developed in Section 5 of Part I. In this way, we consider the augmented residual

$$\mathbf{r}_c(\mathbf{x}_c) := \left\{ \begin{array}{c} \boldsymbol{\varepsilon}_{n+1}^e - \boldsymbol{\varepsilon}_{n+1}^{e,trial} + c \langle \frac{\Delta\lambda}{c} + f_{n+1} \rangle \mathbf{m}_{\sigma_{n+1}} \\ -\boldsymbol{\alpha}_{n+1} + \boldsymbol{\alpha}_{n+1}^{trial} + c \langle \frac{\Delta\lambda}{c} + f_{n+1} \rangle \mathbf{m}_{q_{n+1}} \\ \langle \frac{\Delta\lambda}{c} + f_{n+1} \rangle - \frac{\Delta\lambda}{c} \end{array} \right\}, \quad \text{for } \mathbf{x}_c := \left\{ \begin{array}{c} \boldsymbol{\varepsilon}_{n+1}^e \\ -\boldsymbol{\alpha}_{n+1} \\ \Delta\lambda \end{array} \right\}, \quad (2.9)$$

the penalty parameter $c > 0$ and Macaulay brackets $\langle \cdot \rangle$. We have employed the notation $\Delta\lambda$, instead of $\Delta\gamma$, to emphasize the unconstrained character of this scalar variable. The plastic multiplier is simply obtained as

$$\Delta\gamma = \langle \Delta\lambda \rangle = \Delta\lambda > 0, \quad (2.10)$$

for the plastic corrector case of interest ($\Delta\gamma = 0$ otherwise).

As shown in the aforementioned section of Part I, the solution of this new unconstrained system of equations is exactly the same solution as the original equations (2.9). Its solution can be obtained directly with the use of the line search scheme presented in Section I.1 of Appendix I for unconstrained problems. The resulting algorithm is summarized in Box 2.2, and referred to in short as the augmented–primal–CPPM. The numerical simulations presented in Section 5 illustrate the improvement gained in the numerical performance when introducing this augmented regularization. A careful look of the algorithm presented in Box 2.2 reveals a discontinuity of the Jacobian for $\Delta\lambda + cf(\boldsymbol{\sigma}, \mathbf{q}) = 0$. Note that this discontinuity does not occur, however, at the solution, characterized by $\Delta\lambda > 0$ and $f = 0$, for the plastic corrector case of interest. In fact, it has not affected the performance of the scheme in the numerical simulations presented in Section 5. Still, to avoid this theoretical drawback, we develop in the following section dual algorithms that avoid entirely this situation.

3. Dual Algorithms

The algorithms developed in the previous section were based on the direct solution of the Euler-Lagrange equations associated to the primal formulation of the closest-point projection equations. In this way, they considered as primary variables the elastic strain, strain-like internal variables and the plastic multiplier (or its unconstrained counterpart in the associated augmented formulation), while imposing simultaneously the flow rule, the hardening law and the plastic consistency condition.

We develop in this section alternative algorithms based on the dual formulations of the problem developed in Part I of this work. In contrast with the preceding primal algorithms, the resulting numerical schemes involve a separate (or staggered) imposition of the plastic consistency condition. This leads to “two level” algorithms as described next.

3.1. The dual closest-point projection method

The dual formulation of the closest-point projection equations has been characterized in Proposition 3.3 of Part I for the rate-independent problem considered next. In this context, the solution of the closest-point projection equations can be characterized as the root of the scalar equation

$$\bar{f}(\Delta\gamma) := f(\boldsymbol{\sigma}(\Delta\gamma), \mathbf{q}(\Delta\gamma)) = 0, \quad (3.1)$$

in terms of the plastic multiplier $\Delta\gamma \geq 0$ for the plastic corrector step of interest herein ($\Delta\gamma = 0$ automatically, otherwise), and the original yield function $f(\cdot)$ evaluated at $(\boldsymbol{\sigma}(\Delta\gamma), \mathbf{q}(\Delta\gamma))$, the solution of the system of equations $\tilde{\mathbf{r}}(\tilde{\mathbf{x}}) = 0$ where

$$\tilde{\mathbf{r}}(\tilde{\mathbf{x}}) := \left\{ \begin{array}{l} \boldsymbol{\varepsilon}_{n+1}^e - \boldsymbol{\varepsilon}_{n+1}^{e,trial} + \Delta\gamma \mathbf{m}_{\boldsymbol{\sigma}_{n+1}} \\ -\boldsymbol{\alpha}_{n+1} + \boldsymbol{\alpha}_{n+1}^{trial} + \Delta\gamma \mathbf{m}_{\mathbf{q}_{n+1}} \end{array} \right\} \quad \text{for} \quad \tilde{\mathbf{x}} := \left\{ \begin{array}{l} \boldsymbol{\varepsilon}_{n+1}^e \\ -\boldsymbol{\alpha}_{n+1} \end{array} \right\}. \quad (3.2)$$

and a fixed value $\Delta\gamma \geq 0$. The notation “ $(\tilde{\cdot})$ ” is employed hereafter to emphasize the reduced nature of the variables in front of the similar quantities employed in the previous section; see e.g. the definitions in (2.1). We note that the equations (3.2) define an unconstrained system of equations, but the original scalar problem (3.1) is constrained by the unilateral condition

$$\Delta\gamma \geq 0, \quad (3.3)$$

in the plastic multiplier.

The problem reduces then to the solution of the scalar equation (3.1), a problem that we approach again through a Newton scheme to assure its asymptotic quadratic rate of convergence in combination with a line search scheme to assure its global convergence. We refer to this part of the algorithm as the “upper level” of the final scheme, since the evaluation of the consistency function $\bar{f}(\cdot)$ and its derivative requires the solution of the system of equations (3.2). We approach again the solution of these equations through a Newton scheme with a line search technique, and refer to it as the “lower level” of the final scheme. Boxes 3.1 and 3.2 present a summary of the computations involved in these upper and lower phases, respectively. Note that the final solution $\{\boldsymbol{\varepsilon}_{n+1}^e, \boldsymbol{\alpha}_{n+1}\}$ (with its corresponding values $\{\boldsymbol{\sigma}_{n+1}, \mathbf{q}_{n+1}\}$ for the conjugate stress variables) are given by the solution of the lower level scheme of Box 3.2 after convergence of the upper level algorithm of Box 3.1 for the plastic multiplier $\Delta\gamma$.

Concentrating first on the scheme presented in Box 3.2 for the lower level problem, we observe that it consists of a straightforward application of the line search scheme presented in Section I.1 of Appendix I in combination with a Newton solution of the problem. The unconstrained nature of the problem (3.2) leads naturally to this simple approach, avoiding the theoretical difficulties when considering the original constrained primal form of the problem; see Remark I.1 of Appendix I. The advantage gained in this respect when splitting

BOX 3.1. Implementation of the upper level of the dual-CPPM, involving a Newton iteration process in $\Delta\gamma$.

1. Input data: $\{\boldsymbol{\varepsilon}_{n+1}^{e,trial}, \boldsymbol{\alpha}_{n+1}^{trial}\}$, with the corresponding $\{\boldsymbol{\sigma}_{n+1}^{trial}, \mathbf{q}_{n+1}^{trial}\}$ and $f_{n+1}^{trial} > 0$.

2. Initialize: set $k = 0$, $(\boldsymbol{\varepsilon}^e, \boldsymbol{\alpha}, \boldsymbol{\sigma}, \mathbf{q})_{n+1}^{(0)} = (\boldsymbol{\varepsilon}^e, \boldsymbol{\alpha}, \boldsymbol{\sigma}, \mathbf{q})_{n+1}^{trial}$, $\Delta\gamma^{(0)} = 0$ and $\bar{f}^{(0)} = f_{n+1}^{trial}$.

3. Compute update direction:

$$\delta(\Delta\gamma)^{(k)} := \bar{f}^{(k)} / \left(\nabla f^{(k)} \cdot \tilde{\mathbf{G}}^{(k)} (\mathbf{I} + \nabla \mathbf{m}^{(k)} \tilde{\mathbf{G}}^{(k)})^{-1} \mathbf{m}^{(k)} \right) .$$

5. Apply the line search scheme of Box I.1 with the scalar residual and descent function

$$r_{\Delta\gamma}(\Delta\gamma) := \bar{f}(\Delta\gamma), \quad \text{and} \quad M_{\Delta\gamma}(\Delta\gamma) = \frac{1}{2} (\bar{f}(\Delta\gamma))^2$$

with the modified update formula for $\mathbf{x}^{(k)} \leftarrow \Delta\gamma^{(k)}$

$$\Delta\gamma^{(k+1)} := \langle \Delta\gamma^{(k)} + \alpha_{(j)}^{(k)} \delta(\Delta\gamma)^{(k)} \rangle \quad \text{in Box I.1}$$

(that is, including the Macaulay brackets $\langle \cdot \rangle$), and where $\bar{f}(\Delta\gamma) = f(\boldsymbol{\sigma}(\Delta\gamma), \mathbf{q}(\Delta\gamma))$ for the values $\{\boldsymbol{\sigma}(\Delta\gamma), \mathbf{q}(\Delta\gamma)\}$ computed by the lower level algorithm in Box 3.2 for a fixed $\Delta\gamma$.

INPUT: $\Delta\gamma^{(k)}$, $\bar{f}^{(k)}$ and $\delta(\Delta\gamma)^{(k)}$.

OUTPUT: $\Delta\gamma^{(k+1)}$, $\bar{f}^{(k+1)}$, as well as $(\boldsymbol{\varepsilon}^e, \boldsymbol{\alpha}, \boldsymbol{\sigma}, \mathbf{q})^{(k+1)}$ and other auxiliary quantities used in the update formula in **3.**, from the evaluation of $\bar{f}^{(k+1)}$ through the algorithm in Box 3.2 (lower level).

5. Check convergence \rightarrow set $(\boldsymbol{\varepsilon}^e, \boldsymbol{\alpha}, \boldsymbol{\sigma}, \mathbf{q})_{n+1} = (\boldsymbol{\varepsilon}^e, \boldsymbol{\alpha}, \boldsymbol{\sigma}, \mathbf{q})_{n+1}^{(k+1)}$ and EXIT.

6. Set $k \leftarrow k + 1$ and GO TO **3.**

BOX 3.2. Implementation of the lower level of the dual–CPPM.

1. Input data: the fixed values $\boldsymbol{\varepsilon}_{n+1}^{e,trial}$, $\boldsymbol{\alpha}_{n+1}^{trial}$ and $\Delta\gamma^{(k+1)}$, and the initial values $(\boldsymbol{\varepsilon}^e, \boldsymbol{\alpha})_{n+1}^{(k)}$, with $(\boldsymbol{\sigma}, \boldsymbol{q})_{n+1}^{(k)}$.

2. Initialize: set $i = 0$, $\tilde{\boldsymbol{x}}_{(0)} := \left\{ \boldsymbol{\varepsilon}_{n+1}^{e,(k)}, -\boldsymbol{\alpha}_{n+1}^{(k)} \right\}^T$ and $\tilde{\boldsymbol{r}}_{(0)} := \tilde{\boldsymbol{r}}(\tilde{\boldsymbol{x}}_{(0)})$ by (3.2).

3. Compute the Jacobian:

$$\tilde{\boldsymbol{J}}_{(i)} := \boldsymbol{I} + \Delta\gamma^{(k+1)} \nabla \boldsymbol{m}_{(i)} \tilde{\boldsymbol{G}}_{(i)} .$$

4. Compute the direction of advance:

$$\tilde{\boldsymbol{d}}_{(i)} := -(\tilde{\boldsymbol{J}}_{(i)})^{-1} \tilde{\boldsymbol{r}}_{(i)} .$$

5. Apply the line search scheme of Box I.1 to the function $\tilde{\boldsymbol{r}}(\boldsymbol{x})$.

INPUT: $\tilde{\boldsymbol{x}}_{(i)}$, $\tilde{\boldsymbol{r}}_{(i)}$ and $\tilde{\boldsymbol{d}}_{(i)}$.

OUTPUT: $\tilde{\boldsymbol{x}}_{(i+1)}$, and $\tilde{\boldsymbol{r}}_{(i+1)}$, as well as $(\boldsymbol{\sigma}, \boldsymbol{q})_{(i+1)}$ from the computation of $\tilde{\boldsymbol{r}}_{(i+1)}$, and other auxiliary quantities used in Item 3. for the Jacobian $\tilde{\boldsymbol{J}}_{(i)}$.

5. Check convergence \rightarrow set $(\boldsymbol{\varepsilon}^e, \boldsymbol{\alpha}, \boldsymbol{\sigma}, \boldsymbol{q})_{n+1}^{(k+1)} = (\boldsymbol{\varepsilon}^e, \boldsymbol{\alpha}, \boldsymbol{\sigma}, \boldsymbol{q})_{(i+1)}$ and EXIT.

7. Set $i \leftarrow i + 1$ and GO TO 3.

the problem in this way becomes then apparent. We also note that the Jacobian $\tilde{\boldsymbol{J}}_{(i)}$ used in this iterative process and included in Box 3.2 is non-singular (in fact, positive definite) under the usual assumptions of convexity (i.e., positive definite $\tilde{\boldsymbol{G}}$) and associativity with a convex yield function (i.e., $\nabla m = \nabla^2 f$ positive semi-definite). This situation, together with the smoothness of the residual (3.2)₁ as implied by the material model, assures the global convergence of the proposed scheme.

The upper level algorithm of Box 3.1 reduces to the solution of the scalar equation (3.1), constrained by the non-negative character of its argument as given by (3.3). The scalar nature of the problem allows the straightforward imposition of this constraint through the simple Newton update formula

$$\Delta\gamma^{(k+1)} = \langle \Delta\gamma^{(k)} + \alpha^{(k)} \delta(\Delta\gamma)^{(k)} \rangle , \quad \text{with} \quad \delta(\Delta\gamma)^{(k)} = -\bar{f}^{(k)} / \bar{f}'^{(k)} , \quad (3.4)$$

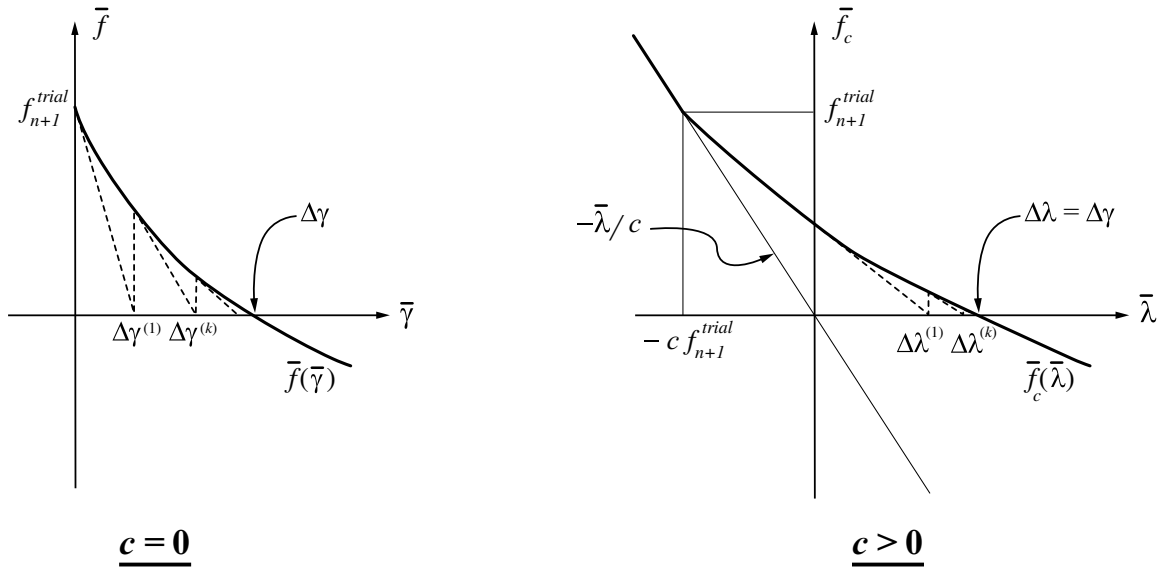


FIGURE 3.1. Graphical interpretation of the upper level scheme of the dual-CPPM for the non-augmented ($c = 0$) and augmented ($c > 0$) formulations.

for an typical iteration (k) in terms again of the Maucalay brackets $\langle \cdot \rangle$. The derivative \bar{f}' in (3.4) is obtained in closed-form using the equations (3.1) and (3.2) as

$$\bar{f}' = -\nabla f \cdot \left[\tilde{\mathbf{G}}^{-1} + \Delta\gamma \nabla \mathbf{m} \right]^{-1} \mathbf{m} . \quad (3.5)$$

At the boundary $\Delta\gamma = 0$ of the admissible set, this derivative reduces to the value

$$\bar{f}' \Big|_{\Delta\gamma=0} = -\nabla f \cdot \tilde{\mathbf{G}} \mathbf{m} < 0 \quad \text{strictly} , \quad (3.6)$$

given the fundamental assumption of the underlying continuum model (see Box 1.1), even in the general non-convex (e.g. with strain softening) and non-associated plastic flow ($\mathbf{m} \neq \nabla f$). This important result implies that even though the iteration process (3.4) may lead to the value $\Delta\gamma^{(k)} = 0$ at some iteration (k), the constraint itself is not activated, that is, the iteration direction (3.4)₂ leads naturally to $\Delta\gamma^{(k+1)} > 0$ and no modified advancing rules like (I.17) in Appendix I are needed. This situation, together with the aforementioned unconstrained character of the problem in the lower level, avoids altogether the need for the use of complex line search rules as required in the constrained primal formulation presented in Section 2.1.

The global convergence of the upper level algorithm defined by the iterative process (3.4) is then assured if the derivative in (3.5) is continuous and does not vanish. The smoothness condition is again implied by the proper smoothness of the material model, that is, the yield surface and elastic and hardening laws. The non-zero condition on the derivative is satisfied under the usual assumptions of convexity and associated plastic

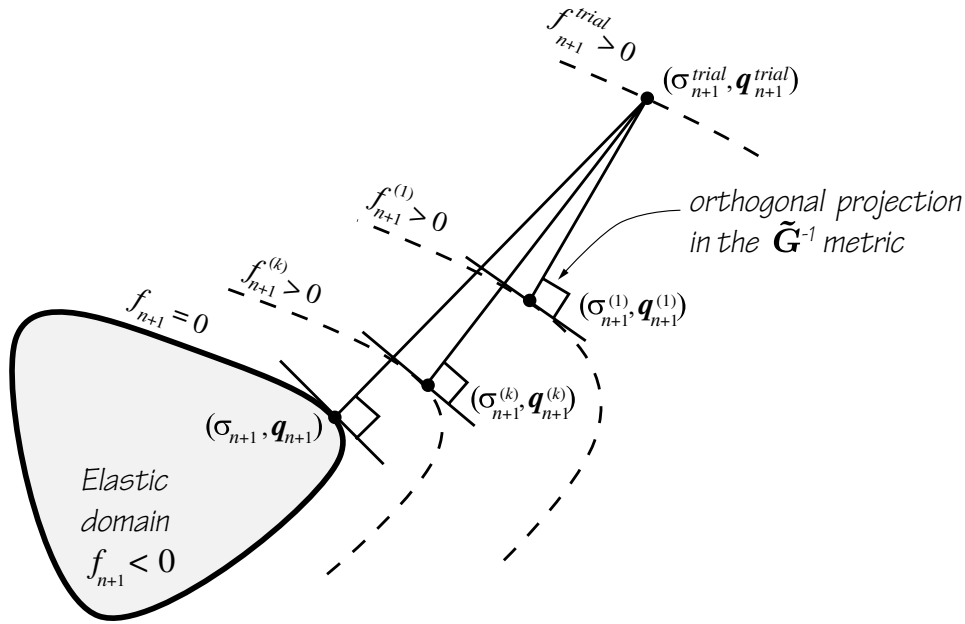


FIGURE 3.2. Graphical interpretation of both the dual-CPPM and the augmented-dual-CPPM. The stress variables $\{\boldsymbol{\sigma}_{n+1}^{(k)}, \mathbf{q}_{n+1}^{(k)}\}$ at each iteration (k) are the closest-point projection onto the current iterate of the yield function $\bar{f}(\Delta\gamma^{(k)})$ (or $\bar{f}_c(\Delta\lambda^{(k)})$ for the augmented algorithm) for the plastic multiplier $\Delta\gamma^{(k)}$ (or $\Delta\lambda^{(k)}$) obtained by the upper level scheme. A similar figure can be found in the literature but erroneously associated with the original Newton-CPPM of Box 1.1.

flow. Under these assumptions, equation (3.5) reveals that the function $\bar{f}(\Delta\gamma)$ is strictly monotonically decreasing ($\bar{f}' < 0$) as obtained in Part I of this work. Figure 3.1 illustrates these results graphically. Under these conditions, the line search scheme considered in this upper level scheme did not need to be activated in the numerical examples reported in Section 5, but its consideration is needed to assure the global convergence of the iterative process in general situations.

Therefore, we conclude that the proposed two level scheme based on the dual form of the closest-point projection equations is globally convergent under these assumptions. The numerical examples presented in Section 5 have confirmed this property. Figure 3.2 depicts graphically the idea behind the proposed dual-CPPM for the associated case given by the normality rule $\mathbf{m} = \nabla f$, and constant elasticities and linear hardening (i.e. $\tilde{\mathbf{G}} = \text{constant}$). Equations (3.2) imply in this case that in a given iteration of the upper level scheme, that is, for each value $\Delta\gamma^{(k)}$, the vector $\boldsymbol{\Sigma}_{n+1}^{(k)} - \boldsymbol{\Sigma}_{n+1}^{trial}$ in stress space (for $\boldsymbol{\Sigma} = \{\boldsymbol{\sigma}, \mathbf{q}\}$) is indeed normal in the metric $\tilde{\mathbf{G}}^{-1}$ to the current value of the yield surface $f^{(k)}$. This property is illustrated in Figure 3.2, showing each iteration value of the stress variables as the closest-point projection on the elastic domain $f_{n+1}^{(k)} = \bar{f}(\Delta\gamma^{(k)}) \leq 0$ for the current iterate $\Delta\gamma^{(k)}$ in the upper level algorithm depicted in Figure 3.1. We note that a similar figure can

be found in SIMO & HUGHES [1998], among others, and it is erroneously associated with the original Newton–CPPM. The developments presented in this section clearly identify the approach depicted in this figure with the newly proposed algorithm based on the dual formulation of the governing equations.

Remark 3.1. The dual–CPPM described in this section extends to the viscoplastic problem, following the developments of the dual formulation of this problem presented in Proposition 4.3 of Part I. That is, simply replace the scalar equation (3.1) by the relation

$$g(\bar{f}(\Delta\gamma)) - \hat{\eta} \Delta\gamma = 0, \quad (3.7)$$

for a general viscoplastic function $g(\cdot)$ and viscoplastic parameter $\hat{\eta} \geq 0$. We observe that this is the only needed modification, since the problem (3.2) is not changed, with the lower level algorithm of Box 3.2 applying entirely to the viscoplastic problem as well. Similarly, the same considerations regarding the non-activation of the constraint $\Delta\gamma = 0$ and, indeed, the same global convergence properties apply under the usual monotonicity assumption of the viscoplastic function $g(\cdot)$. Additional details are omitted. \square

3.2. The augmented dual closest-point projection method

Even though the constrained character of the upper level problem in the dual scheme considered in the previous section was shown not to affect the algorithm itself, the consideration of augmented Lagrangian extensions avoiding altogether this constraint leads to algorithms improving on their numerical performance, as illustrated in the numerical examples presented in Section 5. Following the developments of the dual augmented Lagrangian formulation summarized in Proposition 5.2 of Part I, the plastic consistency function $\bar{f}(\cdot)$ in (3.1) is replaced by

$$\bar{f}_c(\Delta\lambda) := f(\boldsymbol{\sigma}_c(\Delta\lambda), \mathbf{q}_c(\Delta\lambda)) = 0, \quad (3.8)$$

with $\{\boldsymbol{\sigma}_c(\Delta\lambda), \mathbf{q}_c(\Delta\lambda)\}$ defined by the augmented lower level problem $\tilde{\mathbf{r}}_c(\tilde{\mathbf{x}}) = 0$ for the augmented residual

$$\tilde{\mathbf{r}}_c(\tilde{\mathbf{x}}) = \left\{ \begin{array}{l} \boldsymbol{\varepsilon}_{n+1}^e - \boldsymbol{\varepsilon}_{n+1}^{e,trial} + \langle \Delta\lambda + c f(\boldsymbol{\sigma}_{n+1}, \mathbf{q}_{n+1}) \rangle \mathbf{m}_{\sigma_{n+1}} \\ -\boldsymbol{\alpha}_{n+1} + \boldsymbol{\alpha}_{n+1}^{trial} + \langle \Delta\lambda + c f(\boldsymbol{\sigma}_{n+1}, \mathbf{q}_{n+1}) \rangle \mathbf{m}_{q_{n+1}} \end{array} \right\}, \quad (3.9)$$

for a penalty parameter $c \geq 0$ and in terms, again, of the primary unknowns $\tilde{\mathbf{x}} := \{\boldsymbol{\varepsilon}_{n+1}^e, -\boldsymbol{\alpha}_{n+1}\}^T$. Following the same notation employed in the primal augmented Lagrangian formulations of Section 2.2, we denote the scalar field appearing in these equations by $\Delta\lambda$ emphasizing its entirely unconstrained character in front of $\Delta\gamma \geq 0$. The final plastic multiplier $\Delta\gamma$ is recovered by the simple relation

$$\Delta\gamma = \langle \Delta\lambda \rangle, \quad (3.10)$$

BOX 3.3. Implementation of the upper level of the augmented–dual–CPPM, involving a Newton iterative process in $\Delta\lambda$.

1. Input data: $\{\boldsymbol{\varepsilon}_{n+1}^{e,trial}, \boldsymbol{\alpha}_{n+1}^{trial}\}$, with the corresponding $\{\boldsymbol{\sigma}_{n+1}^{trial}, \mathbf{q}_{n+1}^{trial}\}$ and $f_{n+1}^{trial} > 0$.

2. Initialize: set $k = 0$, $(\boldsymbol{\varepsilon}^e, \boldsymbol{\alpha}, \boldsymbol{\sigma}, \mathbf{q})_{n+1}^{(0)} = (\boldsymbol{\varepsilon}^e, \boldsymbol{\alpha}, \boldsymbol{\sigma}, \mathbf{q})_{n+1}^{trial}$, $\Delta\lambda^{(0)} = 0$ and $\bar{f}_c^{(0)} = f_{n+1}^{trial}$.

3. Compute update direction:

$$\delta(\Delta\lambda)^{(k)} := \bar{f}^{(k)} / \left(\nabla f^{(k)} \cdot \tilde{\mathbf{G}}^{(k)} (\mathbf{I} + \mathbf{H}^{(k)} \tilde{\mathbf{G}}^{(k)})^{-1} \mathbf{m}^{(k)} \right),$$

where

$$s^{(k)} := \begin{cases} 0, & \text{for } \Delta\lambda^{(k)} + cf^{(k)} < 0, \\ 1, & \text{for } \Delta\lambda^{(k)} + cf^{(k)} > 0, \end{cases}$$

$$\mathbf{H}^{(k)} := \langle \Delta\lambda^{(k)} + cf^{(k)} \rangle \nabla \mathbf{m}^{(k)} + c s^{(k)} \mathbf{m}^{(k)} \otimes \nabla f^{(k)}.$$

5. Apply the line search scheme of Box I.1 with the scalar residual and descent function

$$r_{c\Delta\lambda}(\Delta\lambda) := \bar{f}_c(\Delta\lambda), \quad \text{and} \quad M_{c\Delta\lambda}(\Delta\lambda) = \frac{1}{2} (\bar{f}_c(\Delta\lambda))^2$$

for $\mathbf{x}^{(k)} \leftarrow \Delta\lambda^{(k)}$, and where $\bar{f}_c(\Delta\lambda) = f(\boldsymbol{\sigma}_c(\Delta\lambda), \mathbf{q}_c(\Delta\lambda))$ for the values $\{\boldsymbol{\sigma}_c(\Delta\lambda), \mathbf{q}_c(\Delta\lambda)\}$ computed by the lower level algorithm in Box 3.4 for a fixed $\Delta\lambda$.

INPUT: $\Delta\lambda^{(k)}$, $\bar{f}_c^{(k)}$ and $\delta(\Delta\lambda)^{(k)}$.

OUTPUT: $\Delta\lambda^{(k+1)}$, $\bar{f}_c^{(k+1)}$, as well as $(\boldsymbol{\varepsilon}^e, \boldsymbol{\alpha}, \boldsymbol{\sigma}, \mathbf{q})_{n+1}^{(k+1)}$ and other auxiliary quantities used in the update formula in **3.**, from the evaluation of $\bar{f}_c^{(k+1)}$ through the algorithm in Box 3.4 (lower level).

5. Check convergence \rightarrow set $(\boldsymbol{\varepsilon}^e, \boldsymbol{\alpha}, \boldsymbol{\sigma}, \mathbf{q})_{n+1} = (\boldsymbol{\varepsilon}^e, \boldsymbol{\alpha}, \boldsymbol{\sigma}, \mathbf{q})_{n+1}^{(k+1)}$ and EXIT.

6. Set $k \leftarrow k + 1$ and GO TO **3.**

BOX 3.4. Implementation of the lower level of the augmented–dual–CPPM.

1. Input data: the fixed values $\boldsymbol{\varepsilon}_{n+1}^{e,trial}$, $\boldsymbol{\alpha}_{n+1}^{trial}$ and $\Delta\lambda^{(k+1)}$, and the initial values $(\boldsymbol{\varepsilon}^e, \boldsymbol{\alpha})_{n+1}^{(k)}$, with $(\boldsymbol{\sigma}, \boldsymbol{q})_{n+1}^{(k)}$.

2. Initialize: set $i = 0$, $\tilde{\boldsymbol{x}}_{(0)} := \left\{ \boldsymbol{\varepsilon}_{n+1}^{e,(k)}, -\boldsymbol{\alpha}_{n+1}^{(k)} \right\}^T$ and $\tilde{\boldsymbol{r}}_{c(0)} := \tilde{\boldsymbol{r}}_c(\tilde{\boldsymbol{x}}_{(0)})$ by (3.9).

3. Compute the Jacobian:

$$\tilde{\boldsymbol{J}}_{c(i)} := \boldsymbol{I} + \left(\langle \Delta\lambda^{(k+1)} + c f_{(i)} \rangle \nabla \boldsymbol{m}_{(i)} + c s_{(i)} \boldsymbol{m}_{(i)} \otimes \nabla f_{(i)} \right) \tilde{\boldsymbol{G}}_{(i)},$$

where

$$s_{(i)} := \begin{cases} 0, & \Delta\lambda^{(k+1)} + c f_{(i)} < 0, \\ 1, & \Delta\lambda^{(k+1)} + c f_{(i)} > 0. \end{cases}$$

4. Compute the direction of advance:

$$\tilde{\boldsymbol{d}}_{c(i)} := -(\tilde{\boldsymbol{J}}_{c(i)})^{-1} \tilde{\boldsymbol{r}}_{c(i)}.$$

5. Apply the line search scheme of Box I.1 based on the function $\tilde{\boldsymbol{r}}_c(\boldsymbol{x})$.

INPUT: $\tilde{\boldsymbol{x}}_{(i)}$, $\tilde{\boldsymbol{r}}_{c(i)}$ and $\tilde{\boldsymbol{d}}_{c(i)}$.

OUTPUT: $\tilde{\boldsymbol{x}}_{(i+1)}$, and $\tilde{\boldsymbol{r}}_{c(i+1)}$, as well as $(\boldsymbol{\sigma}, \boldsymbol{q})_{(i+1)}$ from the computation of $\tilde{\boldsymbol{r}}_{c(i+1)}$, and other auxiliary quantities used in Item 3. for the Jacobian $\tilde{\boldsymbol{J}}_{c(i)}$.

6. Check convergence \rightarrow set $(\boldsymbol{\varepsilon}^e, \boldsymbol{\alpha}, \boldsymbol{\sigma}, \boldsymbol{q})_{n+1}^{(k+1)} = (\boldsymbol{\varepsilon}^e, \boldsymbol{\alpha}, \boldsymbol{\sigma}, \boldsymbol{q})_{(i+1)}$ and EXIT.

7. Set $i \leftarrow i + 1$ and GO TO 3.

corresponding actually to $\Delta\lambda > 0$ in the plastic corrector step of interest. We observe that the original dual problem (3.1)–(3.2) is recovered for $c = 0$. The solution of the upper and lower problems defined by (3.8) and (3.9), respectively, is approached again with Newton schemes in combination with the unconstrained line search technique presented in Section I.1. The final scheme is summarized in Boxes 3.3 and 3.4 for the upper and lower level algorithms, respectively.

The fully unconstrained character of the problem in the upper level of the algorithm

leads to the direct consideration of the line search scheme of Box I.1 without the need of the added imposition of the non-negative constraint on $\Delta\gamma$ by (3.4)₁ for the previous constrained dual formulation. The derivative of the augmented plastic consistency function (3.8) can also be obtained in closed-form after using equations (3.9) of the lower level augmented problem as

$$\bar{f}'_c = -\nabla f \cdot \left[\tilde{\mathbf{G}}^{-1} + \mathbf{H} \right]^{-1} \mathbf{m} . \quad (3.11)$$

where

$$\mathbf{H} := \langle \Delta\lambda + cf \rangle \nabla \mathbf{m} + c s \mathbf{m} \otimes \nabla f , \quad (3.12)$$

for

$$s := \begin{cases} 0 , & \text{for } \Delta\lambda + cf < 0 , \\ 1 , & \text{for } \Delta\lambda + cf > 0 . \end{cases} \quad (3.13)$$

Even though no problems have been observed in the actual numerical simulations due to the discontinuity of s at $\Delta\lambda + cf = 0$ (in fact, values $\Delta\lambda + cf < 0$ are never reached), we assign the value $s = 0$ at this point. We can conclude from these results the the same properties of the augmented plastic consistency function $\bar{f}'_c(\Delta\lambda)$ as its counterpart $\bar{f}'(\Delta\gamma)$ in the original constrained dual formulation; additional details are omitted. In particular, its strictly monotonically decreasing character (i.e., $\bar{f}'_c < 0$) is concluded under the usual convexity and associativity assumptions. The same globally convergent character of the proposed scheme is concluded in these cases.

We also observe that the augmented–dual–CPPM developed in this section has the same graphical interpretation depicted in Figure 3.2 for the non-augmented dual algorithms (i.e $c = 0$). The upper level algorithm involves, however, a regularized consistency function, a situation that has been depicted in Figure 3.1 for $c > 0$. As argued in the end of Remark 3.2 below and verified in the numerical examples presented in Section 5, this simple modification leads to some improvement in the computational performance of the dual algorithms considered in this section.

Remark 3.2. We observe that by considering the initial estimate of the upper level algorithm by $\Delta\lambda^{(0)} = 0$, the first solution of the lower level problem (3.9) obtained by the scheme in Box 3.4 corresponds to the solution of a viscoplastic problem defined by the viscoplastic parameter $c = 1/\hat{\eta}$ and linear viscoplastic model $g(f) = \langle f \rangle$. In fact, this problem corresponds to the primal formulation of the viscoplastic problem considered in Remark 2.1 above for this case. The consideration of more general viscoplastic models is easily accomplished through the use of augmented formulations based on the corresponding regularization function $g(\cdot)$ as presented in Remark 5.1.2 (that is, replace $\langle \cdot \rangle$ by $g(\cdot)$ in the relations of Box 3.4). In this viscoplastic case, the equation (3.10) giving the plastic multiplier $\Delta\gamma$ is to be replaced by the viscous relation

$$\Delta\gamma = \frac{1}{\hat{\eta}} g(\bar{f}'_c(0)) . \quad (3.14)$$

Therefore, the choice $c = 1/\widehat{\eta}$ leads the final solution of the viscoplastic problem in a single iteration of the upper level algorithm. If the viscoplastic problem is understood as the penalty regularization of the rate-independent problem as $\widehat{\eta} \rightarrow 0$, the improvement in the computational performance gained by the consideration of a large regularization parameter c is to be expected when solving the limit rate-independent problem. The usual considerations on the well-conditioning of the resulting problem is to be weighed in the argument, as it is investigated through the numerical examples presented in Section 5 below. \square

4. Numerical Assessment: Primal Algorithms

We assess in this section the numerical performance of the new primal algorithms proposed in Section 2. More specifically, it is our interest to evaluate the global convergence properties of these schemes. To this purpose, we study in Section 4.1 the convergence properties of the proposed schemes for a single increment (from, say, t_n to t_{n+1}) for different imposed strain increments. Section 4.2 evaluates the overall performance of the schemes in a given imposed path of the deformation gradient, involving different numbers of time increments.

Remarks 4.1.

1. The results presented below are expressed in terms of the invariants

$$p_* = -\frac{I_1(*)}{3}, \quad q_* = \sqrt{3J_2(*)} \quad \text{and} \quad \theta_* = \frac{1}{3} \arccos \left(\frac{3\sqrt{3}J_3(*)}{2J_2(*)^{3/2}} \right), \quad (4.1)$$

of a generic second order tensor $*$, where $I_1(*)$, $J_2(*)$ and $J_3(*)$ denote the first invariant of $*$ and the second and third invariants of the deviatoric part of $*$, $[\text{dev}(*)]_i = [*]_i + p_*$, respectively,

$$I_1(*) = \sum_{i=1}^3 [*]_i, \quad J_2(*) = \frac{1}{2} \sum_{i=1}^3 ([\text{dev}(*)]_i)^2 \quad \text{and} \quad J_3(*) = \prod_{i=1}^3 [\text{dev}(*)]_i, \quad (4.2)$$

in terms of the three principal points $[*]_i$ for $i = 1, 2, 3$. The function θ_* corresponds to the so-called Lode's angle and varies from 0° to 60° . These expressions are used for the Kirchhoff principal stresses $* = \boldsymbol{\sigma}$ and the logarithmic principal elastic strains $* = \boldsymbol{\varepsilon}^e$; see Section 2.3 of Part I of this work.

2. All the contour plots presented in this and subsequent sections (see e.g. Figure 4.1) have been obtained with a uniform grid of 80×80 sampling values, independently of the ranges of the variables depicted in both axis.

3. In all the examples presented in this paper, the convergence of the algorithm is detected through the expression

$$e_{\hat{\boldsymbol{x}}}^{(k)} = \frac{\|\hat{\boldsymbol{x}}^{(k+1)} - \hat{\boldsymbol{x}}^{(k)}\|_{\infty}}{\|\hat{\boldsymbol{x}}^{(k+1)}\|_{\infty}} \leq \text{TOL}_{\hat{\boldsymbol{x}}} \quad (4.3)$$

measuring the relative error in iteration $(k + 1)$ in the maximum norm $\|\cdot\|_{\infty} = \max_i |[\cdot]_i|$, for each component $[\cdot]_i$ despite they may have different dimensions, in general. Here $\hat{\boldsymbol{x}}$ refers the driving variable employed in the particular algorithm under consideration (that is, \boldsymbol{x} given by (2.1) in the primal algorithms, $\tilde{\boldsymbol{x}}$ given by (3.2) in the lower level of the dual algorithms, and $\Delta\gamma$ or $\Delta\lambda$ in the upper level of the dual algorithms). The tolerance value of $\text{TOL}_{\hat{\boldsymbol{x}}} = 10^{-12}$ has been employed in all cases. \square

4.1. Single increment tests

We evaluate in this section the convergence properties of the iterative schemes under investigation during a plastic corrector step for an imposed trial elastic state. The initial state is assumed elastic (i.e., vanishing initial values of the plastic internal variables) with vanishing strain. Deviatoric and pressure dependent models are considered in Sections 4.1.1 and 4.1.2, respectively, both in combination of perfect plasticity and Hencky's hyperelastic law, resulting in a set of constant elasticities in the logarithmic principal elastic strains $\boldsymbol{\varepsilon}^e$; see Appendix II. The imposed trial state is then characterized in the deviatoric Π -plane by the corresponding Lode angle $\theta_{\boldsymbol{\varepsilon}^e, \text{trial}} (= \theta_{\sigma^{\text{trial}}})$ and the radial measure $q_{\boldsymbol{\varepsilon}^e, \text{trial}} (= q_{\sigma^{\text{trial}}}/2\mu$ for the shear modulus μ). The pressure parameter $p_{\boldsymbol{\varepsilon}^e, \text{trial}} (= p_{\sigma^{\text{trial}}}/3\kappa$ for the bulk modulus κ) defines completely the imposed trial state in the pressure-dependent models considered in Section 4.1.2.

4.1.1. Deviatoric plastic models

We consider first the von Mises–Tresca type yield surfaces described in Section II.2 of Appendix II, defining in terms of the material parameter m a family of deviatoric yield surfaces exhibiting different levels of curvature, as it is of the interest in this work. In particular, the choice $m = 0$ corresponds to the smooth von Mises circular cylinder, with higher values of m leading to increasing of the curvature of this yield surface at $\theta_{\sigma} = 0, 30$ (the Tresca non-smooth yield surface is recovered for $m \rightarrow \infty$). Only the two deviatoric parameters $q_{\boldsymbol{\varepsilon}^e, \text{trial}}$ and $\theta_{\boldsymbol{\varepsilon}^e, \text{trial}}$ are needed in this case to define the trial state. Because of the symmetry of the resulting yield functions (see Figure II.1 in Appendix II), Lode angles between 0° and 30° need only to be considered. The values of $\kappa = 164.206 \text{ kN/mm}^2$ and $\mu = 80.1938 \text{ kN/mm}^2$ are taken for the bulk and shear modulus, respectively, in Hencky's law (II.2)-(II.3), with the constant yield stress $\sigma_{y_0} = 0.45 \text{ kN/mm}^2$.

Figure 4.1 compares the performance of the Newton–CPPM and the primal–CPPM in this case. The number of iterations needed for convergence of both schemes for several

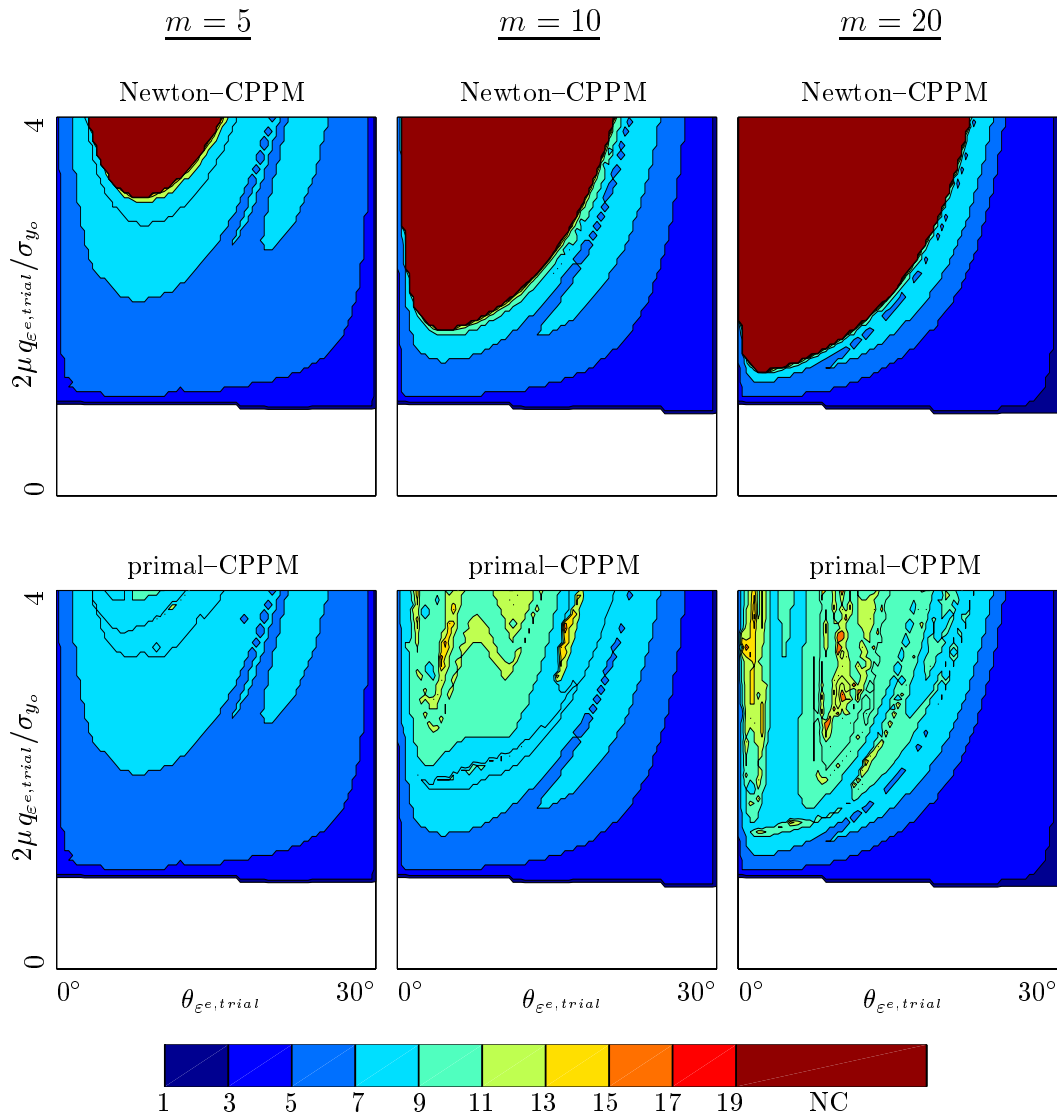


FIGURE 4.1. Single increment tests: deviatoric plastic models. Number of iterations needed for convergence by the Newton-CPPM and the primal-CPPM for three different von Mises-Tresca type yield surfaces ($m = 5, 10$ and 20). “NC” denotes no convergence after more than 100 iterations; extended tests in these regions lead to no convergence after several hundreds of iterations.

elastic trial states $\{q_{\varepsilon^e, trial}, \theta_{\varepsilon^e, trial}\}$ and different values of the material parameter m are depicted in this figure. The regions where no convergence is detected after more than 100 iterations are denoted by “NC”; extended simulations show no convergence after several hundreds of iterations in these regions. The value of $q_{\varepsilon^e, trial}$ varies in the range $[0, 4 \cdot \sigma_{y_0}/(2\mu)]$, that is, with corresponding trial stress states up to four times the yield limit σ_{y_0} .

The results depicted in Figure 4.1 reveal that no convergence is detected with the

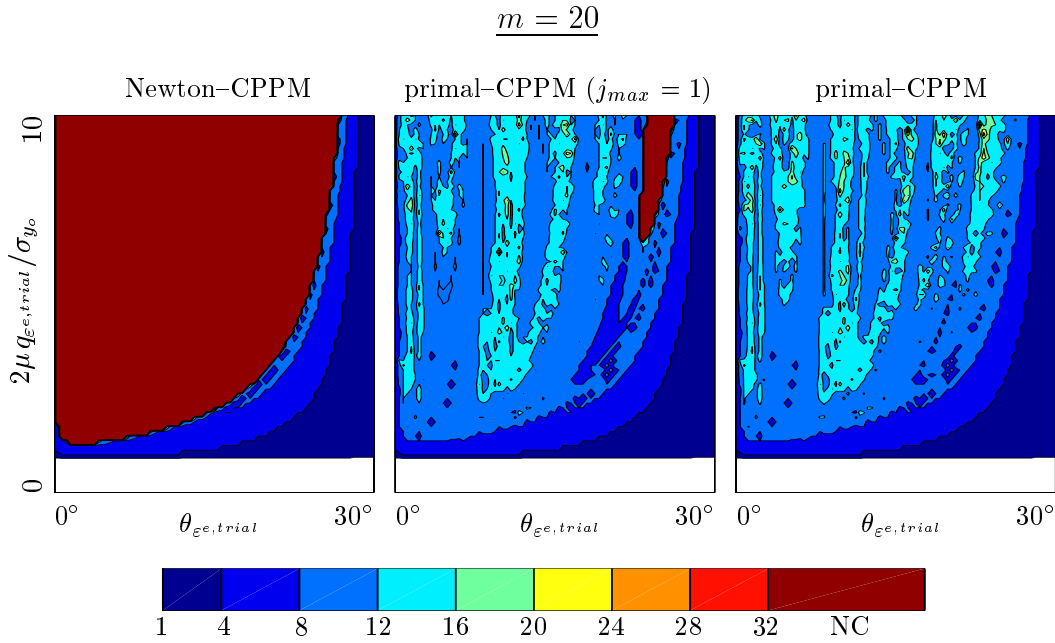


FIGURE 4.2. Single increment tests: deviatoric plastic models ($m = 20$). Number of iterations needed for convergence by the Newton–CPPM and the primal–CPPM (with a maximum of one curve fitting ($j_{max} = 1$), and without a limit on the number of curve fittings) for large excursions outside the elastic domain.

standard Newton–CPPM when the solution is close to $\theta_{\varepsilon^e, trial} = 0^\circ$ (and 60°). As noted above, these values correspond to points where the curvature of the yield surface is higher. Moreover, as m increases the size of the region of no convergence increases. In fact, the Newton–CPPM becomes basically useless even for moderate values of m . With the primal–CPPM these regions of no convergence are avoided. Convergence is attained for any trial state, with less than 17 iterations everywhere. This improvement is observed mainly in the regions of no convergence of the original Newton–CPPM wherever the Newton–CPPM converges, the primal–CPPM does not reduce the number of iterations sensibly. Note also that for $\theta_{\varepsilon^e, trial}$ exactly equal to 0° (and 60°) the convergence is achieved always in a reduced number of iterations. This very special situation is due to the fact that the gradient of the yield surface has always the same direction at these Lode angles.

Both schemes are compared again in Figure 4.2, but with the added consideration of the maximum number of curve fittings in the line search scheme employed in the primal–CPPM, that is, the j_{max} parameter in Boxes I.1 and I.2 of Appendix I. Larger excursions outside the elastic domain, in the range $[0, 10 \cdot \sigma_{y_0} / (2\mu)]$ for the radial measure $q_{\varepsilon^e, trial}$, are also considered. We observe that the primal–CPPM without a limit in the number of curve fittings per iteration avoids completely the regions of no convergence of the original Newton–CPPM. The maximum number of curve fittings needed is only two, though. The small region of no convergence remaining far from the yield surface with a limit of just one

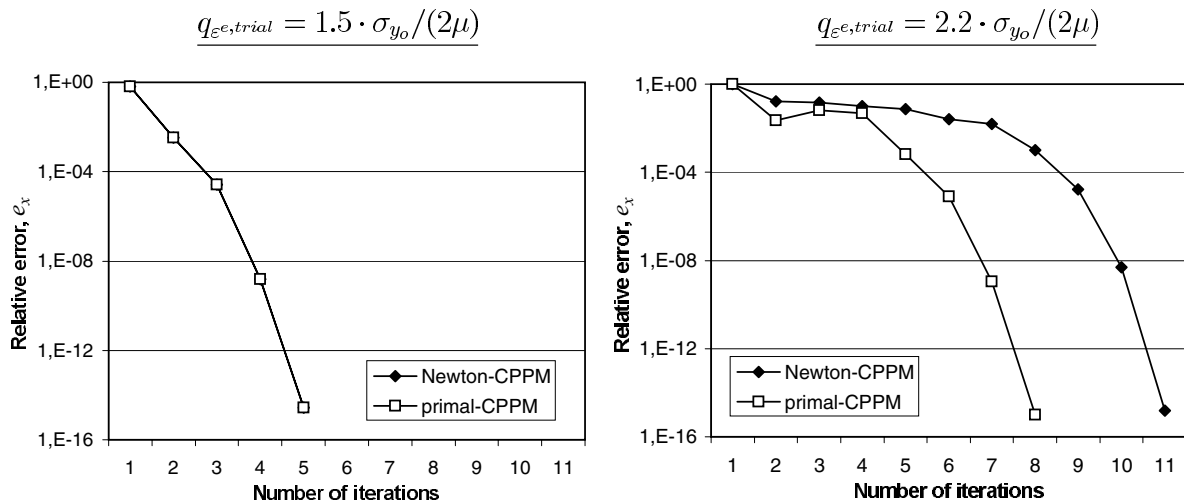


FIGURE 4.3. Single increment tests: deviatoric plastic models ($m = 20$). Convergence results with the primal-CPPM for elastic trial states at $\theta_{\epsilon^{e,trial}} = 15^\circ$ and $q_{\epsilon^{e,trial}} = 1.5, 2.2 \cdot \sigma_{y_0} / (2\mu)$. The solutions with the Newton-CPPM and the primal-CPPM coincide for the case $q_{\epsilon^{e,trial}} = 1.5$.

fitting ($j_{max} = 1$) illustrates the (small) dependence of the scheme on this parameter.

We have also observed that the value of the Goldstein's parameter $\beta \in (0, 1/2)$ (see Box I.1 of Appendix I) does not have a significant influence in the convergence results reported herein. The default value $\beta = 10^{-4}$ has been used in the previous results. With $\beta = 0.49$, that is with a more demanding test for the line search parameter, the overall behavior of the primal-CPPM is the same, with minor modifications: the maximum number of curve fittings per iteration may increase to three, and some minor variations in the number of iterations may be found.

Detailed evolutions of the iterative process for specific tests involving plastic correction are depicted in Figures 4.3 and 4.4. The evolution of the relative error $e_x^{(k)}$ in $\mathbf{x} = \{\boldsymbol{\epsilon}_{n+1}^e, \Delta\boldsymbol{\gamma}\}$, defined by equation (4.3), is shown. We note again that the tolerance has been fixed to 10^{-12} ; see Remark 4.1.3. Figure 4.4 includes the values of the line search parameter, $\alpha^{(k)}$, and the number of quadratic curve fittings per iteration. The trial states correspond to the tests with $\theta_{\epsilon^{e,trial}} = 15^\circ$ and $q_{\epsilon^{e,trial}} = 1.5, 2.2, 4, 7$ and $10 \cdot \sigma_{y_0} / (2\mu)$ (the first two cases are depicted in Figure 4.3, with the last three in Figure 4.4).

For trial states close to the yield surface, as depicted in Figure 4.3, the line search scheme is either not activated (case $q_{\epsilon^{e,trial}} = 1.5 \cdot \sigma_{y_0} / (2\mu)$), or it just results in a little improvement (case $q_{\epsilon^{e,trial}} = 2.2 \cdot \sigma_{y_0} / (2\mu)$). The asymptotic quadratic rate of convergence is also verified. As expected, the final results corresponding to Figure 4.3 are the same for both algorithms. For the cases depicted in Figure 4.4, involving large excursions outside the elastic domain, the asymptotic rate of convergence of the primal-CPPM is

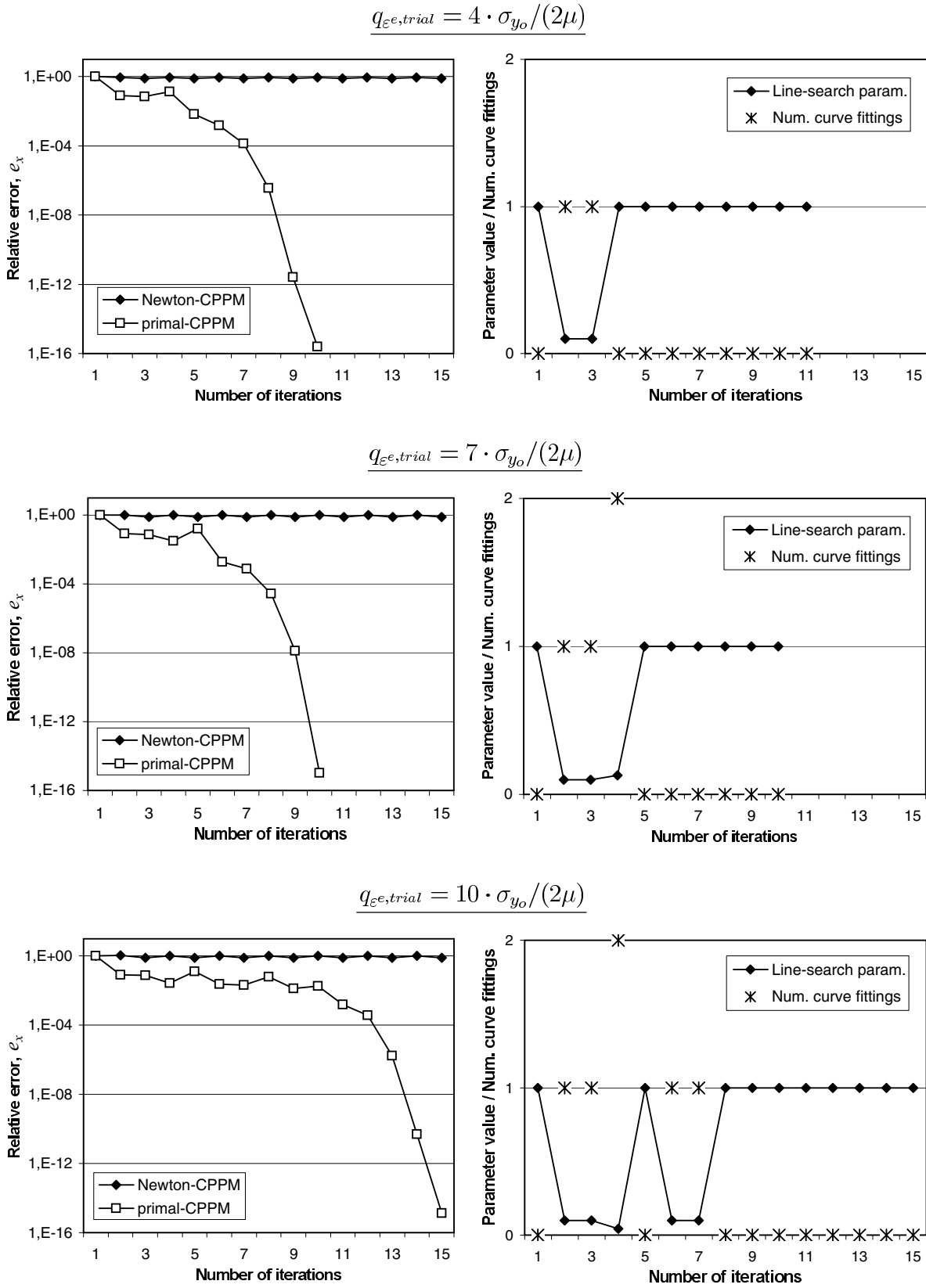


FIGURE 4.4. Single increment tests: deviatoric plastic models ($m = 20$). Convergence results and evolution of the line search scheme with the primal-CPPM for elastic trial states at $\theta_{\varepsilon^e, trial} = 15^\circ$ and $q_{\varepsilon^e, trial} = 4, 7, 10 \cdot \sigma_{y_0} / (2\mu)$.

TABLE 4.1. Single increment tests: deviatoric plastic models ($m = 20$). Accuracy of the results obtained with the primal-CPPM for the plastic correction problems of Figures 4.3 and 4.4, with respect to the reference solutions computed with 1000 time increments.

$q_{\varepsilon^e, trial} \cdot 2\mu / \sigma_{y_0}$	Method	Approx. $\theta_{\varepsilon_{n+1}^e}$	$\theta_{\varepsilon_{n+1}^e}$ error	$q_{\varepsilon_{n+1}^e}$ error
1.5	Newton-CPPM	6.4°	0.14°	0.11%
2.2	Newton-CPPM	2.7°	1.41°	0.83%
4	primal-CPPM	1.8°	0.51°	0.25%
7	primal-CPPM	1.5°	0.25°	0.11%
10	primal-CPPM	1.4°	0.16°	0.07%

also quadratic. The Newton-CPPM does not converge. The maximum number of curve fittings per iteration is very low in all cases (a maximum of two) and the active constraint condition, equation (2.3), has not been activated in any case. In this way, the computational cost per iteration of the primal-CPPM is equivalent to that of the Newton-CPPM, with the added improved convergence properties.

The accuracy observed in the tests of Figures 4.3 and 4.4 in the value of the computed final elastic strain ε_{n+1}^e is compiled in Table 4.1. The same elastic trial states have been imposed, with the final solution obtained with 1000 sub-steps. The corresponding plastic corrections have not activated the line search scheme with such small increments. The final value of the Lode angle is very close to 0°, where the curvature of the yield surface is higher, in all the cases. The results obtained with a single increment for $q_{\varepsilon^e, trial} = 4, 7$ and $10 \cdot \sigma_{y_0} / (2\mu)$ (where the line search is needed for convergence) show the same degree of accuracy as the results for $q_{\varepsilon^e, trial} = 1.5$ and $2.2 \cdot \sigma_{y_0} / (2\mu)$ (solved without the need of a line search scheme). Therefore, the use of large trial increments does not imply a loss of accuracy in this case. Hence, the use of the primal-CPPM becomes a clearly competitive option.

To conclude this section, Figure 4.5 depicts the results obtained with augmented Lagrangian versions of the Newton-CPPM and the primal-CPPM. The same range of the trial state values of Figure 4.2 is considered. The performance of both algorithms is observed to improve with the penalty parameter c within a certain range. The size of the region of no convergence of the original Newton-CPPM decreases as the value of c increases, for small values of c ($\leq 1/\sigma_{y_0}$, approximately). However, this tendency reverses for larger values of c . The same behavior is detected with the primal-CPPM, the so-called augmented-primal-CPPM. A slight reduction in the number of iterations is found with

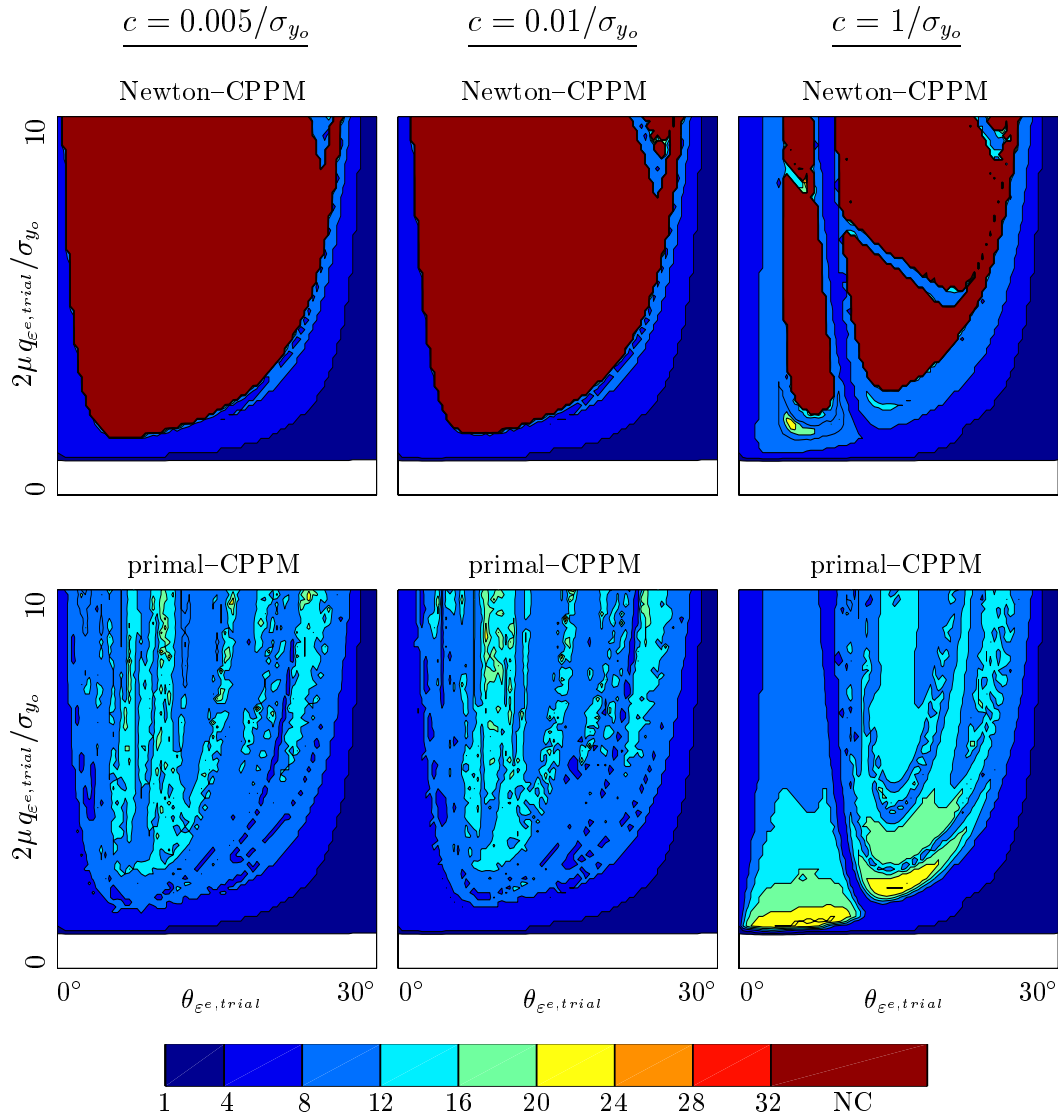


FIGURE 4.5. Single increment tests: deviatoric plastic models ($m = 20$). Number of iterations needed for convergence by the Newton-CPPM and the augmented-primal-CPPM for different values of the penalty parameter c , and large excursions outside the elastic domain.

small values of c ($\leq 0.1/\sigma_{y_o}$, approximately), but for large values of c the overall behavior does not improve, or may even worsen on, the non-augmented formulation.

4.1.2. Pressure-dependent plastic models

We consider in this section the primal-CPPM applied to several examples involving the rounded hyperbolic Mohr-Coulomb yield surface described in Section II.2 in Appendix II. The main goal in presented this additional case is to evaluate the properties of the algorithm in situations involving a non-differentiable flow vector. This yield surface is

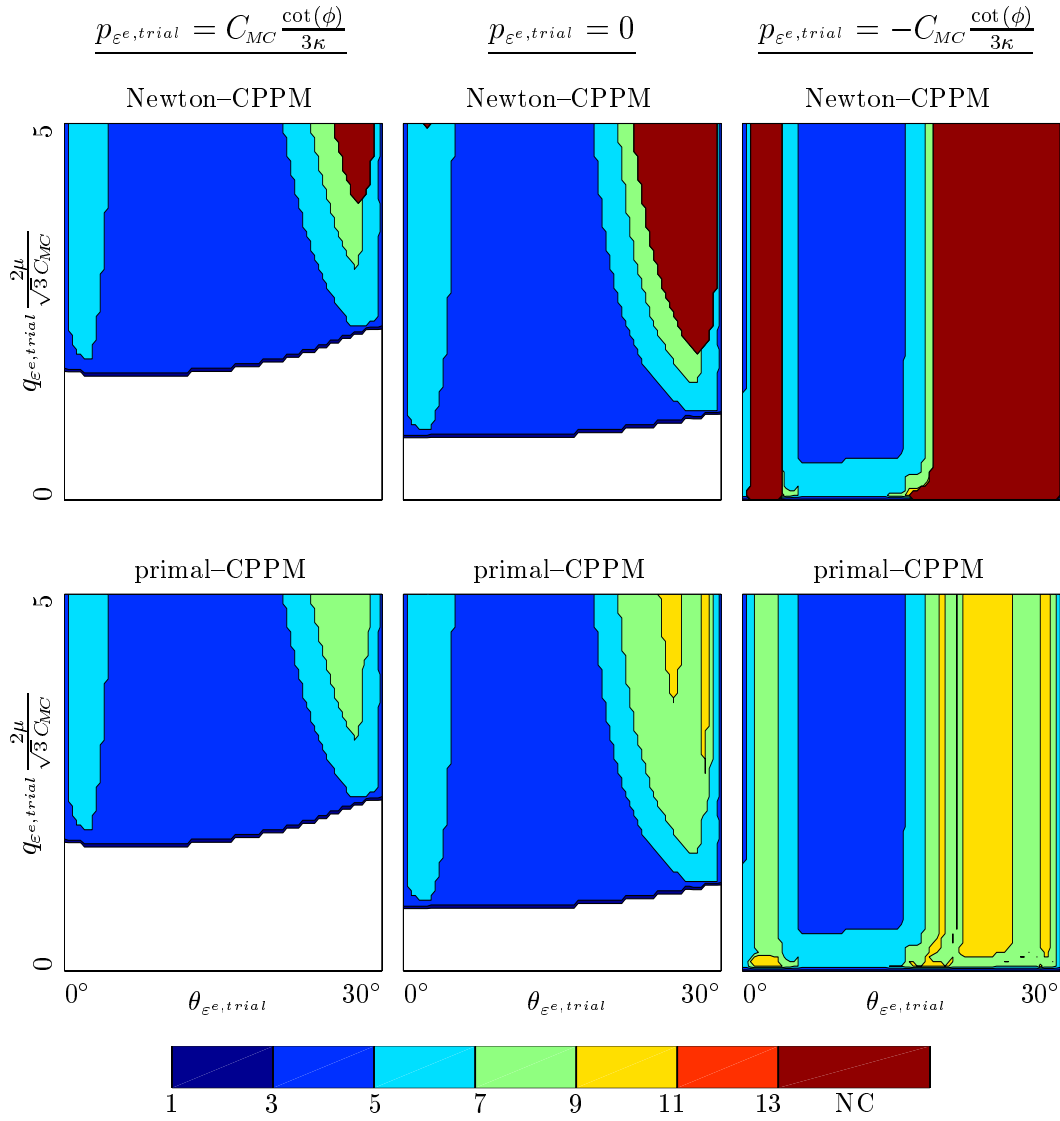


FIGURE 4.6. Single increment tests: pressure-dependent plastic models. Number of iterations needed for convergence by the Newton-CPPM and the primal-CPPM for $p_{\epsilon^{e,trial}} = 1, 0, -1 \cdot C_{MC} \cot(\phi)/(3\kappa)$.

considered in combination with Hencky's law for a bulk modulus of $\kappa = 2500 \text{ kN/mm}^2$ and a shear modulus of $\mu = 1153.8461 \text{ kN/mm}^2$, and perfect plasticity. The values of $C_{MC} = 1 \text{ kN/mm}^2$ and $\phi = 30^\circ$ are considered for the cohesion and the friction angle, respectively (PÉREZ-FOGUET ET AL. [2000a,b]).

Figure 4.6 compares the number of iterations needed for convergence by the Newton-CPPM and the primal-CPPM. The solutions for imposed elastic trial states located in deviatoric planes at $p_{\epsilon^{e,trial}} = 1, 0$ and $-1 \cdot C_{MC} \cot(\phi)/(3\phi)$ are shown, for the cohesive and frictional parameters C_{MC} and ϕ , respectively. The value $p_{\epsilon^{e,trial}} = -C_{MC} \cot(\phi)/(3\kappa)$

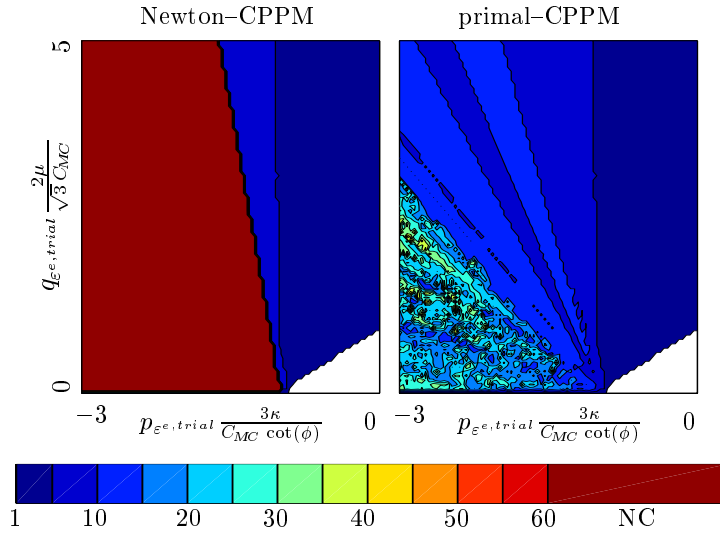


FIGURE 4.7. Single increment tests: pressure-dependent plastic models. Number of iterations needed for convergence by the Newton-CPPM and the primal-CPPM for $\theta_{\epsilon^e, trial} = 30^\circ$.

corresponds to the deviatoric plane passing through the vertex of the underlying Mohr–Coulomb cone. The trial states are then defined by the radial measure $q_{\epsilon^e, trial} \in [0, 5 \cdot \sqrt{3}C_{MC}/(2\mu)]$ and the Lode angle $\theta_{\epsilon^e, trial} \in [0^\circ, 60^\circ]$.

We observe that no convergence is detected by the standard Newton-CPPM when the solution is close to the Lode angles $\theta_{\epsilon^e, trial} = 5^\circ$ and 55° . The region of no convergence around $\theta_{\epsilon^e, trial} = 55^\circ$ is due to the non-differentiability of the flow vector and the high curvature of the yield surface. The region around $\theta_{\epsilon^e, trial} = 5^\circ$ is related only with the non-differentiability of the flow vector. In both cases this region of no convergence decreases as the solution is further away from the apex. In contrast, we observe that the use of the new primal-CPPM avoids the regions of no convergence entirely. Convergence is attained in less than 10 iterations for all trial states, with a maximum of two curve fittings per iteration and without the activation of the constraint condition (2.3). We note that convergence is obtained always with a reduced number of iterations in both methods at the trial Lode angles of 0° and 60° exactly. This particular situation happens because the Lode angle of the final solutions coincide with those of the trial states for these particular tests. By symmetry, the gradient of the yield surface does not have a component in the Lode angle direction.

The number of iterations for elastic trial steps in the meridian plane $\theta_{\epsilon^e, trial} = 30^\circ$ are shown in Figure 4.7. The Newton-CPPM does not converge in a large region of the trial state located behind the apex, that is, for $p_{\epsilon^e, trial} < -C_{MC} \cot(\phi)/(3\kappa)$. This is due to the non-differentiability of the flow vector and the high curvature of the yield surface in all the apex region. The standard Newton-CPPM becomes then useless to solve problems

which involve tensile pressures with this yield surface.

In contrast, the primal–CPPM leads to convergence for all the trial states. Still, the overall behavior of the primal–CPPM in the region behind the apex is worse than in the examples of Figure 4.6. There is a high variability in the distribution of the number of iterations, which for some trial states are a relatively large, although less than 50 iterations are needed anywhere. The large number of iterations is again related with to the non-differentiability of the flow vector, with the associated lack of continuity of the Jacobian at $\theta_\sigma = 5^\circ$ and $\theta_\sigma = 55^\circ$. The high high sensitivity in the initial trial state can be traced back to the closeness of the iterative process to these points for low values of q_σ . The results of Figure 4.7 has been obtained with a maximum number of curve fittings fixed to three. For some trial states, this parameter influences in the convergence results, although the overall behaviour is the same

To illustrate better the effect of the non-differentiability of the residual vector and the observed dependence on different algorithmic parameters in the resulting highly sensitive cases, we consider the specific trial state defined by $p_{\varepsilon e, trial} = -3 \cdot C_{MC} \cot(\phi)/(3\kappa)$, $q_{\varepsilon e, trial} = 2.25 \cdot \sqrt{3}C_{MC}/(2\mu)$ and $\theta_{\varepsilon e, trial} = 30^\circ$ in this region of high variability. The primal–CPPM takes 49 iterations with a maximum of three curve fittings ($j_{max} = 3$), as shown in Figure 4.7. This is the maximum number of iterations observed in this figure. The evolution of the relative error, the yield function, the number of curve fittings, the value of the line search parameter and the Lode angle of the stresses during the iterative process is depicted in Figure 4.8 for a maximum number of curve fittings $j_{max} = 5$, and 10. In both cases, more curve fittings than this fixed maximum number are needed in a few iterations. These iterations are indicated with a black circle in the plots depicting the required number of curve fittings. Note that both iterative processes (for $j_{max} = 5$ and 10) coincide until this point. During these early stages of the iterative process, the iterations are “captured” at the Lode angle $\theta_\sigma = 55^\circ$, where the Jacobian of the residual is not continuous. The number of curve fittings increases and the iterative increment becomes very small (bounded from below by the backtracking parameter $\eta = 0.1$ and maximum number of curve fittings; see Box I.1) while the relative value of the yield function remains basically constant and the relative error based on the norm of the increment of the unknowns diminishes. This fact is directly related with the value of the line search parameter.

The test with $j_{max} = 10$ allows the additional number of curve fittings after this point. After the maximum number of curve fittings j_{max} is reached, the behavior of the iterative scheme changes dramatically. One curve fitting is needed during some of the subsequent iterations and finally a quadratic rate of convergence is achieved. The iterative process has “escaped” from the discontinuity of the Jacobian. These considerations, together with the discussion presented with Figure 4.2 for smooth cases, allow to conclude that a moderate value of the parameter j_{max} ($\approx 3 - 5$ seems appropriate) should be used for the maximum number of curve fittings.

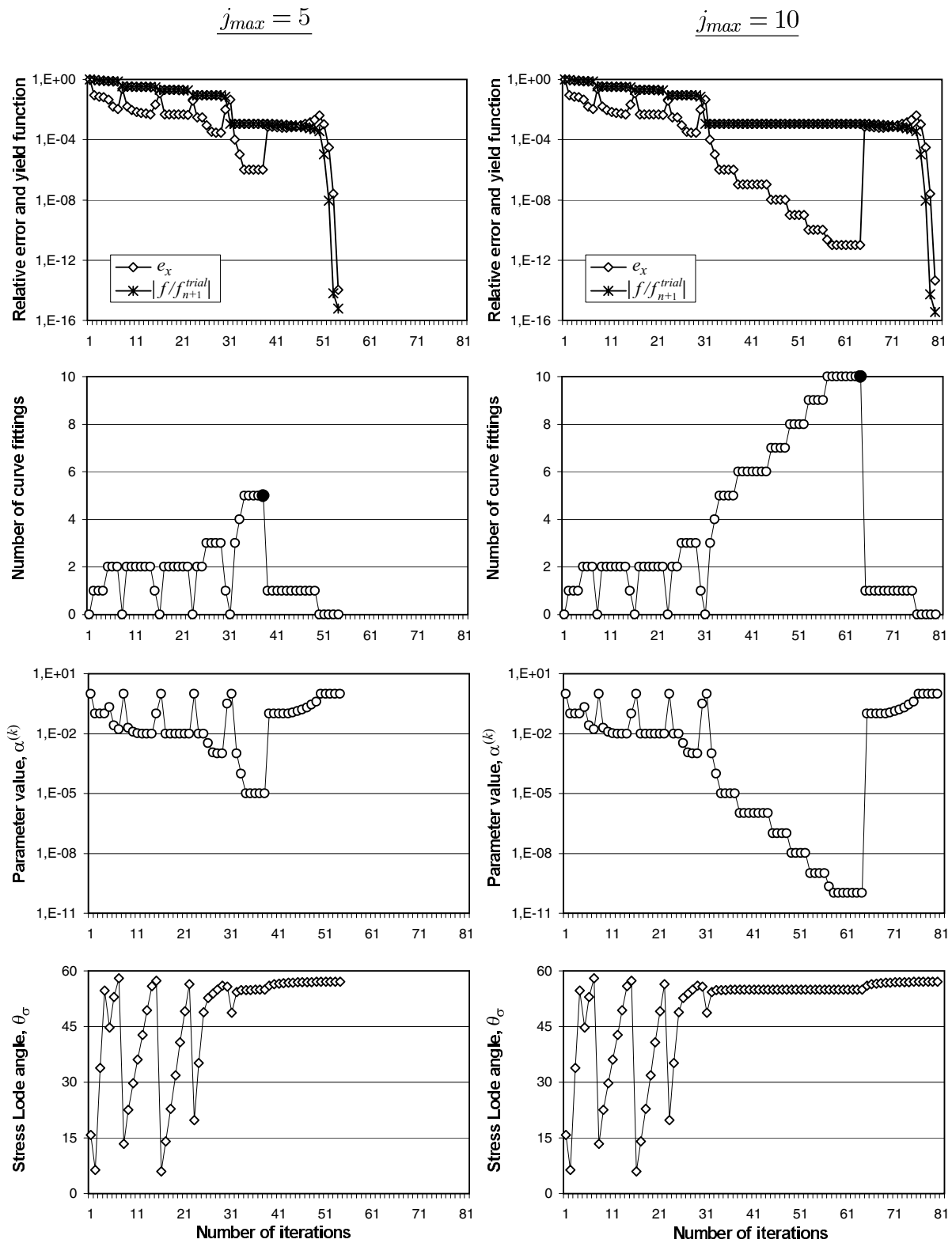


FIGURE 4.8. Single increment tests: pressure-dependent plastic models. Influence of the non-differentiability of the flow vector in the RHMC model for the test given by $p_{\varepsilon,trial} = -3 \cdot C_{MC} \cot(\phi)/(3\kappa)$, $q_{\varepsilon,trial} = 2.25 \cdot \sqrt{3}C_{MC}/(2\mu)$ and $\theta_{\varepsilon,trial} = 30^\circ$. Evolution of the relative error $e_x^{(k)}$, the yield function $f^{(k)}/f_{n+1}^{trial}$, the number of curve fittings, the line search parameter $\alpha^{(k)}$ and the stress Lode angle $\theta_\sigma^{(k)}$ for a maximum of curve fittings $j_{max} = 5$ and 10.

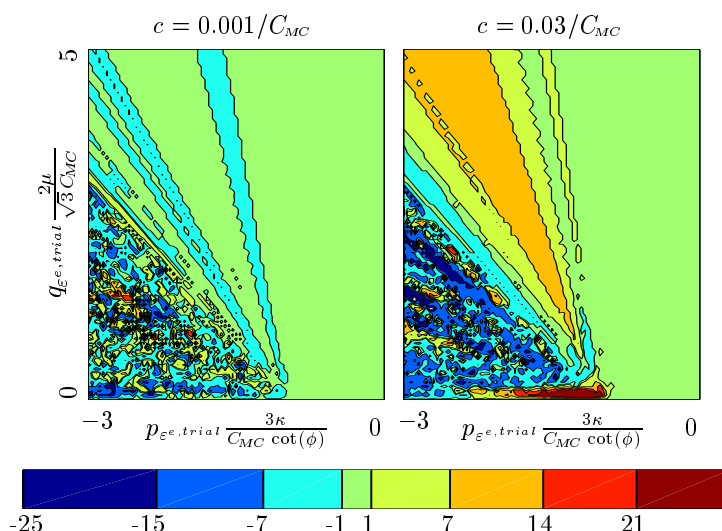


FIGURE 4.9. Single increment tests: pressure-dependent plastic models. Increment of the number of iterations for the primal-CPPM with different values of the penalty parameter c , with respect to the non-augmented formulation in Figure 4.7 for $\theta_{\epsilon^{e,trial}} = 30^\circ$.

To conclude this section, we consider again the augmented versions of the algorithms. The increment of the number of iterations of the augmented primal-CPPM with respect to the non-augmented version is depicted in Figure 4.9 (elastic trial steps in the meridian plane $\theta_{\epsilon^{e,trial}} = 30^\circ$). The performance of the scheme improves in average with small values of the penalty parameter c when compared with the non-augmented formulation. For larger values of c , although a high reduction of the number of iterations is found in some regions, a significant increase is found in another ones (note the results obtained with $c = 0.03/C_{MC}$ in the region close to the apex). This effect is accentuated as c increases, and, as this effect occurs in the region closest to the apex, the method becomes less competitive with large values of c . The effects of the non-differentiability of the residual follow the same pattern in this augmented case as discussed in the previous paragraphs for the dual-CPPM.

4.2. Imposed deformation gradient path

We evaluate next the performance of the primal algorithms in more general situations involving Ogden hyperelastic models (i.e., non-constant elasticities in the logarithmic strains) as well as strain hardening and softening relations. To this purpose we consider imposed paths of the deformation gradient. More specifically we consider the deformation gradient history

$$\mathbf{F}(t) = b(t)^{1/3} \text{diag}(a(t), a(t)^{-r}, a(t)^{r-1}) \quad (4.4)$$

for the pseudotime t , function $a(t)$ (such as $a(0) = 1$ and $a(t) > 0$) that guides the evolution

TABLE 4.2. Elastic parameters used with the Ogden hyperelastic model.

$\kappa = 164.206 \text{ kN/mm}^2$	$\hat{\mu}_1 = 1.4911$	$\hat{\alpha}_1 = 1.3000$
$\mu_g = 80.1938 \text{ kN/mm}^2$	$\hat{\mu}_2 = 0.0028$	$\hat{\alpha}_2 = 5.0000$
$N = 3$	$\hat{\mu}_3 = -0.0237$	$\hat{\alpha}_3 = -2.0000$

of the axial stretch in the first principal direction, and the function $b(t)$ controlling the volumetric response ($\det \mathbf{F} = b(t)$). The exponent r in (4.4) controls the desired Lode angle of the elastic trial increment ($\Delta \boldsymbol{\varepsilon}^{e,trial} = \boldsymbol{\varepsilon}_{n+1}^{e,trial} - \boldsymbol{\varepsilon}_n$), since

$$r = \frac{1}{2} \left(1 - \sqrt{3} \tan(\theta_{\Delta \boldsymbol{\varepsilon}^{e,trial}}) \right) \quad (4.5)$$

In particular, the value $r = 0.5$ corresponds to pure tension ($\theta_{\Delta \boldsymbol{\varepsilon}^{e,trial}} = 0^\circ$) and the value $r = -1$ to pure compression ($\theta_{\Delta \boldsymbol{\varepsilon}^{e,trial}} = 60^\circ$).

4.2.1. Deviatoric plastic models

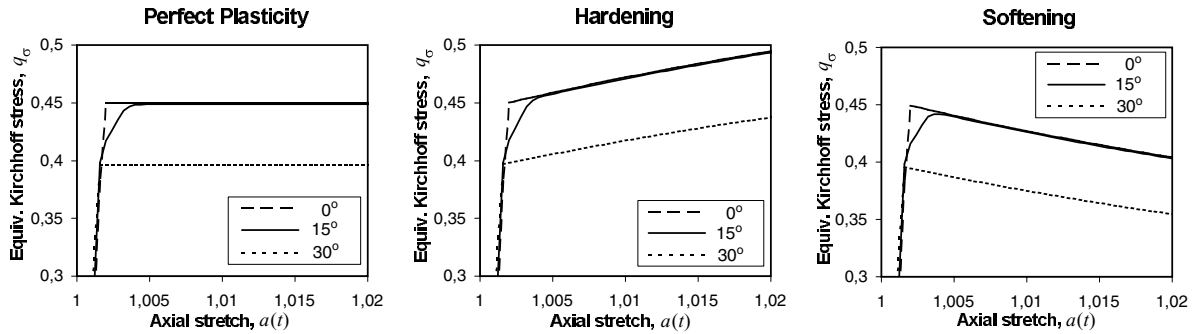
We consider the deviatoric plastic models defined by the von Mises-Tresca type yield surfaces described in Section II.2 of Appendix II. The Ogden hyperelastic model defined in (II.4) of Appendix II, with material parameters summarized in Table 4.2 (MIEHE [1998]), is considered. Similarly, the hardening/softening potential (II.9) is considered for the saturation exponent $\delta = 20$ and with the saturation stress $\sigma_{y_\infty} = 0.6 \text{ kN/mm}^2$ for the examples with strain hardening and $\sigma_{y_\infty} = 0.3 \text{ kN/mm}^2$ in the examples with strain softening. In all cases, including the examples with perfect plasticity, the initial yield stress is $\sigma_{y_0} = 0.45 \text{ kN/mm}^2$.

The imposed function of

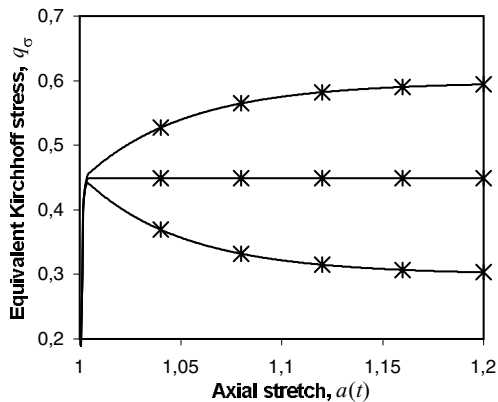
$$a(t) = 1 + 0.2 t \quad \text{for } t \in [0, 1], \quad (4.6)$$

is considered, with $b(t) \equiv 1$ leading to a purely isochoric deformation. We consider solutions involving 5, 50 and 500 equal time increments. The resulting Kirchhoff stress path in q_σ is depicted in Figures 4.10, including details in the small range of the imposed axial stretch. We consider the values of $\theta_{\Delta \boldsymbol{\varepsilon}^{e,trial}} = 0^\circ, 15^\circ$ and 30° , leading to the corresponding exponents r by (4.5). Note the smooth transition from elastic to elastoplastic regime in the curves corresponding to $\theta_{\Delta \boldsymbol{\varepsilon}^{e,trial}} = 15^\circ$. This is produced by the change of the Lode's angle of the stresses during the evolution of the simulation. The evolution of q_σ for a larger range of the axial stretch and $\theta_{\Delta \boldsymbol{\varepsilon}^{e,trial}} = 15^\circ$ is shown in Figure 4.10.b. The evolution of the Lode angle θ_σ of the Kirchhoff stress is depicted in Figure 4.10.c for the softening case. The solid curves of correspond to the problems solved with 500 equal increments and the

a)



b)



c)

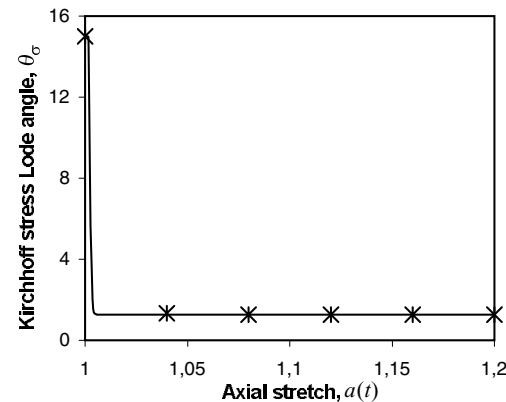


FIGURE 4.10. Imposed deformation gradient paths: deviatoric plastic models ($m = 20$). **a)** Details of the evolution of the equivalent Kirchhoff stresses q_σ in the range $a(t) \in [1, 1.02]$, for three prescribed paths ($\theta_{\Delta \varepsilon^e, trial} = 0^\circ, 15^\circ$ and 30°) and perfect plasticity, hardening and softening. **b)** Evolution of q_σ in the full range $a(t) \in [1, 1.2]$ for perfect plasticity, hardening and softening models, and $\theta_{\Delta \varepsilon^e, trial} = 15^\circ$. (solid lines for obtained with 500 time increments, with the stars corresponding to the solution obtained with 5 time increments, both obtained with the primal-CPPM). **c)** Evolution of the Lode angle θ_σ for the softening case and $\theta_{\Delta \varepsilon^e, trial} = 15^\circ$.

stars to the problems solved with just 5 equal increments. The line search scheme has not been activated in the problem with 500 increments recovering then the Newton-CPPM. It has been activated with the simulation involving 5 time increments only. Still, we observe in Figure 4.10.b a good agreement between both solutions, hence implying that the use of very large elastic trial steps does not imply a loss of accuracy.

The convergence results at several pseudotimes t are presented in Figure 4.11 for the hardening and the softening examples, including the evolution of the relative errors $e_x^{(k)}$ (see equation (4.3)) in $\mathbf{x} = \{\varepsilon_{n+1}^e, -\alpha_{n+1}, \Delta\gamma\}$. The results correspond to the paths solved

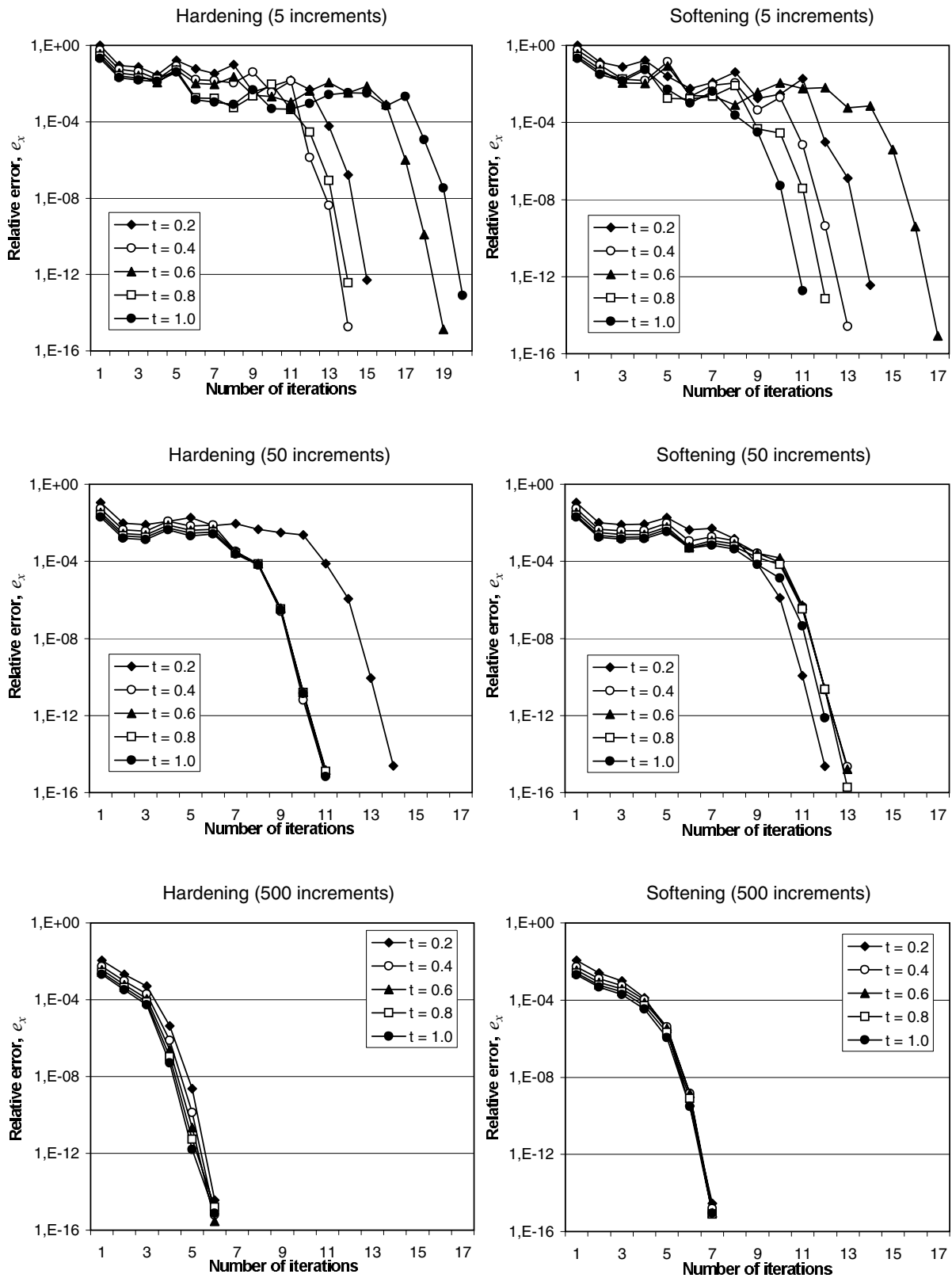


FIGURE 4.11. Imposed deformation gradient paths: deviatoric plastic models ($m = 20$). Convergence results with the primal-CPPM for several pseudotimes t (hardening and softening, and 5, 50 and 500 increments).

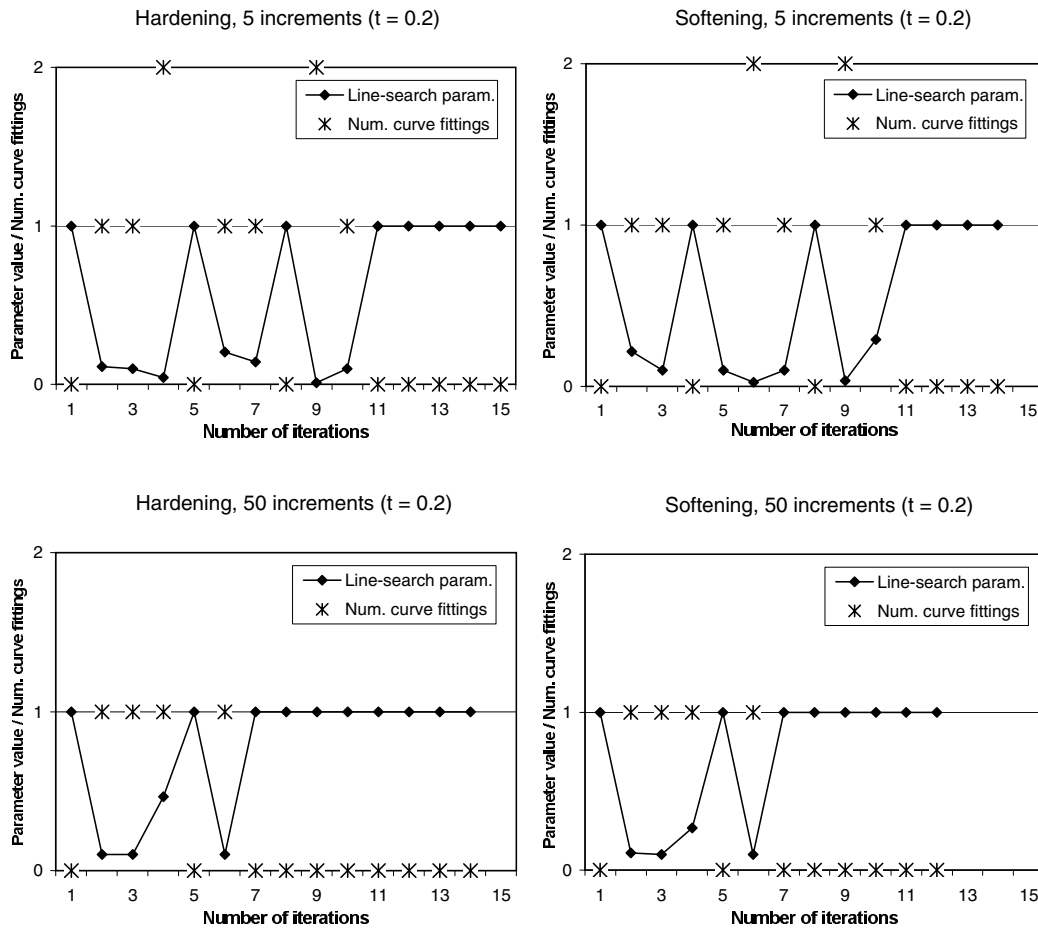


FIGURE 4.12. Imposed deformation gradient paths: deviatoric plastic models ($m = 20$). Evolution of the line search at $t = 0.2$ for the examples with hardening and softening, and 5 and 50 time increments.

with 5, 50 and 500 time increments. In all cases the primal-CPPM converges with the rate of convergence being asymptotically quadratic for each time increment. The evolution of the line search parameter and the number of curve fittings is shown in Figure 4.12, for the runs with 5 and 50 increments, pseudotime $t = 0.2$, and both the hardening and softening problem. As occurred in the examples of Section 4.1, the maximum number of curve fittings is two. Therefore, the computational cost added in each iteration by the considered line search scheme is not significant.

We can observe that, although the number of iterations per increment increases as the number of increments reduces, the ratio is clearly favorable to the problems with less time increments. A reduction of the number of increments by a factor 10 implies a reduction of the number of accumulated iterations by a factor of 5, at the least. This reduction is directly related with a reduction of the total computational cost. Therefore, the primal-CPPM is computationally very efficient, including cases with non-constant elasticities.

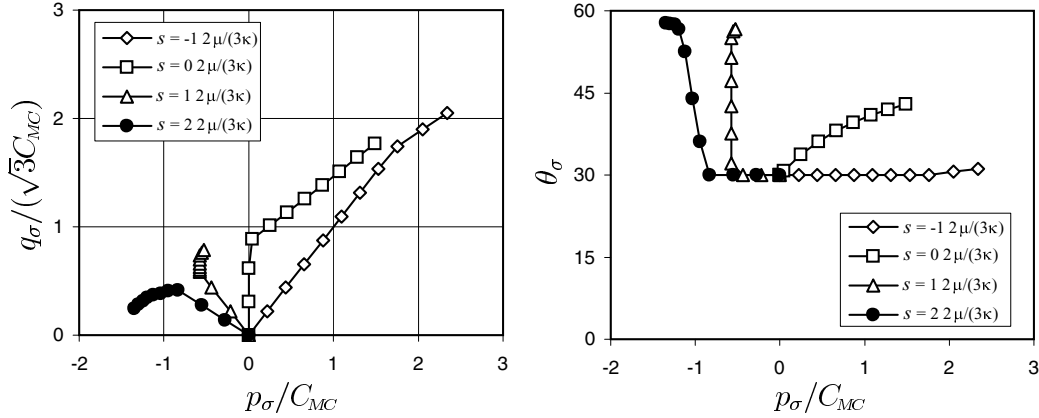


FIGURE 4.13. Imposed deformation gradient paths: pressure-dependent plastic models. Evolution of the Kirchhoff stresses in the meridian and the deviatoric planes for the paths defined by $r = 0$ and $s = -1, 0, 1, 2 \cdot 2\mu/(3\kappa)$ (with $t_f = 1.58, 2.24, 1.58$ and 1 , respectively), obtained by the primal-CPPM with 10 time increments

4.2.2. Pressure-dependent models

We conclude the evaluation of the primal algorithms with the consideration of the rounded hyperbolic Mohr-Coulomb model for imposed path of the deformation gradient. We consider again the path defined by the relation (4.4), with the stretch function

$$a(t) = 1 + 6 \cdot 10^{-5} t \quad t \in [0, t_f], \quad (4.7)$$

for a final time t_f (see below) and with the volumetric function

$$b(t) = (a(t))^{3s}, \quad (4.8)$$

allowing to prescribe the parameter

$$p_{\Delta\varepsilon^{e,trial}} = \frac{-s}{\sqrt{r^2 - r + 1}} \frac{q_{\Delta\varepsilon^{e,trial}}}{\sqrt{3}}, \quad (4.9)$$

for the elastic trial strain increment $\Delta\varepsilon^{e,trial}$ in the meridian plane. Hencky's law is considered in this case which results in a linear relation between the stresses and logarithmic strains. Equation (4.9) is equivalent in this case to

$$s = - \sqrt{r^2 - r + 1} \frac{2\mu}{3\kappa} \frac{p_{\Delta\sigma_{n+1}^{trial}}}{q_{\Delta\sigma_{n+1}^{trial}}/\sqrt{3}}. \quad (4.10)$$

where $\Delta\sigma_{n+1}^{trial} = \sigma_{n+1}^{trial} - \sigma_n$. The evolution of the Kirchhoff stresses is depicted in Figure 4.13 for the paths defined by $r = 0$ and $s = -1, 0, 1, 2 \cdot 2\mu/(3\kappa)$ (with $t_f = 1.58, 2.24$,

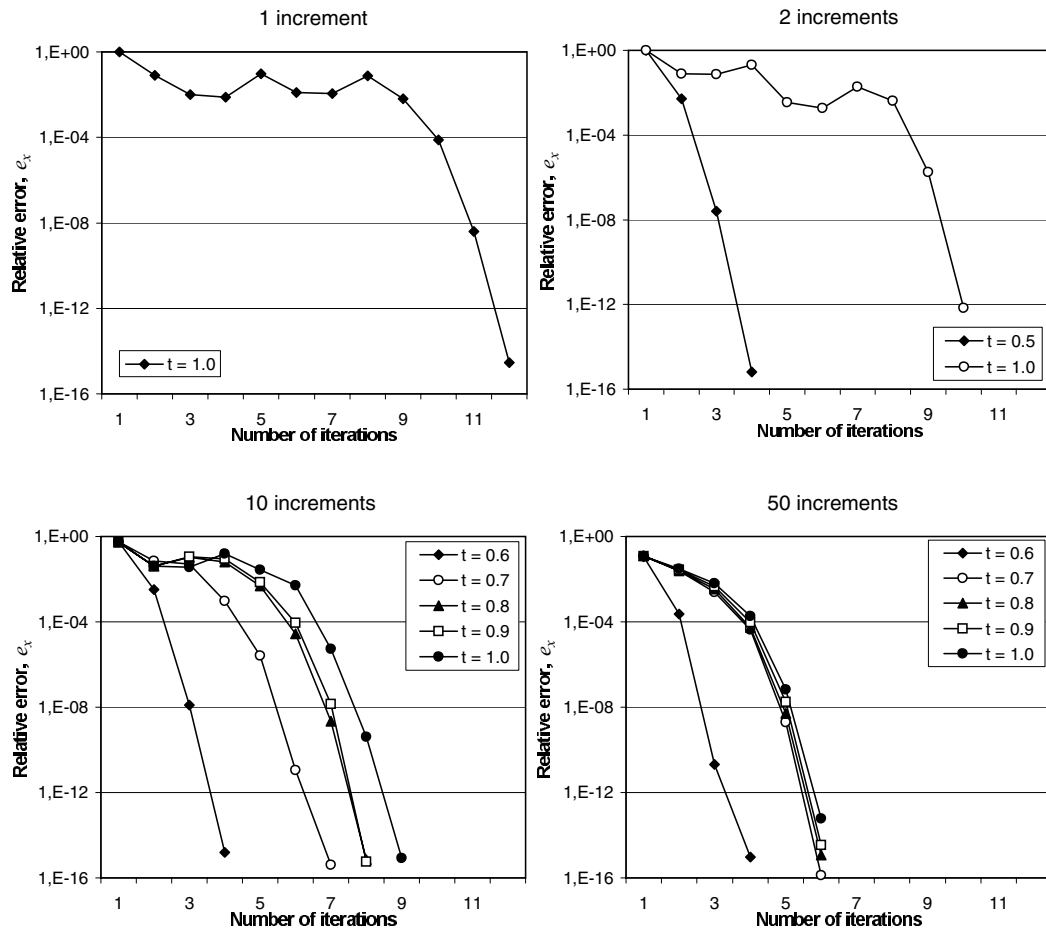


FIGURE 4.14. Imposed deformation gradient paths: pressure-dependent plastic models. Convergence results for several pseudotimes t of the path $s = 2 \cdot 2\mu/(3\kappa)$ ($t_f = 1$) obtained with the primal-CPPM and 1, 2, 10 and 50 increments.

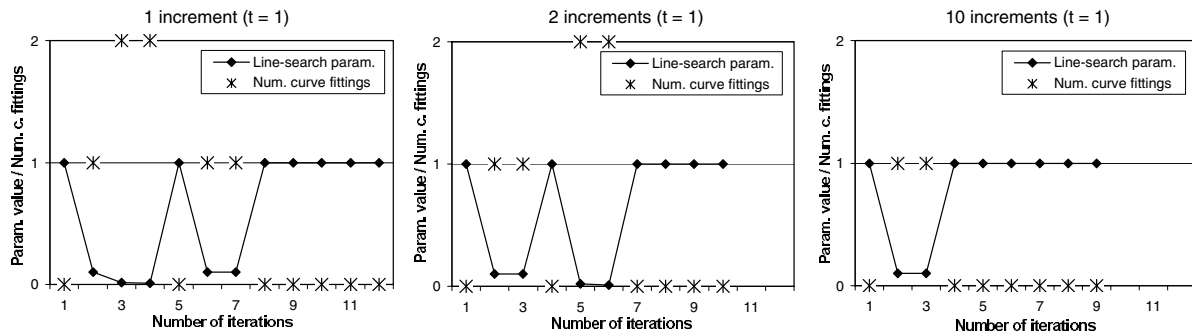


FIGURE 4.15. Imposed deformation gradient paths: pressure-dependent plastic models. Evolution of the line search parameter at each last increment of the path $s = 2 \cdot 2\mu/(3\kappa)$ ($t = t_f = 1$) obtained with the primal-CPPM and 1, 2 and 10 increments.

TABLE 4.3. Imposed deformation gradient paths: pressure-dependent plastic models. Accuracy of the final results obtained with the primal-CPPM for the four paths presented in Figure 4.14 with respect to the reference solution computed with 1000 increments.

Number incr.	Method	Approx. $\theta_{\varepsilon_{n+1}^e}$	$\theta_{\varepsilon_{n+1}^e}$ error	$q_{\varepsilon_{n+1}^e}$ error	$p_{\varepsilon_{n+1}^e}$ error
50	Newton-CPPM	57.7°	0°	0.04%	0.01%
10	primal-CPPM	57.7°	0.005°	0.23%	0.06%
2	primal-CPPM	57.0°	0.7°	0.87%	0.40%
1	primal-CPPM	56.5°	1.2°	1.14%	0.61%

1.58 and 1, respectively). The stress paths in the meridian and the deviatoric planes are shown.

The path defined by $r = 0$ and $s = 2 \cdot 2\mu/(3\kappa)$ has been obtained with the primal-CPPM and with 1, 2, 10 and 50 equal time increments. The convergence results for several pseudotimes t are shown in Figure 4.14. Except for the solution obtained with 50 time increments, the line search scheme has been activated in these solutions. The characteristic asymptotic quadratic rate of convergence is observed in all the cases. The values of the line search parameter, α_k , and the number of quadratic curve fittings has been depicted in Figure 4.15 for the last time increment ($t = 1$) of the paths solved with 1, 2 and 10 increments. In all the cases the maximum number of curve fittings is two, and the active constraint condition, equation (2.3), has not been activated. Therefore, the cost per iteration of the primal-CPPM is of the same order than that of Newton-CPPM. In fact, the number of accumulated iterations decreases with the number of increments, hence resulting in a reduced computational cost with the use of the primal-CPPM.

The accuracy of the computed final solution is assessed in Table 4.3. The same final deformation gradient has been imposed with 1000 increments, with the final result taken as a reference. Although the results are less accurate as less increments are done, the errors are low (of the same order as the results of Table 4.1) even for only one increment, thus justifying the use of very large trial increments in combination of the primal-CPPM.

5. Numerical Assessment: Dual Algorithms

We evaluate in this section the numerical properties of the new dual closest-point projection algorithms presented in Section 3. More specifically, it is our goal to verify their globally convergent character, showing locally an asymptotic quadratic rate of convergence, and to evaluate the computational cost given their two-level structure. For brevity in the

presentation, we only consider the single increment tests presented in Section 4.1 for the new primal algorithms developed in this work. We present again examples in the context of deviatoric and pressure-dependent plastic models.

5.1. Single increment tests

The single increment tests considered in Section 4.1 are again considered in this section. A trial state, characterized by the deviatoric measures of the Lode angle $\theta_{\varepsilon e, trial}$ and radial measure $q_{\varepsilon e, trial}$, and $p_{\varepsilon e, trial}$ for pressure-dependent models, is imposed and the number of iterations required for convergence measured. We consider the general augmented–dual–CPPM of Boxes 3.3 and 3.4, for a penalty parameter c , recovering essentially the dual–CPPM of Boxes 3.1 and 3.2 for $c = 0$.

5.1.1. Deviatoric plastic models

The deviatoric plastic models described in Section II.2 of Appendix II are considered first, in combination of Hencky’s hyperelastic law and perfect plasticity with the same material parameters as in Section 4.1.1. (i.e. $\kappa = 164.206 \text{ kN/mm}^2$, $\mu = 80.1938 \text{ kN/mm}^2$ and $\sigma_{y_o} = 0.45 \text{ kN/mm}^2$). Figure 5.1 depicts the number of iterations required for convergence by the augmented–dual–CPPM in this case for several elastic trial states and different values of the penalty parameter c . The range of the trial state space depicted is $\theta_{\varepsilon e, trial} = 0^\circ$ to 30° and $q_{\varepsilon e, trial}$ from 0 to $10 \cdot \sigma_{y_o} / (2\mu)$, the same as Figure 4.2. The number of iterations refers to the total number of evaluations of the gradient of the flow vector (which coincides with the sum of the number of iterations of both levels; see Boxes 3.3 and 3.4). Note that this number can be compared directly with the number of iterations with the primal–CPPM since both involve the same major operation count.

We observe that convergence has been achieved for all the trial states and different values of c , for the dual–CPPM ($c = 0$), in particular. The dependence observed on the penalty parameter c agrees with the same performance observed for the augmented–primal–CPPM described in Section 4.1.1. In particular, a significant reduction of the number of iterations, with respect to the non–augmented case $c = 0$, can be observe for low values of the penalty parameter c .

For large values of the penalty parameter c , the scheme requires more iterations in average. This behavior is directly related with the structure of the algorithm. As c increases the upper level problem becomes easier to solve because the function is flatter: for all c the root of the equation (3.8) is in the same position while the value at $\bar{\lambda} = -c/f_{n+1}^{trial}$ is always f_{n+1}^{trial} , with the value at the origin (the initial estimate) decreasing. See Figure 3.1. At the same time, however, the lower level problem becomes more difficult to solve because of the added nonlinearity: compare the last term in the equations (2.1) with the corresponding one in the equations (2.9). The sum of both effects gives an average *optimal* value of c which, for the problems at hand, is approximately given in the range $c \cdot \sigma_{y_o} \in (0.05, 0.5)$.

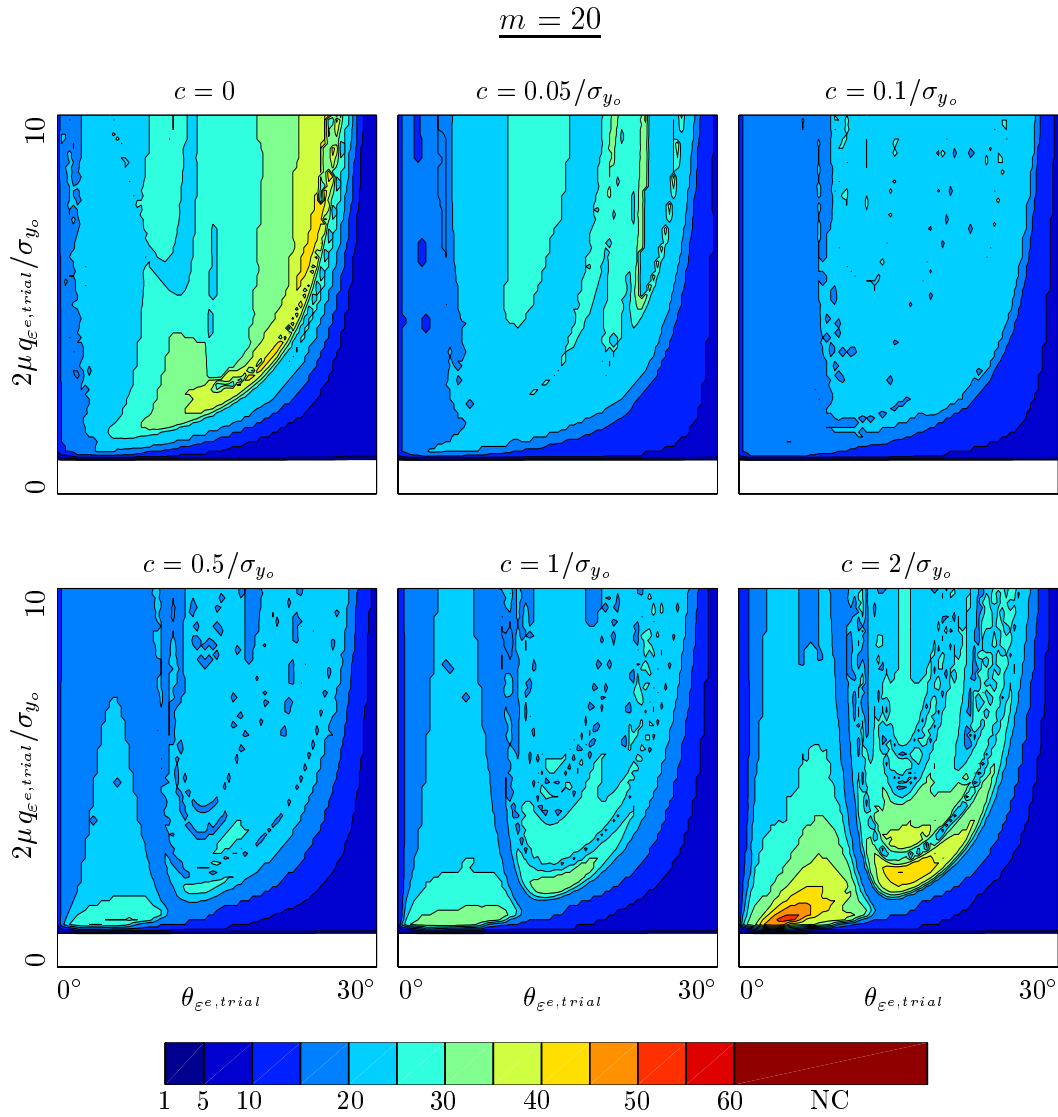


FIGURE 5.1. Single increment tests: deviatoric plastic models ($m = 20$). Number of iterations needed for convergence by the dual-CPPM and the augmented-dual-CPPM for different values of the penalty parameter c .

When comparing these dual algorithms with the primal-CPPM (compare Figure 5.1 with Figures 4.2 and 4.5), we observe that the dual algorithms require, in general, a higher number of iterations to converge. The difference is less important as the number of iterations of the primal-CPPM increases, especially if the line search scheme is activated in this last algorithm. For example, the trial state where the non-augmented primal-CPPM spends the maximum number of iterations, 29, the dual-CPPM ($c = 0.1/\sigma_{y_0}$) needs only 20. However, this improvement is not general for all trial states.

Convergence results of both levels (iterations on $\Delta\gamma^{(k)}$ and $\sigma^{(k)}$) and for three elastic

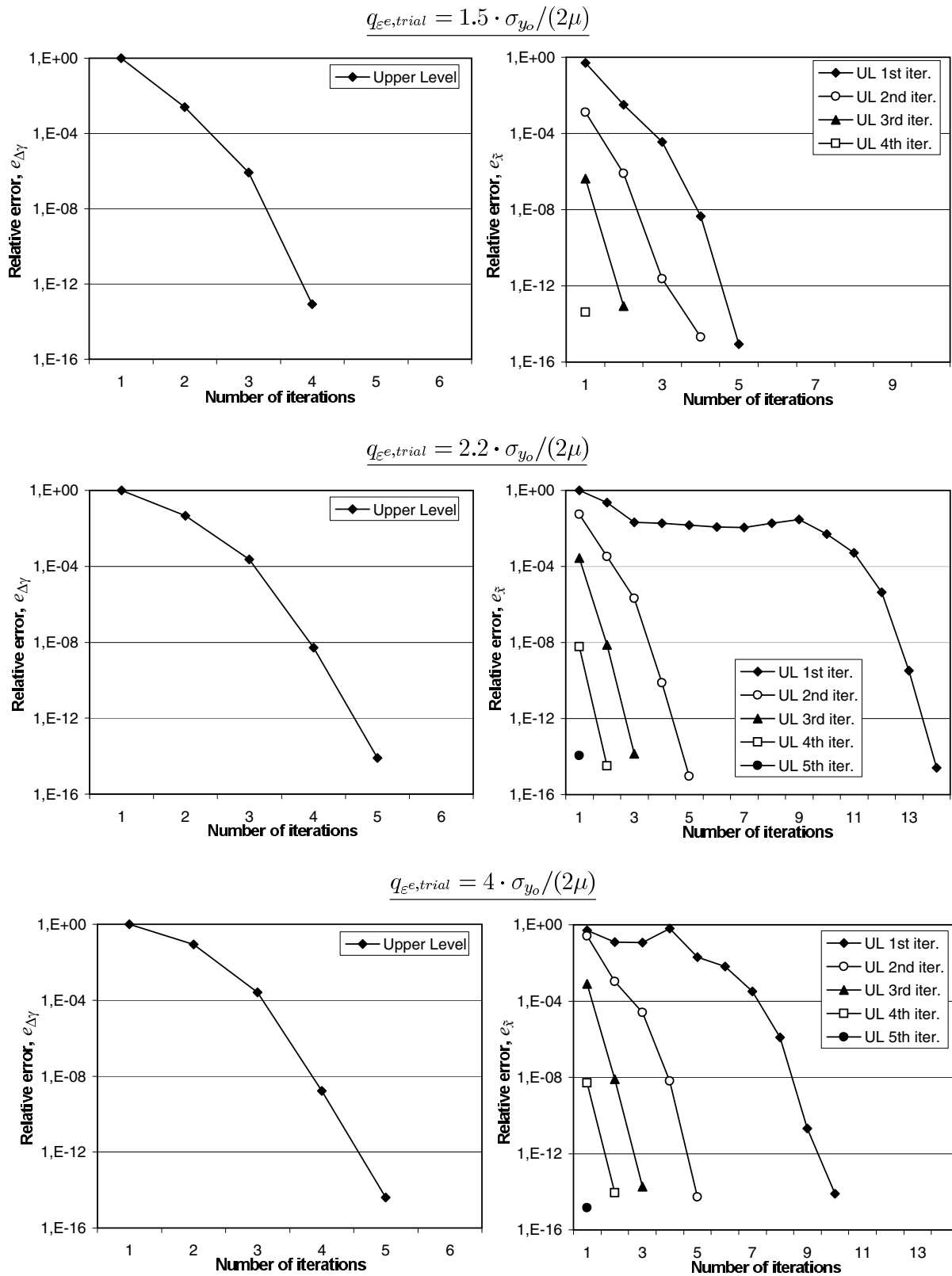


FIGURE 5.2. Single increment tests: deviatoric plastic models ($m = 20$). Convergence results obtained with the dual-CPPM ($c = 0$) for elastic trial states at $\theta_{\varepsilon e, trial} = 15^\circ$ and $q_{\varepsilon e, trial} = 1.5, 2.2, 4 \cdot \sigma_{y_0} / (2\mu)$.

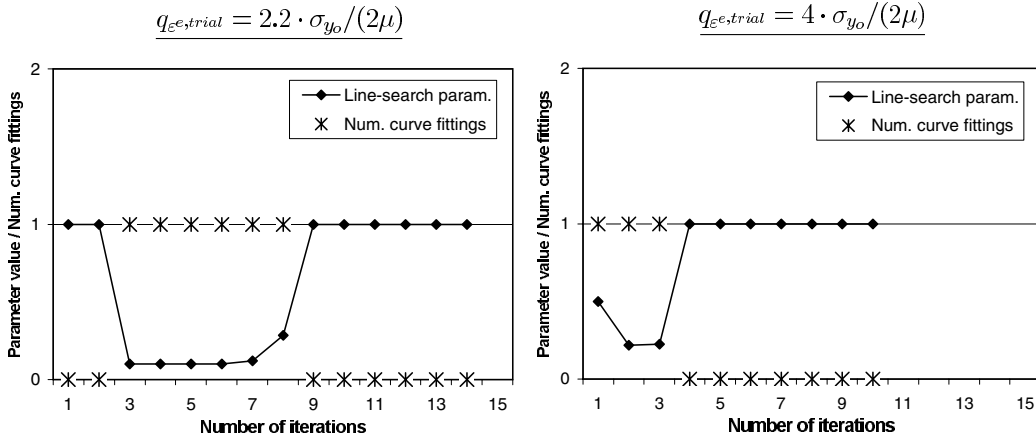


FIGURE 5.3. Single increment tests: deviatoric plastic models ($m = 20$). Evolution of the line search scheme for the first lower level loop of the dual-CPM ($c = 0$). $q_{\epsilon^e, trial} = 2.2, 4 \cdot \sigma_{y_0} / (2\mu)$.

trial states are depicted in Figure 5.2 ($\theta_{\epsilon^e, trial} = 15^\circ$ and $q_{\epsilon^e, trial} = 1.5, 2.2$ and $4 \cdot \sigma_{y_0} / (2\mu)$). The evolutions of the relative errors $e_{\Delta\gamma}$ for the upper level and $e_{\tilde{\mathbf{x}}}$ for the lower level are depicted (particularize equation (4.3) to $\Delta\gamma$ and $\tilde{\mathbf{x}} = \boldsymbol{\epsilon}^{e, (k)}$, respectively). Note that there is a convergence curve for the iterations on $\boldsymbol{\sigma}^{(k)}$ for each iterative value $\Delta\gamma^{(k)}$. All the convergence curves, for both levels, exhibit an asymptotic quadratic rate of convergence. The convergence on $\Delta\gamma$ is achieved in a reduced number of iterations and without activating the line search. The same behavior is observed in the iterations on $\boldsymbol{\sigma}^{(k)}$, except for the first value $\boldsymbol{\sigma}^{(1)}$, and trial states not close to the yield surface ($q_{\epsilon^e, trial} = 2.2$ and $4 \cdot \sigma_{y_0} / (2\mu)$). The line search is required to achieve convergence in these cases.

The evolution of the line search parameter and the number of quadratic curve fittings are depicted in Figure 5.3 for the cases where it has been activated (the first iteration of the lower level, $q_{\epsilon^e, trial} = 2.2, 4 \cdot \sigma_{y_0} / (2\mu)$). Note that just one curve fitting is necessary. However, in some cases (like for $q_{\epsilon^e, trial} = 4 \cdot \sigma_{y_0} / (2\mu)$) the number of activations is quite large. This point is located in the region that requires a larger total number of iterations; see Figure 5.1.

The convergence results for $c = 0.1 / \sigma_{y_0}$ and the same trial states as considered in Figure 5.2 are depicted in Figure 5.4. This value of the penalty parameter c corresponds to the best overall behavior of the numerical scheme; see Figure 5.1. Note that the initial value $\boldsymbol{\sigma}^{(0)}$ employed in the lower level problem, corresponding to the initial value $\Delta\gamma^{(0)} = 0$, is no longer the trial stress for $c > 0$; see Box 3.4. In this way, Figure 5.4 includes convergence curves for the lower level at this iteration zero (initialization) of the upper level. The asymptotic quadratic rate of convergence is verified again. Moreover, the upper level problems converge in just three iterations in all three cases, which agrees with the previous comments about the influence of the penalty parameter on the difficulty of the

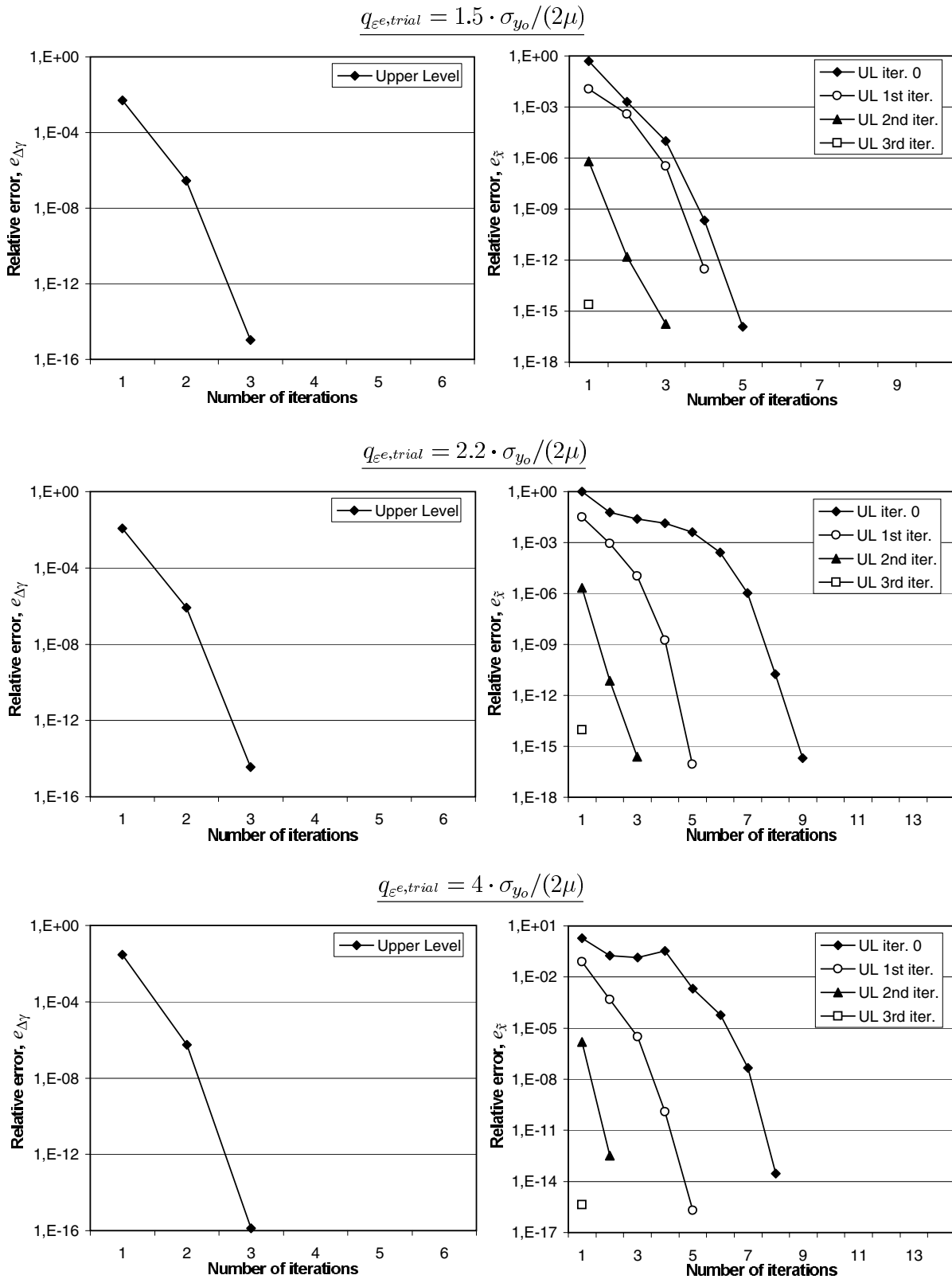


FIGURE 5.4. Single increment tests: deviatoric plastic models ($m = 20$). Convergence results of the augmented-dual-CPM with $c = 0.1/\sigma_{y_0}$ and for elastic trial states at $\theta_{\varepsilon^e, trial} = 15^\circ$ and $q_{\varepsilon^e, trial} = 1.5, 2.2, 4 \cdot \sigma_{y_0} / (2\mu)$.

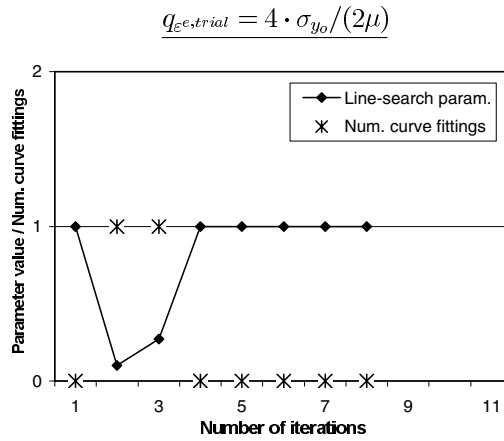


FIGURE 5.5. Single increment tests: deviatoric plastic models ($m = 20$). Evolution of the line search scheme for the first lower level loop of the augmented–dual–CPPM with $c = 0.1/\sigma_{y_0}$. $q_{\varepsilon^e, trial} = 4 \cdot \sigma_{y_0} / (2\mu)$.

problem. The convergence in the lower level problems is also better than for $c = 0$; compare with Figure 5.2. As in the non–augmented case, the first loop of the lower level requires more computational effort, although in this case the number of line search activations is lower. See Figure 5.5, where the evolution of the line search parameter and the number of curve fittings are depicted for the only where it has been activated (first iteration loop of the lower level and $q_{\varepsilon^e, trial} = 4 \cdot \sigma_{y_0} / (2\mu)$).

5.1.2. Pressure-dependent plastic models

We focus in this section in the evaluation of the effects of the non-differentiability of the flow vector in the convergence of the dual algorithms. The RHMC of Appendix II is again considered in combination with perfect plasticity and Hencky’s law, with the same parameters as in Section 4.1.2 (i.e. $\kappa = 2500 \text{ kN/mm}^2$, $\mu = 1153.8461 \text{ kN/mm}^2$, $C_{MC} = 1 \text{ kN/mm}^2$ and $\phi = 30^\circ$). The number of iterations of the augmented–dual–CPPM for several elastic trial states and different values of the penalty parameter c are depicted in Figure 5.6. The range of the trial state space depicted is $\theta_{\varepsilon^e, trial} = 30^\circ$, $q_{\varepsilon^e, trial}$ from 0 to $5 \cdot \sqrt{3}C_{MC} / (2\mu)$ and $p_{\varepsilon^e, trial}$ from -3 to $0 \cdot C_{MC} \cot(\phi) / (3K)$, the same as in Figure 4.7 for the primal–CPPM.

The algorithm leads to convergence for all the trial states, a reflection of the global convergent character of the proposed schemes. The dependence of the results on the penalty parameter c follows the same trend as in the previous section. In fact, the range of adequate values of c is also similar, $c \cdot C_{MC} \in (0.01, 0.1)$. Two observations follow from the comparison of the results obtained with $c = 0.1/C_{MC}$ with those obtained with the primal–CPPM. First, the number of iterations of the dual–CPPM is, in general, higher (especially where the primal–CPPM converges in few iterations). However, the maximum number of

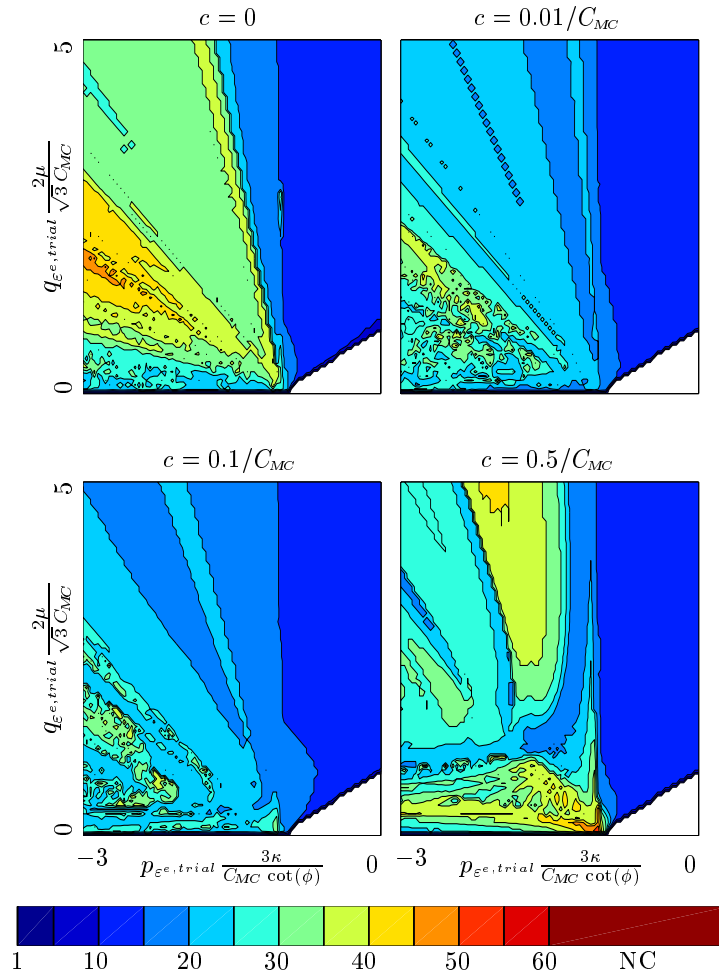


FIGURE 5.6. Single increment tests: pressure-dependent plastic models. Number of iterations needed for convergence by the dual-CPPM ($c = 0$) and the augmented-dual-CPPM for different values of the penalty parameter c , and $\theta_{\epsilon^e, trial} = 30^\circ$.

iterations is lower: with the primal-CPPM it is 49, and only 40 with the dual-CPPM. These maximum values are reached with different trial states. The maximum number of curve fittings is set to $j_{max} = 3$ as in the example in Section 4.1.2. The same overall behavior discussed in this section is observed on the dependence of this parameter in the numerical performance of the algorithms in these non-smooth cases.

6. Finite element application

In this section, the primal-CPPM is applied to solve the necking of a cylindrical bar, as an example of practical application of the algorithms presented in previous sections. This problem is a well-known benchmark test in large-strain solid mechanics, see SIMO

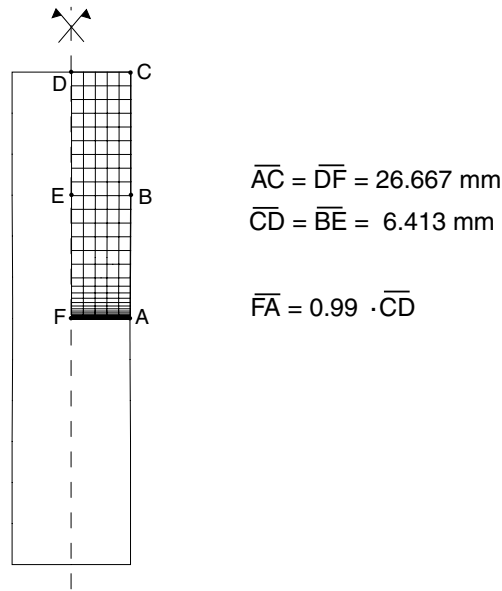


FIGURE 6.1. Necking of a cylindrical bar. Problem definition and computational mesh.

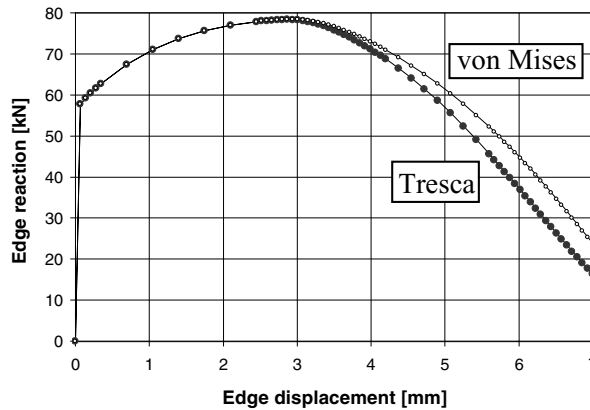


FIGURE 6.2. Necking of a cylindrical bar. Load–displacement curves obtained with the von Mises model and the Tresca model.

& HUGHES [1998] for the analysis of this test with the von Mises model, and MIEHE [1998] and PERIĆ & DE SOUZA NETO [1999] for the solution with Tresca-like models.

The test consists in the uniaxial extension of a cylindrical bar with circular cross-section, with a radius of 6.413 mm and 53.334 mm length. A slight geometric imperfection (1% reduction in radius), see Figure 6.1, induces necking in the central part of the bar. An axisymmetric analysis is carried out with the mesh shown in Figure 6.1. Eight-noded quadrilateral elements with 2×2 Gauss-points are used.

The Hencky's hyperelastic law and a Tresca-like plastic model (the von Mises–Tresca

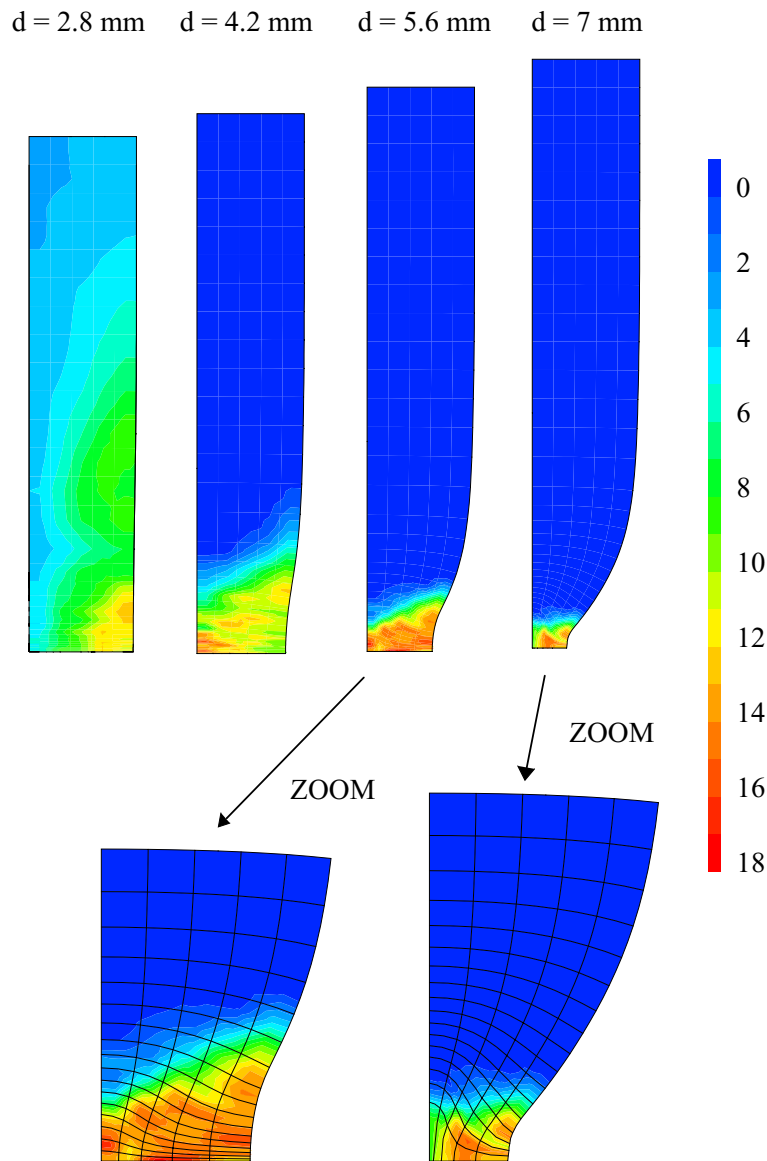


FIGURE 6.3. Necking of a cylindrical bar with the Tresca model and the primal-CPPM. Distribution of number of iterations at Gauss-point level for four load increments, top displacements equal to 2.8, 4., 5.6 and 7 mm.

model with a shape parameter $m = 20$, see Section II.2), are used here. The load–displacement curve is depicted in Figure 6.2. The results obtained with the von Mises model are included in the same figure for comparative purposes. Both results agree with those presented by MIEHE [1998] and PERIĆ & DE SOUZA NETO [1999]. The load increments used in the simulations are marked on the curves. Load increments of reduced size have been needed in the middle and the end of the test to ensure convergence of the problem with the Tresca model. With the primal-CPPM the convergence at Gauss–point level

does not limit the size of the load increments, see Figure 6.3 with the distribution of number of iterations at Gauss-point level for four load increments. This is in contrast with the Newton–CPPM, where the size of the load increments is restricted by the poor convergence properties of the algorithm at Gauss–point level, and, therefore, the more demanding closest–point projection problem guides the incremental–iterative solution of the overall finite element problem.

7. Conclusions

We have presented in this paper two new families of algorithms for the solution of the closest–point projection equations in elastoplasticity, referred to as primal and dual algorithms. Augmented Lagrangian extensions have been considered in both cases, as well as extensions to the viscoplastic problem. The proposed algorithms have been evaluated in the context of multiplicative models of finite strain isotropic plasticity, based on general models of finite hyperelasticity (Hencky’s law and Ogden models), including examples with perfect plasticity, strain hardening and strain softening. This general setting has been considered without requiring the convexity assumptions necessary for the rigorous theoretical characterization of the variational structure developed in Part I of this work, and which motivated all these developments. Plastic models based on deviatoric and pressure-dependent yield surfaces have been considered, the latter leading in addition to non-differentiable flow vectors and thus allowing the evaluation of the numerical schemes under these conditions.

The primal–CPPM consists of the application of a Newton scheme with the appropriate line search scheme applied directly to the primal equations of the problem in the elastic strains, strain-like internal variables and plastic multiplier (that is, the Euler-Lagrange equations in the variational context provided by the assumptions of convexity and associativity). The proposed line search scheme accounts for the constraint of positive plastic multiplier and, up to the existence of spurious accumulation points shown not to appear in common materials models (see Remark I.1.1 in Appendix I for alternative modifications), lead in practice to the globally convergent character of the primal–CPPM. The corresponding augmented extension, the augmented–primal–CPPM, has been proposed avoiding this difficulty.

In contrast, the dual algorithms split the closest–point projection equations in two, leading to two-level algorithms: the upper level consisting of the enforcement of the plastic consistency condition through an iteration in the plastic multiplier, with the lower level consisting of the solution of the closest–point projection equations for a fixed plastic multiplier. Both levels are solved with a Newton scheme in combination of a line search scheme, assuring the asymptotic quadratic rate of convergence of both iteration processes. In particular, the dual–CPPM, involving a constrained upper level problem because again of the

non-negative character of the plastic multiplier, has been shown not to require the activation of special line search schemes, since this constraint cannot be activated. The resulting algorithms have been rigorously proven to be globally convergent under the usual assumptions of convexity. Augmented extensions, referred to as the augmented–dual–CPPM, has still been presented to improve in their numerical performance as summarized below.

Based on the numerical results presented in Sections 4, 5 and 6, we conclude that all the newly proposed algorithms show a dramatic improvement over the standard Newton–CPPM. The large regions of no convergence observed with this scheme are avoided entirely, illustrating the improved global convergence properties of the proposed schemes while maintaining locally the desired asymptotic quadratic rate of convergence. Focusing first on the primal–CPPM, we observe that this improvement comes at no extra computational cost for all practical purposes. In fact, the scheme reduces to the Newton–CPPM when the latter does not exhibit difficulties in the convergence. The dual–CPPM has shown to be computationally competitive when the primal–CPPM requires a large number of iterations to converge, namely, the regions where the Newton–CPPM exhibits no convergence.

The augmented versions of the algorithms have improved properties with respect to the non–augmented ones. They do not need to enforce explicitly the constraint of non-negative plastic multipliers, leading to unconstrained problems easily to treat analytically and avoiding altogether complex line search schemes in practice. Moreover, they have been shown to reduce the computational cost of the original algorithms (that is, a reduced number of iterations) when the regularization parameter is chosen in a given range. A dimensionless expression of this range has been identified in the representative numerical simulations presented in this paper, and it covers approximately one order of magnitude. This improvement in computational cost is more significant for the dual–CPPM, resulting in the so-called augmented–dual–CPPM, even though it does not lead to a fully competitive scheme in regions where the primal–CPPM, or even the Newton–CPPM, show no difficulties, as noted above.

In conclusion, the local integration of the elastoplastic models, involving commonly used yield surfaces with high curvature and/or complex elastic and hardening/softening laws, lead to highly nonlinear equations where currently available techniques show clear difficulties, even no convergence unless small load increments are considered. Since this limitation, even at a single quadrature point of a typical finite element implementation, hinders directly the solution of the global mechanical boundary-value problem, it is of the main interest to consider robust globally convergent schemes for the solution of the resulting closest-point projection equations. We believe that the new algorithms presented in this work provide efficient and computationally competitive alternatives in this respect.

Acknowledgments: Financial support for this research has been provided by the ONR under contract no. N00014-96-1-0818 and the NSF under contract no. CMS-9703000 with UC Berkeley. A. Pérez-Foguet was supported by the Generalitat de Catalunya (grant

number 1998 BEAI200042) and the Commission for Cultural, Educational and Scientific Exchange between the US and Spain (program of 1999, number 99258). All this support is gratefully acknowledged.

References

- ARMERO, F. & PÉREZ-FOGUET, A. [2000], “On the Formulation of Closest-Point Projection Algorithms for Elastoplasticity. Part I: The Variational Structure,” submitted for publication on *Int. J. Num. Meth. Engr.*
- ABBO, A.J. & SLOAN, S.W. [1995], “A smooth hyperbolic approximation to the Mohr-Coulomb yield criterion”, *Computers and Structures*, **54**, 427-441.
- BERTSEKAS, D.P. [1982] *Constrained Optimization and Lagrange Multiplier Methods*, Athena Scientific, Belmont (reprint of 1996).
- BIĆANIĆ, N. & PEARCE, C.J. [1996], “Computational aspects of a softening plasticity model for plain concrete”, *Mechanics of Cohesive and Frictional Materials* **1**, 75-94.
- DENNIS & SCHNABEL [1983] *Numerical methods for unconstrained optimization and nonlinear equations*, Prentice-Hall, New Jersey (reprint of 1996).
- LUENBERGER, D.G. [1989] *Linear and Nonlinear Programming*, Addison-Wesley, Reading.
- MIEHE, C. [1998], “A formulation of finite elastoplasticity based on dual co- and contravariant eigenvector triads normalized with respect to a plastic metric”, *Comp. Meth. Appl. Mech. Engr.*, **159**, 223-260.
- PÉREZ-FOGUET, A., RODRÍGUEZ-FERRAN, A. & HUERTA, A. [2000a], “Consistent Tangent Matrices for Substepping Schemes”, *Comp. Meth. Appl. Mech. Engr.* in press.
- PÉREZ-FOGUET, A., RODRÍGUEZ-FERRAN, A. & HUERTA, A. [2000b], “Numerical differentiation for local and global tangent operators in computational plasticity”, *Comp. Meth. Appl. Mech. Engr.* **189**, 277-296.
- PERIĆ, D. & DE SOUZA NETO, E. A. [1999], “A new computational model for Tresca plasticity at finite strains with an optimal parametrization in the principal space”, *Comp. Meth. Appl. Mech. Engr.* **171**, 463-489.
- SHULTZ, G.A., SCHNABEL, R.B. & BYRD, R.H. [1985], “A family of trust-region-based algorithms for unconstrained minimization with strong global convergence properties”, *SIAM J. Numerical Analysis*, **22**, 47-67.
- SIMO, J.C. & HUGHES, T.J.R. [1998] *Computational Inelasticity*, Springer, New York.
- DE SOUZA NETO, E.A., PERIĆ, D. & OWEN, D.R.J. [1994], “A Model for Elastoplastic Damage at Finite Strains: Algorithmic Issues and Applications”, *Engr. Computation*

11, 257-281.

Appendix I. Line Search Schemes

We summarize in this appendix some basic results on the formulation of solution algorithms for nonlinear algebraic systems of equations as they are used in this paper. The interest herein is the development of globally convergent algorithms for the closest-point projection equations of elastoplasticity. To this purpose, Newton algorithms combined with the proper line search schemes are presented for general unconstrained and unilaterally constrained problems in Sections I.1 and I.2, respectively. Complete details on the classical results presented in this appendix section can be found in BERTSEKAS [1982], DENNIS & SCHNABEL [1983] and LUENBERGER [1989].

I.1. Unconstrained problems

Consider the general unconstrained algebraic system of equations

$$\mathbf{r}(\mathbf{x}) = 0, \quad (\text{I.1})$$

for the unknown vector $\mathbf{x} \in \mathbb{R}^{n_x}$, with $n_x \geq 1$, and the function $\mathbf{r} : \mathbb{R}^{n_x} \rightarrow \mathbb{R}^{n_x}$. The general problem (I.1) corresponds in some of the cases considered in this work to the first order necessary conditions of the unconstrained minimization problem

$$\min_{\mathbf{x} \in \mathbb{R}^{n_x}} \varphi(\mathbf{x}) \quad (\text{I.2})$$

for a function $\varphi(\mathbf{x}) : \mathbb{R}^{n_x} \rightarrow \mathbb{R}$ continuously differentiable with $\mathbf{r}(\mathbf{x}) = \nabla\varphi(\mathbf{x})$ (its gradient). In this context, we consider a general algorithm of the form

$$\mathbf{x}^{(k+1)} = \mathbf{x}^{(k)} + \alpha^{(k)} \mathbf{d}^{(k)} \quad k = 0, 1, \dots, \quad (\text{I.3})$$

for a given initial value $\mathbf{x}^{(0)}$, the update direction $\mathbf{d}^{(k)} \in \mathbb{R}^{n_x}$ and line search parameter $\alpha^{(k)} \in \mathbb{R}$. We direct our attention to solution algorithms exhibiting an asymptotically quadratic rate of convergence through the consideration of the Newton update direction

$$\mathbf{d}^{(k)} = - \left(\mathbf{J}(\mathbf{x}^{(k)}) \right)^{-1} \mathbf{r}(\mathbf{x}^{(k)}) \quad \text{for } \mathbf{J}(\mathbf{x}) := \nabla\mathbf{r}(\mathbf{x}) \in \mathbb{R}^{n_x \times n_x}, \quad (\text{I.4})$$

so $\mathbf{J} = \nabla^2\varphi$ in the case given by (I.2). Enough regularity is tacitly assumed for the definition (I.4) to make sense, as it is the invertibility of the Jacobian matrix. The case of a strictly convex objective function $\varphi(\mathbf{x})$, as it appears in some of the variational principles considered in Part I of this work, assures this last condition, given the positive definite character of $\mathbf{J}(\mathbf{x})$ in this case.

Our main interest is directed to globally convergent extensions of the pure Newton scheme ($\alpha^{(k)} \equiv 1$), assuring the convergence of the sequence $\{\mathbf{x}^{(k)}\}$ from any initial trial

value $\mathbf{x}^{(0)}$ to a solution of (I.1). The classical Global Convergence Theorem (see LUENBERGER [1989], page 187) assures this desirable property for bounded sequences $\{\mathbf{x}^{(k)}\}$ if the algorithm (I.3) defines a continuous mapping from $\mathbf{x}^{(k)}$ to $\mathbf{x}^{(k+1)}$ (closed mapping in the general context if multiple values $\mathbf{x}^{(k+1)}$ exist) and a continuous descent function $M : \mathbb{R}^{n_x} \rightarrow \mathbb{R}$ exists (that is, $M(\mathbf{x}^{(k+1)}) < M(\mathbf{x}^{(k)})$, “ \leq ” if $\mathbf{x}^{(k)}$ is a solution). These two requirements are satisfied by the algorithm (I.3) if the line search parameter $\alpha^{((k)} > 0$ is obtained as the minimization of the merit function

$$\hat{M}(\alpha) := M(\mathbf{x}^{(k)} + \alpha \mathbf{d}^{(k)}) , \quad (\text{I.5})$$

defined in terms of the descent function itself, and the update direction $\mathbf{d}^{(k)}$ defines a descent direction in the sense that

$$\hat{M}'(0) = \nabla M(\mathbf{x}^{(k)}) \cdot \mathbf{d}^{(k)} \leq 0 . \quad (\text{I.6})$$

Practical line search schemes are obtained by considering an approximate solution of the minimization problem of the merit function (I.5). In this case, the global convergence of the final algorithm is preserved if the so-called Goldstein’s conditions (LUENBERGER [1989], page 214)

$$M(\mathbf{x}^{(k)} + \alpha^{(k)} \mathbf{d}^{(k)}) \leq M(\mathbf{x}^{(k)}) + \beta \alpha^{(k)} \nabla M(\mathbf{x}^{(k)}) \cdot \mathbf{d}^{(k)} \quad (\text{I.7})$$

$$M(\mathbf{x}^{(k)} + \alpha^{(k)} \mathbf{d}^{(k)}) \geq M(\mathbf{x}^{(k)}) + (1 - \beta) \alpha^{(k)} \nabla M(\mathbf{x}^{(k)}) \cdot \mathbf{d}^{(k)} , \quad (\text{I.8})$$

with $\beta \in (0, 1/2)$, are satisfied. Moreover, the value $\alpha^{(k)} = 1$ is chosen whenever it verifies equations (I.7) and (I.8), assuring at the same time that the asymptotic quadratic rate of convergence of the original Newton update (I.4) is maintained. The first Goldstein condition (I.7) implies the reduction of the merit function, bounding also the line search parameter $\alpha^{(k)} > 0$ from above. The second Goldstein condition (I.8) assures that this parameter is bounded away from zero. Other equivalent conditions can be found in the literature.

A descent function for the problem (I.1) can be constructed in terms of the residual $\mathbf{r}(x)$ itself as

$$M(\mathbf{x}) := \frac{1}{2} \mathbf{r}(\mathbf{x}) \cdot \mathbf{r}(\mathbf{x}) , \quad (\text{I.9})$$

for the Euclidean inner product “ \cdot ” in \mathbb{R}^{n_x} . The descent property (I.6) follows for this function and the Newton update (I.4) after noting that

$$\nabla M(\mathbf{x}^{(k)}) \cdot \mathbf{d}^{(k)} = -\mathbf{r}(\mathbf{x}^{(k)}) \cdot \mathbf{r}(\mathbf{x}^{(k)}) = -2M(\mathbf{x}^{(k)}) \leq 0 . \quad (\text{I.10})$$

For the minimization problem (I.2), an alternative descent function is given by the simple choice $M(\mathbf{x}) = \varphi(\mathbf{x})$ when this function is strictly convex. Given the generality of (I.10),

BOX I.1. A line search scheme for unconstrained problems. The parameters $\eta = 0.1$ and $\beta = 10^{-4}$ are considered in the numerical simulations presented in this paper.

1. Input data: $\mathbf{x}^{(k)}$, $\mathbf{r}^{(k)}$ and $\mathbf{d}^{(k)}$.
2. Initialize: set $j = 0$, $\alpha_{(0)}^{(k)} = 1$, $\hat{M}^{(k)} := \mathbf{r}^{(k)} \cdot \mathbf{r}^{(k)} / 2$
and $\hat{M}'^{(k)} := -2 \hat{M}^{(k)}$.
3. Compute the new unknowns, residuals and merit function:

$$\mathbf{x}_{(j)}^{(k+1)} := \mathbf{x}^{(k)} + \alpha_{(j)}^{(k)} \mathbf{d}^{(k)}$$

$$\mathbf{r}_{(j)}^{(k+1)} := \mathbf{r}(\mathbf{x}_{(j)}^{(k+1)})$$

$$\hat{M}_{(j)}^{(k+1)} := \mathbf{r}_{(j)}^{(k+1)} \cdot \mathbf{r}_{(j)}^{(k+1)} / 2$$

4. Check Goldstein's condition:

IF $\hat{M}_{(j)}^{(k+1)} \leq (1 - 2\beta \alpha_{(j)}^{(k)}) \hat{M}^{(k)}$ THEN set $\mathbf{x}^{(k+1)} = \mathbf{x}_{(j)}^{(k+1)}$ and EXIT.

5. Check for maximum number of quadratic curve fittings:

IF $j = j_{max}$ THEN notify, set $\mathbf{x}^{(k+1)} = \mathbf{x}_{(j)}^{(k+1)}$ and EXIT.

6. Compute new value of line search parameter:

$$\alpha_{(j+1)}^{(k)} := \text{MAX} \left\{ \eta \alpha_{(j)}^{(k)}, \frac{-\left(\alpha_{(j)}^{(k)}\right)^2 \hat{M}'^{(k)}}{2\left(\hat{M}_{(j)}^{(k+1)} - \hat{M}^{(k)} - \alpha_{(j)}^{(k)} \hat{M}'^{(k)}\right)} \right\}$$

7. Set $j \leftarrow j + 1$ and GO TO 3.

we have chosen the function (I.9) in the developments that follow, even if this convexity property holds.

Several iterative techniques can be found in the literature for the construction of line search schemes satisfying the conditions (I.7)-(I.8). In this work we consider a curve fitting technique, consisting of a quadratic fit of the merit function \hat{M} from the values $\hat{M}^{(k)}$, $\hat{M}'^{(k)}$ and $\hat{M}_{(j)}^{(k)}$ at the iteration value $\alpha_{(j)}^{(k)}$, with the new value $\alpha_{(j+1)}^{(k)}$ given by the minimum of the resulting quadratic curve. This process is repeated for a finite number of iterations ($j = 0, 1, \dots, j_{max}$) until the first Goldstein condition (I.7), which reads in this case

$$\hat{M}(\alpha_{(j)}^{(k)}) =: \hat{M}_{(j)}^{(k)} \leq (1 - 2\beta \alpha_{(j)}^{(k)}) \hat{M}^{(k)}, \quad (\text{I.11})$$

is satisfied. Alternative techniques based on a cubic fit can be found in DENNIS & SCHNABEL [1983]. The simple scheme proposed herein has shown a good performance in the problems of interest in this work; the final formulae have been summarized in Box I.1. We observe that the second condition (I.8), requiring that the line search parameter $\alpha^{(k)} > 0$ is not too small, is taken into account by imposing $\alpha_{(j+1)}^{(k)} \geq \eta \alpha_{(j)}^{(k)}$ for a fixed value $\eta > 0$. These considerations lead to the so-called “backtracking”, as it was proposed in SHULTZ ET AL. [1985] together with the recommended values $\eta = 0.1$ and $\beta = 10^{-4}$ in (I.7).

With respect to the computational cost of the final scheme, we note that if the initial estimate $\alpha_{(0)}^{(k)} = 1$ is admissible, the line search requires only one additional vector norm computation. If the curve fitting loop is activated, each new $\alpha_{(j)}^{(k)}$ has a computational cost equivalent to that of the residual computation, with a fixed number of iterations. Usually, the computation of the Jacobian’s inverse $(\mathbf{J}(\mathbf{x}))^{-1}$ is considerably more expensive than the residual $\mathbf{r}(\mathbf{x})$. Hence, the computation involved in the determination of the line search does not lead to a significant computational cost in a typical iteration of the Newton scheme.

I.2. Unilaterally constrained problems

The unilaterally constrained problems arising in the plastic corrector steps of some of the formulations of the closest-point projection equations considered in this work can be written in the general residual form (I.1) with the added constraint of non-negative, say, n_x component of the solution vector $\mathbf{x} \in \mathbb{R}^{n_x}$, that is,

$$\mathbf{r}(\mathbf{x}) = 0, \quad \text{with} \quad [\mathbf{x}]_{n_x} := x_{n_x} \geq 0. \quad (\text{I.12})$$

The constraint (I.12)₂ corresponds to the non-negative character of the plastic multiplier in the primal closest-point projection schemes presented in Section 2. The equation (I.12)₁ may correspond again to the first order necessary of the minimization problem (I.2), now constrained by (I.12)₂. In fact, the dual closest-point projection schemes presented in Section 3 below will be based on such a principle for the scalar dual function presented in Part I of this work, with $n_x = 1$ in this case.

The algorithms considered in the previous section for unconstrained problems can be generalized to the constraint case while maintaining the same convergence properties as

$$\mathbf{x}^{(k+1)} = \langle \mathbf{x}^{(k)} + \alpha^{(k)} \mathbf{d}^{(k)} \rangle_{n_x}, \quad (\text{I.13})$$

where the vector function $\langle \mathbf{x} \rangle_{n_x} : \mathbb{R}^{n_x} \rightarrow \mathbb{R}^{n_x-1} \times [0, \infty)$ is defined in components as

$$[\langle \mathbf{x} \rangle_{n_x}]_i = x_i \quad \forall i < n_x \quad \text{and} \quad [\langle \mathbf{x} \rangle_{n_x}]_{n_x} = \langle x_{n_x} \rangle. \quad (\text{I.14})$$

Here, $\langle \cdot \rangle : \mathbb{R} \rightarrow [0, \infty)$ denotes the Maucalay brackets $\langle x \rangle = (x + |x|)/2$. If the constraint (I.12)₂ is active, that is, if

$$[\mathbf{x}^{(k)}]_{n_x} = x_{n_x}^{(k)} = 0 \quad \text{and} \quad \left[\nabla M(\mathbf{x}^{(k)}) \right]_{n_x} = \left[\left(\mathbf{J}(\mathbf{x}^{(k)}) \right)^T \mathbf{r}(\mathbf{x}^{(k)}) \right]_{n_x} > 0, \quad (\text{I.15})$$

with $(\cdot)^T$ denoting the matrix transpose, then the update direction $\mathbf{d}^{(k)}$ is given by

$$\mathbf{d}^{(k)} = -\mathbf{D}^{(k)} \nabla M(\mathbf{x}^{(k)}) = -\mathbf{D}^{(k)} \left(\mathbf{J}(\mathbf{x}^{(k)}) \right)^T \mathbf{r}(\mathbf{x}^{(k)}), \quad (\text{I.16})$$

for the descent function $M(\mathbf{x})$ defined in (I.9) and the symmetric matrix $\mathbf{D}^{(k)}$ defined in components by

$$\begin{aligned} \left[\mathbf{D}^{(k)} \right]_{ij} &= \left[\left(\mathbf{J}(\mathbf{x}^{(k)}) \right)^{-1} \left(\mathbf{J}(\mathbf{x}^{(k)}) \right)^{-T} \right]_{ij} \quad \forall i, j < n_x \text{ or } i = j = n_x, \\ \left[\mathbf{D}^{(k)} \right]_{n_x j} &= \left[\mathbf{D}^{(k)} \right]_{j n_x} = 0 \quad \forall j < n_x. \end{aligned} \quad (\text{I.17})$$

The original Newton update (I.4) is considered when the constraint (I.12)₂ is not active (i.e., the conditions (I.15) are not satisfied). Finally, the first Goldstein's condition (I.7) is written as

$$M(\langle \mathbf{x}^{(k)} + \alpha^{(k)} \mathbf{d}^{(k)} \rangle_{n_x}) \leq M(\mathbf{x}^{(k)}) + \beta \nabla M(\mathbf{x}^{(k)}) \cdot \left(\langle \mathbf{x}^{(k)} + \alpha^{(k)} \mathbf{d}^{(k)} \rangle_{n_x} - \mathbf{x}^{(k)} \right), \quad (\text{I.18})$$

in the considered constrained case. Note that $\mathbf{x}^{(k)}$ and, in particular, $\mathbf{x}^{(0)}$ is assumed to satisfy the constraint (I.12)₂ in these expressions.

The line search scheme developed in the previous section can be easily extended to account for the constraint (I.12)₂. The evaluation of the merit function reads now

$$\hat{M}_{(j)}^{(k)} = M(\langle \mathbf{x}^{(k)} + \alpha_{(j)}^{(k)} \mathbf{d}^{(k)} \rangle_{n_x}),$$

when verifying the modified first Goldstein's condition (I.18). The derivative of the merit function is modified accordingly, in particular if the constraint is active at $\mathbf{x}^{(k)}$ (signaled by $\mathbf{d}^{(k)} \neq -(\mathbf{J}^{(k)})^{-1} \mathbf{r}^{(k)}$). The final algorithm is summarized in Box I.2. We note that, if the constraint is not activated, the final scheme coincides with the original line search scheme presented in Box I.1 for unconstrained problems. We can also observe that, if the constraint does become activated, some additional matrix vector multiplications are needed, but still leading to a low computational cost when compared to the computation of the Newton update direction.

BOX I.2. A line search scheme for constrained problems. The parameters $\eta = 0.1$ and $\beta = 10^{-4}$ are considered in the numerical simulations presented in this paper.

1. Input data: $\mathbf{x}^{(k)}$, $\mathbf{r}^{(k)}$, $\mathbf{d}^{(k)}$ and flag, where

$$\text{flag} = \text{.true.} \quad \iff \quad \mathbf{d}^{(k)} = -(\mathbf{J}^{(k)})^{-1} \mathbf{r}^{(k)}$$

for $\mathbf{r}^{(k)} := \mathbf{r}(\mathbf{x}^{(k)})$ and $\mathbf{J}^{(k)} := \nabla \mathbf{r}(\mathbf{x}^{(k)})$.

2. Initialize: set $j = 0$, $\alpha_{(0)}^{(k)} = 1$ and

$$\hat{M}^{(k)} := \begin{cases} -2 \hat{M}^{(k)} & \text{for flag} = \text{.true.} \\ \mathbf{r}^{(k)} \cdot \mathbf{J}^{(k)} \mathbf{d}^{(k)} & \text{for flag} = \text{.false.} \end{cases}$$

for $\hat{M}^{(k)} := \mathbf{r}^{(k)} \cdot \mathbf{r}^{(k)} / 2$.

3. Compute the new unknowns, residuals and merit function:

$$\mathbf{x}_{(j)}^{(k+1)} := \langle \mathbf{x}^{(k)} + \alpha_{(j)}^{(k)} \mathbf{d}^{(k)} \rangle_{n_x}$$

$$\mathbf{r}_{(j)}^{(k+1)} := \mathbf{r}(\mathbf{x}_{(j)}^{(k+1)})$$

$$\hat{M}_{(j)}^{(k+1)} := \mathbf{r}_{(j)}^{(k+1)} \cdot \mathbf{r}_{(j)}^{(k+1)} / 2$$

4. Compute upper limit of Goldstein's condition:

IF (flag).and. $\left([\mathbf{x}^{(k)}]_{n_x} + \alpha_{(j)}^{(k)} [\mathbf{d}^{(k)}]_{n_x} \geq 0 \right)$ THEN

$$\text{uplim} := \left(1 - 2\beta \alpha_{(j)}^{(k)} \right) \hat{M}^{(k)}$$

ELSE

$$\text{uplim} := \hat{M}^{(k)} + \beta \mathbf{r}^{(k)} \cdot \mathbf{J}^{(k)} (\mathbf{x}_{(j)}^{(k+1)} - \mathbf{x}^{(k)})$$

ENDIF

5. Check Goldstein's condition:

IF $\hat{M}_{(j)}^{(k+1)} \leq \text{uplim}$ THEN set $\mathbf{x}^{(k+1)} = \mathbf{x}_{(j)}^{(k+1)}$ and EXIT.

6. Check for maximum number of quadratic curve fittings:

IF $j = j_{max}$ THEN notify, set $\mathbf{x}^{(k+1)} = \mathbf{x}_{(j)}^{(k+1)}$ and EXIT.

7. Compute new value of line search parameter:

$$\alpha_{(j+1)}^{(k)} := \text{MAX} \left\{ \eta \alpha_{(j)}^{(k)}, \frac{-\left(\alpha_{(j)}^{(k)}\right)^2 \hat{M}'^{(k)}}{2 \left(\hat{M}_{(j)}^{(k+1)} - \hat{M}^{(k)} - \alpha_{(j)}^{(k)} \hat{M}'^{(k)} \right)} \right\}$$

8. Set $j \leftarrow j + 1$ and GO TO 3.

Remarks I.1.

1. The previous Newton scheme with line search results effectively in the local minimization of the descent function $M(\mathbf{x})$. In the unconstrained problem of Section I.1, the solution of this problem is given by $\nabla M = \mathbf{J}^T \mathbf{r} = 0$, corresponding to the solution of the original problem (I.12) for a non-singular Jacobian, as it is the case in the problems of interest herein (see the discussion in Section 2.1). In the constrained case considered in this section, additional solutions may appear at the boundary of the admissible set, that is, points characterized by

$$[\mathbf{x}]_{n_x} = 0, \quad [\nabla M(\mathbf{x})]_{1,\dots,n_x-1} = 0 \quad \text{and} \quad [\nabla M(\mathbf{x})]_{n_x} > 0, \quad (\text{I.19})$$

which does not imply $\mathbf{r}(\mathbf{x}) = 0$. Therefore, the iterative process summarized in Box I.2 may be attracted by these spurious solutions. In the context of the closest-point projection algorithms of interest herein, this situation can only occur in the primal-CPPM of Section 2.1, in its non-augmented form and for the inviscid problem, without affecting the other schemes proposed in this work. In the case of the primal-CPPM and for the plastic corrector problems of interest, the equations (I.19) read for the rate-independent problem

$$\left. \begin{aligned} & \Delta\gamma = 0, \\ & \begin{pmatrix} \boldsymbol{\varepsilon}^e - \boldsymbol{\varepsilon}_{n+1}^{e,trial} \\ -\boldsymbol{\alpha} + \boldsymbol{\alpha}_{n+1}^{trial} \end{pmatrix} + f \tilde{\mathbf{G}} \nabla f = 0, \\ & \mathbf{m} \cdot \begin{pmatrix} \boldsymbol{\varepsilon}^e - \boldsymbol{\varepsilon}_{n+1}^{e,trial} \\ -\boldsymbol{\alpha} + \boldsymbol{\alpha}_{n+1}^{trial} \end{pmatrix} > 0. \end{aligned} \right\} \quad (\text{I.20})$$

Note that equations (I.20)_{2,3} together with the fundamental assumption $\mathbf{m} \cdot \tilde{\mathbf{G}} \nabla f > 0$ of the underlying continuum model (see Box 1.1) imply $f(\boldsymbol{\Sigma}) < 0$ for the solution $\boldsymbol{\Sigma} = \{\boldsymbol{\sigma}, \mathbf{q}\}$ of (I.20). These solutions can be shown not to exist in particular cases and are highly unlikely in general plastic models. We have not observed them in any of the numerical simulations considered so far for typical models in practical applications. We note again that no spurious solutions of the type (I.19) can occur in the viscoplastic case treated with the constrained formulation of Remark 2.1.2, as a straightforward calculation shows. In any case, these solutions can be easily detected and avoided. For example, we observe that the solution of a plastic corrector problem for the the yield function $f_\rho(\boldsymbol{\Sigma}) := \rho f(\boldsymbol{\Sigma})$ for $\rho > 0$ differs only from the original problem based on $f(\boldsymbol{\Sigma})$ in the value of the plastic multiplier being $\Delta\gamma/\rho$, with $\Delta\gamma$ being the original solution. Considering for simplicity the case of constant $\tilde{\mathbf{G}}$, the equation (I.20)₂ reads for this new problem

$$\boldsymbol{\Sigma} - \boldsymbol{\Sigma}_{n+1}^{trial} + \rho^2 f(\boldsymbol{\Sigma}) \nabla f(\boldsymbol{\Sigma}) = 0 \quad \implies \quad \|\boldsymbol{\Sigma} - \boldsymbol{\Sigma}_{n+1}^{trial}\| = \rho^2 |f(\boldsymbol{\Sigma})| \|\nabla f(\boldsymbol{\Sigma})\|, \quad (\text{I.21})$$

with $\rho = 1$ recovering the original problem. Therefore, no spurious solutions of the form (I.20) exist in this case if the algorithmic parameter ρ is chosen such that

$$\rho^2 > \rho_{min}^2 = \frac{\min_{\{\Sigma | f(\Sigma) < 0\}} \|\Sigma - \Sigma_{n+1}^{trial}\|}{\max_{\{\Sigma | f(\Sigma) < 0\}} |f(\Sigma)| \|\nabla f(\Sigma)\|} \quad (\text{I.22})$$

since (I.21) has no solutions in this case. Alternatively, the use of more complex merit functions $M(\mathbf{x})$ avoiding altogether this situation can also be devised; see e.g. BERTSEKAS [1982] for such merit functions in the context of constrained convex optimization problems. Since these theoretical difficulties only appear in the direct solution of the original closest-point projection equations in their primal constrained form considered in Section 2.1, and are entirely avoided by the consideration of the augmented and dual formulations of these equations considered in the rest of the paper, thus allowing rigorously the use of the simple merit function (I.9), this choice has been considered in this work, avoiding the unnecessary use of more complex formulations as presented above. Additional details are therefore omitted.

2. We note that, as mentioned above, the convergence of the algorithms in both the unconstrained and constrained forms requires the sequence $\{\mathbf{x}^{(k)}\}$ to be bounded in order to ensure convergence, in addition of the conditions (I.6) to (I.8). Given the descent character of the function $M(\mathbf{x})$, this property is assured if the sets $\mathcal{S}_\varrho = \{\mathbf{x} \mid M(\mathbf{x}) < \varrho\}$ are bounded for $\varrho < \infty$. From the definition (I.9), we observe that this condition holds if $M(\mathbf{x}) = \|\mathbf{r}(\mathbf{x})\|^2/2 \rightarrow \infty$ as $\|\mathbf{x}\| \rightarrow \infty$. This property is to be expected for the cases of interest in this work. For example, we can write the relation

$$2 M(\mathbf{x}) = (\mathbf{x} - \mathbf{x}^{(0)}) \cdot \begin{pmatrix} \mathbf{I} & \mathbf{m} \\ \mathbf{m}^T & \|\mathbf{m}\|^2 \end{pmatrix} (\mathbf{x} - \mathbf{x}^{(0)}) + |f|^2, \quad (\text{I.23})$$

for the residual $\mathbf{r}(\mathbf{x})$ defined in Box 1.1, with $\|\mathbf{m}\|^2 := \mathbf{m} \cdot \mathbf{m}$, $\mathbf{x} = \{\boldsymbol{\varepsilon}^e, -\boldsymbol{\alpha}, \Delta\gamma\}^T$ and the finite trial values $\mathbf{x}^{(0)} = \{\boldsymbol{\varepsilon}_{n+1}^{e,trial}, -\boldsymbol{\alpha}_{n+1}^{trial}, 0\}^T$. Therefore, we conclude that $M(\mathbf{x}) \rightarrow \infty$ for $\|\mathbf{x} - \mathbf{x}^{(0)}\| \rightarrow \infty$ along any path except possibly the kernel of the matrix in (I.23), that is, for $\mathbf{x} - \mathbf{x}^{(0)} = \zeta \{-\mathbf{m}, 1\}^T$ with $\zeta \in \mathbb{R}$, in which case $2M(\mathbf{x}) = |f|^2$. Note that \mathbf{m} depends on \mathbf{x} in general, and that the algorithm imposes the constraint $\Delta\gamma \geq 0$ for the last component of \mathbf{x} , so the case of interest involves $\zeta \geq 0$. Therefore, we must impose the condition

$$|f(\boldsymbol{\Sigma}(\mathcal{I}))| \rightarrow \infty \quad \text{for} \quad \mathcal{I} = \mathcal{I}_{n+1}^{trial} - \zeta \mathbf{m}(\boldsymbol{\Sigma}(\mathcal{I})) \quad \text{and} \quad \zeta \rightarrow \infty, \quad (\text{I.24})$$

where $\boldsymbol{\Sigma} := \{\boldsymbol{\sigma}, \mathbf{q}\}^T$, $\mathcal{I} := \{\boldsymbol{\varepsilon}^e, -\boldsymbol{\alpha}\}^T$ and \mathcal{I}^{trial} is the corresponding trial value, independently of $\Delta\gamma$. For typical coercive elastic relations $\boldsymbol{\Sigma}(\mathcal{I})$ (that is, $\|\boldsymbol{\Sigma}\| \rightarrow \infty$ for $\|\mathcal{I}\| \rightarrow \infty$), the condition (I.24) can be understood as imposing that the yield function is coercive along the direction of plastic flow, a common situation in practical applications. \square

Appendix II. Material Models

We summarize in this appendix the material models employed in the numerical examples presented in the previous sections. The models are fully defined by the yield function $f(\boldsymbol{\sigma}, q)$ and the stored energy function of the form

$$\psi(\boldsymbol{\varepsilon}^e, \boldsymbol{\alpha}) = \psi^e(\boldsymbol{\varepsilon}^e) + \psi^h(\boldsymbol{\alpha}), \quad (\text{II.1})$$

for a hyperelastic potential $\psi^e(\boldsymbol{\varepsilon}^e)$ and isotropic hardening/softening potential $\psi^h(\boldsymbol{\alpha})$, depending on the elastic logarithmic principal stretches ($\varepsilon_i^e = \ln(\lambda_i^e)$) and the scalar strain-like internal variable α , respectively. The notation defined in Remark 4.1.1 regarding the strain and stress invariants is used in describing the material models presented in this appendix.

II.1. Hyperelastic laws

Two different hyperelastic relationships are used:

1. *Hencky's law.* The elastic potential is given in this case by the quadratic potential

$$\psi^e(\boldsymbol{\varepsilon}^e) = \frac{\kappa}{2} (\varepsilon_1^e + \varepsilon_2^e + \varepsilon_3^e)^2 + \mu \operatorname{dev}(\boldsymbol{\varepsilon}^e) \cdot \operatorname{dev}(\boldsymbol{\varepsilon}^e), \quad (\text{II.2})$$

for the bulk modulus κ and the shear modulus μ , with $\operatorname{dev}(\cdot)$ denoting the deviatoric part. The linear relations

$$p_\sigma = 3\kappa p_{\varepsilon^e}, \quad q_\sigma = 2\mu q_{\varepsilon^e} \quad \text{and} \quad \theta_\sigma = \theta_{\varepsilon^e}, \quad (\text{II.3})$$

between the invariants of the Kirchhoff stresses $\boldsymbol{\sigma} = \partial\psi_{\varepsilon^e}$ and $\boldsymbol{\varepsilon}^e$ are easily obtained. The corresponding rate expressions involve constant elasticities.

2. *Ogden model.* We consider the regularized Ogden model with logarithmic volumetric response function

$$\psi^e(\boldsymbol{\varepsilon}^e) = \frac{\kappa}{2} (\varepsilon_1^e + \varepsilon_2^e + \varepsilon_3^e)^2 + \mu_g \sum_{i=1}^3 \sum_{p=1}^N \frac{\hat{\mu}_p}{\hat{\alpha}_p} (\exp([\operatorname{dev}(\boldsymbol{\varepsilon}^e)]_i)^{\hat{\alpha}_p} - 1), \quad (\text{II.4})$$

for the bulk modulus κ and the ground shear modulus μ_g , with N terms defined by the Ogden shape parameters $\hat{\mu}_p$ and $\hat{\alpha}_p$ (with p from 1 to N). The elasticities given by the Hessian of (II.4) are clearly non constant in this case.

II.2. Yield surfaces

The interest in this work lies in the typical yield surfaces with high curvature, leading to strongly nonlinear closest-point projection equations where the standard Newton–CPPM shows clear limitations due to poor (if not any) convergence properties. To this

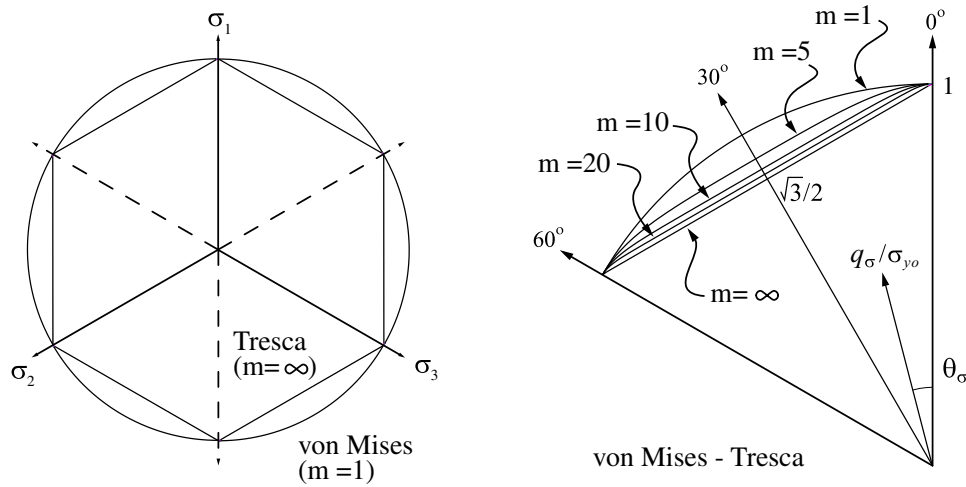


FIGURE II.1. Trace on the deviatoric plane of the von Mises–Tresca type yield surface for different values of m .

purpose, we consider two yield functions, one involving a deviatoric plastic model characteristic of metal plasticity and a pressure-dependent yield surface typical in geomechanics applications. Associated plastic evolutions are considered in both cases.

1. *Deviatoric models.* We consider the von Mises–Tresca type model defined by the general formula (see MIEHE [1998])

$$f(\boldsymbol{\sigma}, q) = \frac{2^{\frac{m-1}{2m}}}{\sqrt{3}} \left(\sum_{i=1}^3 ([\boldsymbol{\sigma}]_i - [\boldsymbol{\sigma}]_{\text{mod}(i+1,3)})^{2m} \right)^{\frac{1}{2m}} - \sqrt{\frac{2}{3}} (\sigma_{y_o} - q), \quad (\text{II.5})$$

for the initial yield limit σ_{y_o} and the stress-like internal variable $q = -\partial_\alpha \psi^h$ for the considered isotropic strain hardening/softening. The material parameter m determines the shape of the yield surface in the stress deviatoric plane, recovering the von Mises circle for $m = 1$ and the Tresca hexagon for $m \rightarrow \infty$. The elastic limit at $\theta_\sigma = 0^\circ$ and 60° is the yield stress value $q_\sigma = \sigma_{y_o}$ for all values of m . See Figure II.1 for an illustration. High values of the curvature of the yield surface are obtained for high values of the parameter m . For the value $m = 20$, the difference between the yield stress at $\theta_\sigma = 30^\circ$ between this yield surface and the Tresca hexagon is less than 2%. The combination of the yield surface (II.5) with the regularized elastic models of the previous section leads to closest-point projection equations in the deviatoric stress plane only (i.e. in $\mathbf{s} := \boldsymbol{\sigma} - \sum_{i=1}^3 [\boldsymbol{\sigma}]_i$), with a purely elastic volumetric response. The final algebraic equations considered in this paper have been implemented in this plane for this case (i.e. the residual associated with the flow rule is written in terms of the deviatoric part of the elastic strains $\text{dev}[\boldsymbol{\varepsilon}^e] := \boldsymbol{\varepsilon}^e - \sum_{i=1}^3 [\boldsymbol{\varepsilon}^e]_i$).

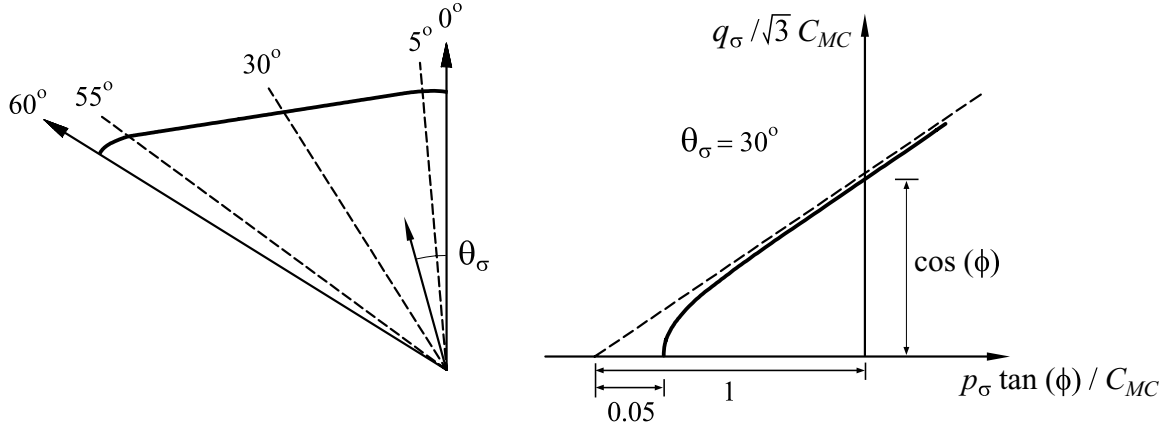


FIGURE II.2. Trace on the deviatoric and meridian stress planes of the Rounded Hyperbolic Mohr–Coulomb yield surface.

2. *Pressure-dependent yield functions.* We consider the Rounded Hyperbolic Mohr–Coulomb (RMHC) yield function (ABBO & SLOAN [1995])

$$f(\boldsymbol{\sigma}) = \sqrt{J_2(\boldsymbol{\sigma}) K^2(\theta_\sigma) + (0.05 C_{MC} \cos(\phi))^2} - (p_\sigma \sin(\phi) + C_{MC} \cos(\phi)), \quad (\text{II.6})$$

for the frictional angle ϕ and cohesion C_{MC} , and where the function $K(\theta_\sigma)$ is defined as

$$K(\theta_\sigma) = \begin{cases} A_1 - A_2 \sin(\phi) + (B_1 \sin(\phi) - B_2) \cos(3\theta_\sigma) & \theta_\sigma \leq 5^\circ \\ \frac{3 + \sin(\phi)}{2\sqrt{3}} \cos(\theta_\sigma) + \frac{1 - \sin(\phi)}{2} \sin(\theta_\sigma) & 5^\circ \leq \theta_\sigma \leq 55^\circ \\ A_1 + A_2 \sin(\phi) + (B_1 \sin(\phi) + B_2) \cos(3\theta_\sigma) & \theta_\sigma \geq 55^\circ \end{cases} \quad (\text{II.7})$$

with

$$\begin{aligned} A_1 &= \cos(25^\circ) + \frac{2 + \sqrt{3}}{3} \sin(25^\circ) \\ A_2 &= \frac{2 + \sqrt{3}}{3\sqrt{3}} \cos(25^\circ) - \frac{1}{\sqrt{3}} \sin(25^\circ) \\ B_1 &= \frac{2\sqrt{2}}{3(3 - \sqrt{3})} \cos(25^\circ) \\ B_2 &= \frac{2\sqrt{2}}{3(\sqrt{3} - 1)} \sin(25^\circ). \end{aligned} \quad (\text{II.8})$$

The RMHC surface (II.6) has been considered in ABBO & SLOAN [1995,96] and PÉREZ-FOGUET ET AL. [2000a,b] in the context of infinitesimal plasticity. Figure II.2 depicts an illustration of the trace of this yield surface with the meridian and deviatoric planes. The function (II.6) is continuously differentiable for all stress states

(ABBO & SLOAN [1995]), leading to a continuous flow vector everywhere. However, the second derivative of (II.6) in $\boldsymbol{\sigma}$ is not continuous at $\theta_\sigma = 5^\circ$, $\theta_\sigma = 55^\circ$, and therefore neither at $q_\sigma = 0$. This fact, and the high curvature at some of the rounded zones, causes the Newton–CPPM not to converge in large regions of the trial state space, in contrast with the new schemes proposed in this work.

II.3. Hardening/softening laws

The numerical examples presented in Sections 4 and 5 consider perfect plasticity as well as isotropic strain hardening and strain softening. These last two cases are considered in combination with the deviatoric yield function (II.5), with the saturation potential

$$\begin{aligned} \psi^h(\alpha) &= (\sigma_{y_\infty} - \sigma_{y_o}) \left(\alpha + \frac{1}{\delta} \exp(-\delta\alpha) \right) \\ \implies q &= -\partial_\alpha \psi^h = -(\sigma_{y_\infty} - \sigma_{y_o}) (1 - \exp(-\delta \alpha)) , \end{aligned} \quad (\text{II.9})$$

for the initial yield limit σ_{y_o} , the saturation yield stress σ_{y_∞} the saturation yield stress and the saturation exponent δ . Perfect plasticity is considered only with the pressure-dependent yield surface (II.6).